MOLECULAR DESIGN AND NANOSCALE ENGINEERING OF ORGANIC NANOFIBRIL DONOR-ACCEPTOR HETEROJUNCTIONS

by

Helin Huang

A dissertation submitted to the faculty of
The University of Utah
in partial fulfillment of the requirements for the degree of

Doctor of Philosophy

Department of Materials Science and Engineering

The University of Utah

August 2014

The University of Utah Graduate School

STATEMENT OF DISSERTATION APPROVAL

The dissertation of **Helin Huang**

has been approved by the following supervisory committee members:

Ling Zang	, Chair	**04/24/2014** Date Approved
Feng Liu	, Member	**04/29/2014** Date Approved
Michael Scarpulla	, Member	**04/24/2014** Date Approved
Ashutosh Tiwari	, Member	**04/29/2014** Date Approved
Ilya Zharov	, Member	**04/24/2014** Date Approved

and by **Feng Liu** , Chair of

the Department of **Materials Science and Engineering**

and by David B. Kieda, Dean of The Graduate School.

ABSTRACT

Organic nanofibril heterojunction materials have gained increasing research interest due to their broad applications in organic semiconductor devices. In order to enhance the device performance, we have investigated the structure-property relationship of these nanostructures by designing and synthesizing functional building block molecules, self-assembling the molecules into well-defined nanofibers, fabricating the nanofibers into optical and electrical devices, and testing their photoconductivity and sensor properties.

In Chapter 2, we present a simple approach to fabricate efficient nanofibril heterojunctions by interfacial engineering of electron donor (D**)** coating onto acceptor (A**)** nanofibers. The nanofibers both create a large D/A interface for increased charge separation and act as long-range transport pathways for photogenerated charge carriers towards the electrodes, and the alkyl groups modified at the A molecules not only enable effective surface adsorption of D molecules on the nanofibers for effective electron-transfer communication, but also spatially separate the photogenerated charge carriers to prevent their recombination.

In Chapter 3, we further investigated the effect of D molecular structure and coating morphology on photoconductivity of organic nanofiber materials. A series of D molecules with varying side-chain modifications were synthesized and investigated for the different intermolecular arrangements caused by π-π stacking in balance with steric hindrance of side-chains. Different molecular assemblies of D resulted in distinctive phase segregation

between D and A nanofiber, which significantly affects the interfacial charge separation.

In Chapter 4, we developed an alternative nanofibril heterojunction structure that is composed of D as the nanofiber, onto which a monolayer of A molecule was coated. Due to the strong redox (charge transfer) interaction between D and A, the nanofibril junction demonstrated high conductivity even without light illumination, which makes this material suitable for applications in chemiresistor sensors for detection of amines.

In Chapter 5, a series of perylene tetracarboxylic monoimides were synthesized through a one-step reaction between cycloalkyl amines and the parent perylene dianhydride. The selection of appropriate reaction medium is the most critical for achieving the high purity of product. This approach opens up a new way for large scale production of the monoimides, which are the precursor for making a variety of perylene based building block molecules.

Dedicated to my family and my country

TABLE OF CONTENTS

ABSTRACT iii

LIST OF ABBREVIATIONS ix

ACKNOWLEDGEMENTS xi

Chapter

1. INTRODUCTION 1

1.1 Organic semiconductor materials in optoelectronic applications 1
1.2 One-dimensional self-assembly nanostructures and materials 3
1.2.1 Influence of molecular packing on semiconductor properties 3
1.2.2 One-dimensional self-assembly nanostructure fabrication methods 5
1.2.3 Applications of one-dimensional self-assembly materials 8
1.3 Photoconductive mechanism 13
1.3.1 Charge-generation process 13
1.3.2 Charge-transport process 14
1.4 One-dimensional heterojunction 15
1.4.1 Inorganic one-dimensional heterojunction 16
1.4.2 Organic one-dimensional heterojunction 16
1.5 Motivation and objectives 19
1.6 References 20

2. INTERFACIAL ENGINEERING OF ORGANIC NANOFIBRIL HETEROJUNCTIONS INTO HIGHLY PHOTOCONDUCTIVE MATERIALS 42

2.1 Abstract 42
2.2 Introduction 43
2.3 Results and discussion 44
2.3.1 Fabrication of nanofibril heterojunctions 44
2.3.2 Photoconductivity of the nanofibril heterojunctions 46
2.3.3 Interfacial influence on the photoconductivity 47
2.4 Conclusion 49
2.5 Experimental section 50
2.5.1 Molecular synthesis 50
2.5.2 Fabrication of A-1 nanofibers and the nanofibril heterojunctions 52

2.5.3 Property characterization of nanofibers 52
2.5.4 Electrical measurement with nanofibers 53
2.6 References 53

3. MORPHOLOGY CONTROL OF NANOFIBRIL DONOR-ACCEPTOR HETEROJUNCTION TO ACHIEVE HIGH PHOTOCONDUCTIVITY: EXPLORATION OF NEW MOLECULAR DESIGN RULE 67

3.1 Abstract 67
3.2 Introduction 68
3.3 Results and discussion 70
3.3.1 Nanofibril heterojunction fabrication 70
3.3.2 Effect of intermolecular aggregation photoconductivity 72
3.3.3 Surface potential of nanofibril heterojunction under illumination 76
3.3.4 Solvent-annealing influence on photoconductivity 77
3.4 Conclusion 80
3.5 Experimental section 81
3.5.1 Materials 81
3.5.2 General characterization 82
3.5.3 Kelvin probe force microscopy (KPFM) 82
3.5.4 Preparation of surface-modified glass slides 83
3.6 References 83

4. ONE-STEP SURFACE DOPING OF ORGANIC NANOFIBERS TO ACHIEVE HIGH DARK CONDUCTIVITY AND CHEMIRESISTOR SENSING OF AMINES 107

4.1 Abstract 107
4.2 Introduction 107
4.3 Results and discussion 109
4.4 Conclusion 114
4.5 Experimenal section 114
4.5.1 Materials 114
4.5.2 Fabrication of nanofibers and devices 115
4.5.3 Materials characterization 116
4.5.4 Langmuir fitting of the current change versus vapor concentration of aniline 117
4.6 References 118

5. DIRECT SYNTHESIS OF HIGHLY PURE PERYLENE TETRACARBOXYLIC MONOIMIDE 139

5.1 Abstract 139
5.2 Introduction 139
5.3 Results and discussions 141
5.4 Conclusion 142

5.5 Experimental section 143
5.6 References 144

6. CONCLUDING REMARKS 150

6.1 Conclusion 150
6.2 Suggestions for future plan 153
6.3 References 154

LIST OF ABBREVIATIONS

A	Acceptor
AAO	Aluminum oxide
AEMs	Arylene ethynylene macrocycles
AFM	Atomic force microscopy
CTAB	Cetyltrimethylammonium bromide
CuPc	Copper phthalocyanine
D	Donor
DMNB	2,3-Dimethyl-2,3-dinitrobutane
DNT	2,4-Dinitrotoluene
DTC	Decyl substituted carbazole-cornered, arylene-ethynylene tetracyclic π-conjugated molecule
EA	Electron affinity
F16CuPc	Copper hexadecafluorophthalocyanine
FTS	(Tridecafluoro-1,1,2,2-tetrahydrooctyl)trichlorosilane
HBC	Hexabenzocoronene
HOMO	Highest occupied molecular orbital
H_2TPyP	5,10,15,20-Tetra(4-pyridyl)-porphyrin
H_2TPP	Tetraphenylporphyrin
IP	Ionization potential

KPFM	Kelvin probe force microscopy
LUMO	Lowest unoccupied molecular orbital
NDI	Naphthalenediimide
OFETs	Organic field effect transistors
OLEDs	Organic light emitting diodes
OPVs	Oligo(p-phenylene vinylene)s
OSCs	Organic solar cells
OTS	Trichloro(octadecyl)silane
P3HT	Poly(3-hexylthiophene)
PMI	Perylene monoimide
PTCDI	Perylene tetracarboxylic diimide
PVT	Physical vapor transport
SEM	Scanning electron microscopy
TBP	Tribenzopentaphene
TNT	Trinitrotoluene
TPP	Tetraphenylporphyrin
VOCs	Volatile organic compounds

ACKNOWLEDGEMENTS

I would like to thank my advisor, Professor Ling Zang, for his guidance and encouragement during my years of study at University of Utah. The work in this thesis could not have been accomplished without his inspiration and great help. His enthusiasm for science has always inspired me, his dedication to his career has always motivated me, and his inexhaustible ideas have always intrigued me. His influences upon me had a tremendous impact on my philosophy of scientific research and will continue to play an important role throughout my future career.

I also would like to thank my other committee members, Dr. Feng Liu, Dr. Michael Scarpulla, Dr. Ashutosh Tiwari, and Dr. Ilya Zharov, for serving on my research committee and providing valuable suggestions and encouragement during my studies. Also I would like to thank Dr. Reaz Chaudhuri for his help in seminar.

I would like to acknowledge all the former and present Zang group members for their help and companionship over the years. Especially, I want to thank Dr. Yanke Che for helping me to start this project and for his continuous input and Dr. Xiaomei Yang for performing the Gaussian calculations to reveal the optimized geometries of the molecules involved in this dissertation. It is a great experience to work together with Dr. Chengyi Zhang, Dr. Zengxing Zhang, Dr. Ligui Li, Dr. Jimin Han, and also Benjamin Bunes, Miao Xu, Chen Wang, Daniel Jacobs, Yaqiong Zhang, and Na Wu in the same group.

We had a fruitful collaboration with Professor Zhonghua Peng's laboratory at the

Department of Chemistry at the University of Missouri-Kansas City on the work described in Chapter 3 and Professor Jeffrey Moore's laboratory at the Departments of Chemistry and Materials Science and Engineering at the University of Illinois at Urbana-Champaign on the work described in Chapter 4. I would like to thank Prof. Zhonghua Peng, Prof. Jeffrey Moore, Dr. Ching-En Chou, and Prof. Dustin Gross for providing experimental materials and helpful discussions regarding my research projects.

Finally, I would like to take the opportunity to thank my parents and my sister. Their continuous love, support, and encouragement give me the strength to accomplish my thesis work.

Financial support for the projects was provided by the NSF, the DHS, and the USTAR Program. Chapter 2 is reprinted with permission of the Journal of the American Chemical Society, 2011, 133, 1087–1091. Chapter 3 is reprinted with permission of the Journal of the American Chemical Society, 2013, 135, 16490–16496. Chapter 4 is reprinted with permission of ACS Applied Materials & Interfaces, 2013, 5, 7704–7708. Chapter 5 is reprinted with permission of Tetrahedron Letters, 2010, 51, 6651–6653.

CHAPTER 1

INTRODUCTION

1.1 Organic semiconductor materials in optoelectronic applications

Organic semiconductor materials have attracted numerous attention for their applications in organic light emitting diodes (OLEDs) [1–4], organic field effect transistors (OFETs) [5–10], organic solar cells (OSCs) [11–13], and sensors [14–16] due to their unique properties, such as low-cost solution fabrication combined with a flexible, lightweight, and adjustable energy level [17–20].

Since the discovery of the first conductive polymer material in 1977, numerous π-conjugated conductive materials have been developed [21–23]. Based on their majority charge carrier type, organic semiconductor materials can be classified as p-type (hole as the majority carrier) or n-type (electron as the majority carrier) materials (Figure 1.1).

For p-type semiconductor materials, the highest occupied molecular orbital (HOMO) is correlated to the ionization potential (IP) or the ability to donate an electron, therefore creating holes as the charge carriers. Pentacene (**1**) has an extraordinary high hole mobility up to 5 $cm^2V^{-1}s^{-1}$, which is one of the best hole transport materials [24]. However, the air-stability is not good enough due to the high lying HOMO energy level, which causes an air oxidation problem. By substituting the phenyl group in pentacene with the thiophene group, one can make pentathienoacene (**2**). This molecule has a low oxidation potential, a

high degree of conjugation, and a high degree of rigidity, which combined lead to air-stable, enhanced π-π interaction, efficient charge transport, and a charge mobility of 0.045 $cm^2V^{-1}s^{-1}$ [25]. In order to enhance the charge mobility, 2,6-diphenyl-thieno[3,2-b]thieno[2',3':4,5]-thieno[2,3-d]thiophene (**3**), a derivative of oligothienoacenes, was synthesized with an improved mobility value of 0.14 $cm^2V^{-1}s^{-1}$ [26]. By incorporating both phenyl ring and thiophene into a fused system, dibenzo[d,d']thieno[3,2-*b*:4,5-*b*']-dithiophene (**4**) can achieve an even higher mobility value (0.51 $cm^2V^{-1}s^{-1}$) [27]. Takimiya's group found that [1]-benzothieno[3,2-*b*][1]-benzothiophene is a promising structure to achieve good device performance. The phenyl substituted (**5**) [28] and alkyl substituted (**6**) [29] molecules can achieve high mobility levels of 2.0 $cm^2V^{-1}s^{-1}$ and 2.75 $cm^2V^{-1}s^{-1}$, respectively. Further expansion of the π-conjugated framework, dinaphtho[2,3-*b*:20,30-f]thieno[3,2-*b*]thiophene (**7**) has an even higher mobility level (2.9 $cm^2V^{-1}s^{-1}$), close to the record level of pentacene [30].

Contrast to the well-developed p-type semiconductor materials, the research of *n*-type material is relatively unexplored due its poor ambient stability and low electrical performance. In n-type semiconductor material, the major charge carrier is the electron. However, either H_2O or O_2, which commonly exist in the ambient condition, can trap the electrons in the material [31]. The lowest unoccupied molecular orbital (LUMO) level of n-type material is correlated to the electron affinity (EA) or the ability to accept an electron to act as a charge carrier, which can be used to predict the air stability of n-type semiconductor material.

Perfluorinated copper phthalocyanine (**8**) is one of the most investigated materials for air-stable n-type organic semiconductors due to its low LUMO level. However, the charge

carrier mobility (0.03 $cm^2V^{-1}s^{-1}$) is too low for application [32]. Oligo-polythiophenes have been widely used in fabrication of organic semiconductor devices due to their chemical stability and synthetic accessibility [33]. Thiophene derivatives (**9** and **10**) have shown good *n*-type semiconducting properties [31]. Recently, Bao's group used a solution processing method to grow large arrays of aligned C_{60} (**11**) single crystals, which can achieve the highest mobility (12 $cm^2V^{-1}s^{-1}$) for n-type semiconductors [34].

Aryl diimide material is another type of molecular structure having the n-type charge transport property [35]. Vapor deposited naphthalene tetracarboxylic diimide (NDI, **12**) film shows an exceptionally high mobility of 6 $cm^2V^{-1}s^{-1}$, which is one of the best values reported for organic semiconducting thin films [36]. Perylene tetracarboxylic diimide (PTCDI, **13**), as an extended conjugation system of NDI, can have a mobility up to 2.1 $cm^2V^{-1}s^{-1}$ in the crystalline phase; this high mobility is due to the intermolecular π-π interaction with a minimum interplanar spacing of 3.40 Å [37]. A solution-processable PTCDI derivative (**14**) was reported with a slightly lower mobility (1.3 $cm^2V^{-1}s^{-1}$) [38].

1.2 One-dimensional self-assembly nanostructures and materials

1.2.1 Influence of molecular packing on semiconductor properties

While the molecule structure of organic semiconductor materials can determine their HOMO and LUMO energy level (Table 1.1), the morphology control of molecular assembly may strongly affect the charge mobility in organic semiconductor materials [39]. This effect becomes even stronger in small molecule semiconductor materials [40]. The disordered nature of organic semiconductor materials causes the transport of carriers to occur through a hopping mechanism rather than a band-like transport. This charge transport

mechanism leads to the formation of localized electronic states, resulting in low charge mobility [19, 41–42]. The charge mobility of organic semiconductor materials are in the order of 10^{0}–10^{-8} $cm^2V^{-1}s^{-1}$ [43–46]. π-Conjugated molecular material represents one of the best performance organic semiconductors due to its excellent charge carrier mobility resulting from the large scale intermolecular π-π interactions [47].

For small molecule semiconductor materials, it is generally believed that grain boundaries will impede charge transport. Thus most of the research effort has been devoted to fabricate materials with large grain size [40, 48]. Under this background, single crystal material is one of most important candidates for organic field effect transistors due to its large grain size and high crystallinity. However, even within the single-crystalline organic material, the conductivity still varies significantly due to the different packing patterns. There are four orders of magnitude difference of mobility between the two-dimensional ordered brick-work packing of (triethylsilyl) ethynyl-substituted anthradithiophene (1 $cm^2V^{-1}s^{-1}$) and the one-dimensional ordered slipped packing (Figure 1.2) of (triisopropylsilyl)ethynyl substituted anthradithiophene (10^{-4} $cm^2V^{-1}s^{-1}$). The less ordered herringbone packing mode material even does not have measurable field-effect behavior [49]. Combined with other similar results from tetracene [50, 51] and oligothiophenes [52], it is reasonable to expect that the cofacial stacking pattern will maximize the π-π orbital overlap and enhance the charge mobility [40]. However, the majority of π-conjugated molecules tend to assemble in an edge-to-face fashion in the crystalline state [47]. It is necessary to develop a method to fabricate π-conjugated molecules into a cofacial stacking pattern.

1.2.2 One-dimensional self-assembly nanostructure fabrication methods

One-dimensional nanostructure (e.g., nanofiber) is an ideal nanomaterial candidate for investigating the structure-property relationship and elucidating the exciton diffusion and charge transport mechanism in nanoscale domain [53]. Due to the cofacial stacking pattern and high crystallinity in the material, nanofiber has enhanced charge transport properties compared with polycrystalline and amorphous 2D thin films. Substantial research has been done to fabricate inorganic one-dimensional nanostructures for enhanced device performance [54–58]. Compared with the inorganic counterparts, organic nanofibers have been less thoroughly studied [59]. Due to the difference in intermolecular interactions between the inorganic material (covalent bonding) and organic material (noncovalent bonding), different methods, such as molecular self-assembly, have been developed and used for fabrication of organic nanofiber structures.

1.2.2.1 Template method

The template method can be divided into two categories, hard template and soft template, based on the template material used during the processing. The hard template refers to inorganic material, such as mesoporous silica [60], particle track-etched membranes [61], and anodic aluminum oxide (AAO) [62]. The hard template material has a good control for the diameter and length of the nanofiber, and the density of the nanofiber arrays can be controlled by the pore-density in the template. However, the removal of the template normally requires strong acidic or basic etching, which often causes damage to the assembled nanomaterials.

The soft template method uses organic material as the template, representing a more

mild method for fabricating nanofibers. Block-copolymer and surfactant are commonly used as the soft template, which can self-assemble into nanoscale phase-separated domains by tuning the polymer composition and molecular structure [63, 64]. The template is afterwards removed through the solvent dissolution method. However, it is difficult to completely remove the template material through this method, and the template residues may increase the contact resistance [64, 65].

1.2.2.2 Physical vapor deposition

The physical vapor deposition method has been widely used for the fabrication of single-crystal small molecule materials [66]. This method can also be used to fabricate nanofiber material with high crystallinity [67–71]. However, only limited types of molecules have the ability to self-assemble into nanofiber structure by the physical vapor deposition method. The high temperature employed during this process often cause thermal destruction of the organic materials.

1.2.2.3 Solvent self-assembly method

Molecular self-assembly is an effective way to construct one-dimensional nanostructure through noncovalent intermolecular interaction, such as π-π interaction, dipole-dipole interaction, hydrogen bonding, and hydrophobic interaction. There are several advantages associated with this self-assembly method: (1) facile processing condition, (2) efficient and repeatable synthesis, and (3) easy morphology and composition control through molecule structure modification. Owing to these advantages, numerous nanofiber structures have been fabricated through solvent-phase self-assembly and used in

a wide range of optoelectronic devices, including OFETs [72, 73], OSCs [74], photodetectors [75, 76], and sensors [77, 78]. Unlimited molecular structure modification of the nanofibers provides an enormous option for the property and function improvement of these devices.

The self-assembly process can be performed either in bulk liquid phase or liquid/solid interface. For π-conjugated system, the driving force of one-dimensional self-assembling is mainly attributed to the intermolecular π-π interaction, in association with the hydrophobic (van der Waals) interaction between alkyl chains attached to the molecule core. Through cooperative optimization of these two interactions, well-defined organic nanofibers can be formed along the columnar π-π stacking direction [59].

The rapid solution dispersion method has been widely used for growing nanofibers in bulk liquid phase [79]. In this method, a small volume of concentrated solution of the molecules in a "good" solvent is injected into a "poor" solvent, where the sharp decrease in solubility results in rapid aggregation of the molecules, thus producing a large amount of nucleus sites in a very short time period. This rapid dilution and nucleation process prevent the formation of bulk crystal of the molecules, rather conducive to the growth of individual nanostructures, here specifically the nanofibers. The strong intermolecular π-π interaction facilitates the one-dimensional growth of the small nucleus along the π-π stacking direction [80]. Besides rapid solution dispersion, phase transfer, vapor diffusion, and seeded growth, sol-gel processing methods have also been used for nanofiber fabrication, depending on the structure of the building block molecule and the strength of the intermolecular interaction [59].

Solvent-vapor annealing is also an effective way to enable self-assembly at liquid-solid

interface, leading to the formation of well-defined nanofiber structures [81]. The annealing process is normally performed in a closed chamber saturated with solvent vapor. Depending on the molecular interaction and surface property, a solvent is chosen with appropriate polarity and solubility for the molecule, which allows for sufficient mobility for the molecules to transport on the surface of the substrate.

1.2.3 Applications of one-dimensional self-assembly materials

The cofacial molecular stacking pattern in the nanofiber structure leads to one-dimensional confinement and enhancement of exciton diffusion and charge transport. These unique optical and electrical properties render the wide applications of nanofiber materials in optoelectronic devices, including photodetectors [82–84], sensors [77, 85–92], OLED [93, 94], OFET [72, 73], photovoltaics [95, 96], and nanophotonics [97, 98]. Herein we will refine our discussion mainly on the applications in photodetectors, optical sensors, and electrical sensors, which are more relevant to my thesis research.

1.2.3.1 Photodetectors

One-dimensional photoconductive materials are used to fabricate photodetector devices. The conductivity of photoconductive material can be enhanced under light illumination. Photoconductive nanomaterials serve as an important platform for investigating the photo-electrical process, such as charge generation and charge transport.

Several materials have been used to fabricate photodetectors. By using anodic aluminum oxide (AAO) as a template, poly[9,9-dioctylfluorenyl-2,7-diyl)-co-[bithiophene)] has been fabricated into nanofibers with a diameter of 200 nm. The

photoconductivity of a single nanowire was measured by a near-field scanning optical microscope. The measured photoresponsivity of a single nanofiber was 0.4 mA/W, which is comparable to the value of inorganic nanowires [82]. Nanowires of copper (II) hexadecafluorophthalocyanine (F16CuPc) have been fabricated through physical vapor deposition and used as photoswitches and phototransistors. The photoconductivity gain achieved can be as high as 10^5 under V_{gs} = -6 V [83].

Recently, Samorì's group used solution processing to fabricate organic phototransistors based on PTCDI molecules. The photoresponsivity of these materials was found to be correlated to the channel length and device geometry. The highest photoresponsivity value of 4.08×10^5 A/W was achieved on a multifiber-based device [84].

1.2.3.2 Optical sensors

Due to their large surface area, nanofibers have been widely used in sensor devices, especially for chemical vapor detection. Based on the different signal modulation employed in the experiments, the sensor systems can be categorized into optical mode or electrical mode.

In the optical mode, the intermolecular π-π stacking along the long axis of the nanofiber leads to enhanced exciton migration, which enables the amplified fluorescence quenching as shown in Figure 1.3. When a quenching molecule (e.g., the target analyte) is absorbed on the nanofiber surface, any exciton generated within the diffusion length can be quenched by the quenching molecule. Based on this mechanism, Zang's group has developed a series of sensor molecules and fabricated them into nanofibers for detection of nitro-based explosives or amines.

The well-defined fluorescence nanofibril sensory material was fabricated from N-(1-hexylheptyl)perylene-3,4,9,10-tetracarboxyl-3,4-anhydride-9,10-imide with high sensitivity, selectivity, and photostability [85]. This molecule possesses a good balance between the molecular stacking and the fluorescence yield (15%) of the materials thus assembled. The former prefers a molecular structure with minimal steric hindrance (usually referring to a small or linear side chain), while the latter favors bulky, branched side chains that may distort the π-π stacking to afford increased fluorescence (by enhancing the low-energy excitonic transition) for the molecular assembly [79, 80, 99]. After deposition onto the substrate, the entangled nanofibers form a meshlike, highly porous film, which enables expedient diffusion of gaseous analyte molecules within the thin matrix. The combination of strong fluorescence and large surface area enables development of a fluorescence sensor for detecting reductive volatile organic compounds (VOCs), such as organic amines, through a photoinduced electron transfer process-based fluorescence quenching (Figure 1.4) [85]. The driving force for the photoinduced electron transfer process is the energy difference between the HOMO of aniline and the HOMO of PTCDI. Upon exposure to the saturated vapor of aniline (880 ppm), the fluorescence of the nanofibril film can be quenched completely. The detection limit for this sensor material can be projected as low as 200 ppt. The sensitivity of the nanofibril film was largely enhanced by decreasing the size of the nanofibers. The enhanced fluorescence sensing is mainly due to the increased surface area and the enhanced exciton diffusion along the long axis of nanofiber. With an optimized loading of nanofibril material, the detection limit is projected as low as 5 ppt [86].

Similar fluorescence sensing of gaseous molecules was also achieved with nanofiber

fabricate from AEMs (arylene ethynylene macrocycles). AEM molecules demonstrate strong electron-donating ability, which enables effective sensing of oxidative reagents (such as trinitrotoluene (TNT)) through electron-transfer-based fluorescence quenching. Upon deposition onto a suitable substrate, the AEM nanofibers form porous film structure not only provides increased surface area for enhanced adsorption of gaseous molecules, but also enables expedient diffusion of guest molecules across the film matrix. The detection limit for TNT was projected as low as 10 ppt for the AEM-based fluorescence sensor material [87]. The AEM-based material can also be used as fluorescence sensor for 2,3-dimethyl-2,3-dinitrobutane (DMNB) at very low vapor pressure [88]. Recently, a selective detection of trace amounts of TNT was achieved using AEM-based nanoporous fibers. The slow diffusion and strong encapsulation of TNT molecules within the nanopores result in a further fluorescence quenching of the material after removal from the TNT vapor source. Under the same testing conditions, other common nitroaromatic explosives and oxidizing reagents did not demonstrate this postexposure fluorescence quenching; rather, a recovery of fluorescence was observed [77].

Besides AEMs, a new type of carbazole trimer molecules has also been fabricated into nanofibers and used for trace vapor detection of explosives [89]. These nanofibers demonstrated efficient, fast fluorescent sensing not only for nitroaromatic explosives (e.g., TNT, 2,4-Dinitrotoluene (DNT)), but also for nitroaliphatic explosives (e.g., nitromethane), which remain difficult to detect due to their high volatility and low vapor condensation to many sensory materials.

1.2.3.3 Electrical sensor

One-dimensional organic nanostructures assembled via π-π interactions present promising candidates for highly conductive materials. The enhanced charge carrier mobility is usually maximized along the direction of cofacial stacking of the molecules through the delocalization of π electrons [90, 100, 101]. The combination of the long range charge transport channels and the large surface area resulting from the mesh-like network structures enables effective vapor sensing properties for nanofibers material.

When n-type PTCDI nanofiber is exposed to the vapor of hydrazine (a strong electron donor), the efficient intermolecular electron transfer between PTCDI and hydrazine leads to the formation of the anionic radical of PTCDI. The π-electron delocalization along the long axis of molecular stacking has been observed by electron spin resonance spectroscopy. The increased charge carrier density of PTCDI nanofiber along with the ordered one-dimensional π-electron delocalization leads to enhanced conductivity. The enhanced conductivity in this case can reach 1.0×10^{-3} S/m, which is much higher than that obtained for polymer nanowires. The electrical current can increase by more than three orders of magnitude upon exposure to hydrazine vapor, which makes PTCDI nanofibers promising sensor materials for hydrazine and other amines [90, 91].

For p-type AEM nanofibers, the hole is the major charge carrier. Under light illumination the AEM molecule can donate an electron to the absorbed oxygen molecule, leading to an increase in hole density within the nanofiber. Such increase in electrical conductivity under light is referred as photoconductivity. Organic amines have stronger electron donating ability than AEM molecules. When AEM nanofiber is exposed to amine vapor, interfacial electron transfer will occur from amine to the oxidized AEM molecule

(i.e., a process similar to the hole depletion in semiconductor materials), thereby resulting in a decrease in electrical conductivity. This decreased conductivity can be used as a sensor signal for vapor detection of amines [92].

1.3 Photoconductive mechanism

Photoconductive effect refers to the phenomena that electrical conductivity is enhanced under light illumination. Photoconductive effect has been explored and studied for organic semiconductor materials, aiming to investigate the fundamental mechanism and process of photoinduced charge generation. Many optoelectronic devices, such as photodetectors, have been fabricated from organic materials based on the photoconductive effect. The mechanism of photoconductivity can be described as two subsequent processes: charge generation and charge transport, as illustrated in Figure 1.5 [19].

1.3.1 Charge-generation process

For the charge generation process, it includes three rapid, interrelated steps: absorption of a photon leading to the formation of bound electron-hole pairs (excitons), excitons diffusion to the donor/acceptor (D/A) interface, and dissociation into free charges at the interface [20]. Because organic semiconductor materials usually have a very large absorption coefficient, they can absorb most incident photons even with very thin film (<100 nm) [102]. After absorbing the light, the photoexcitation of organic semiconductor material leads to the formation of excitons rather than free charge carriers due to its much lower dielectric constant compared with the inorganic counterparts [103]. It has been estimated that only 10% of the photoexcitations lead to free charge carriers in bulk

conjugated polymers material [104]. The efficient dissociation of excitons can only occur at the D/A interface, where strong local electrical fields are formed due to the abrupt changes of the potential energy [19]. Thus, the separation distance between the donor and acceptor should be at the range of the exciton diffusion length (10–20 nm) to ensure the exciton diffusion to the interface within its lifetime [105]. Otherwise, the excitons will decay through radiative or nonradiative ways before reaching the interface. For the fabrication of efficient photodetectors, it is necessary to improve the efficiency of charge generation processes by controlling the distance between the D/A interfaces [20].

1.3.2 Charge-transport process

Once generated in the photoexcitation process, the free charges (both electron and hole) must transport to the electrodes to finish the whole function cycle of a device (e.g., photodetector, photoconductive sensors). Organic semiconductors have much weaker intermolecular interactions than the inorganic semiconductors and thus possess more localized charge carriers and lower carrier mobility [106]. The low charge carrier mobility of organic semiconductors also result from the nature of the disordered molecular packing mode, which enforces the carriers transport through the hopping mechanism rather than the bandlike transport [42]. For example, poly(3-hexylthiophene) (P3HT), one of the commonly used conjugated polymer materials in organic solar cells, has a hole mobility value of only 0.1–0.5 $cm^2V^{-1}s^{-1}$, which is more than three orders of magnitude lower than the value of crystalline silicon (475 $cm^2V^{-1}s^{-1}$) [42, 107]. In order to improve the photoconductivity of organic semiconductors, it is essential to develop a material that has better charge transport properties [42].

In general, the efficiency of organic photoconductive devices (like photodetectors and solar cells) is significantly lower than their inorganic counterparts. For example, typical organic solar cells have photoconversion efficiency around 10%, which is still much lower than efficiency obtained for the inorganic solar cells fabricated from silicon, cadmium telluride (CdTe), and copper indium gallium (di) selenide (CIGS) [108]. Both charge generation and charge transport processes play important roles in determining the photoconversion efficiency [109]. It is imperative to improve the efficiency of both the two processes cooperatively in order to improve the photoconductivity of organic materials.

1.4 One-dimensional heterojunction

Heterojunctions are structures where two different (typically n-type and p-type) semiconductor materials are interfaced together. Heterojunctions often possess different electronic properties that are not available within homojunction structures [110]. The dielectric constant for most organic semiconductor materials is in the range of 3.5–5.5, which are much smaller than the values of silicon (11.9) [19]. The low dielectric constant is not conducive to the charge separation of the photogenerated excitons. To this end, introduction of D/A interface becomes critical for achieving high efficiency of charge separation and eventually improving the device performance.

One-dimensional heterojunction structure (e.g., composite of n-type and p-type nanofibers) has a large interface area to facilitate charge generation while still maintaining single-crystalline structure (i.e., organized molecular packing) to assure efficient charge transport pathway along the long axis. Combination of these unique features makes nanofiber heterojunction an ideal candidate for photodetectors, as well as other

optoelectronic devices [20].

1.4.1 Inorganic one-dimensional heterojunction

One-dimensional inorganic heterojunction structure has been well studied for its applications in OLEDs [111], OFETs [112], and OSCs [113–115]. In 2007, Lieber's group reported the p-type/intrinsic/n-type coaxial silicon nanowire solar cells, with a power conversion efficiency of 3.4% and maximal power output of up to 200 pW per nanowire device [113]. Yang's group fabricated polythiophene grafted ZnO heterojunction nanowires, which provide an effective platform to study the photo-electrical process [114].

1.4.2 Organic one-dimensional heterojunction

Compared with the inorganic counterpart, organic nanofibril heterojunction has been much less explored, mainly due to the challenge of formation of good contact between donor and acceptor materials [116]. Unlike traditional inorganic heterojunction materials that can be fabricated with hard template or reactive ion etching techniques, organic materials are usually fragile and cannot be processed under these harsh conditions [117–119]. To overcome these technical hurdles, physical vapor transport and solvent self-assembly have been widely used in fabricating organic nanofibril heterojunctions.

1.4.2.1 Physical vapor transport method

By using physical vapor transport (PVT) techniques, copper phthalocyanine (CuPc, as donor) and copper hexadecafluorophthalocyanine (F16CuPc, acceptor) single crystalline p-n junction nanoribbons were fabricated with ambipolar transport (Figure 1.6). However,

due to mismatch between the energy levels of donor and acceptor, the photoconversion efficiency of this single nanowire device is only 0.007% [120]. In order to improve the efficiency of this type of heterojunction, the energy levels were modified by using CuPc and 5,10,15,20-tetra(4-pyridyl)-porphyrin (H_2TPyP) instead. When fabricated into a nanofiber p-n junction, a single fiber device demonstrated an improved photoconversion efficiency with 0.08% [116].

1.4.2.2 Solvent self-assembly method

Compared with the PVT method, molecular self-assembly in solution is a more mild and adaptable method for fabricating one-dimensional heterojunctions [59, 121, 122]. The material can be categorized as n-type or p-type based on the self-assembly moiety.

For p-type materials, hexabenzocoronene (HBC) represents as a good electron-donating π-conjugated molecule, which can self-assemble into nanotube structure to be suited for hole-transport properties. Aida's group has synthesized a HBC molecule appended with trinitrofluorenone as side chains (Figure 1.7). This molecule was found to self-assemble into a one-dimensional heterojunction structure in the morphology of a nanotube, which demonstrated a highly efficient photoconductive response with a more than 10^4 on/off ratio [110, 123–126]. Furthermore, in a 2009 paper, the author attached C60 moiety to the HBC molecule to approach ambipolar transistor properties [124]. Besides HBC building-blocks, the author also synthesized porphyrin derivatives and fabricated them into photoconductive nanofibers with amipolar charge-carrier mobility [127, 128].

As an n-type material naphthalenediimide (NDI) has also been explored extensively

for molecular self-assembly, aiming to produce heterojunction nanostructures. Matile's group used NDI molecules to fabricate heterojunction nanostructures on surface [129, 130]. Parquette's group synthesized a bolaamphiphile molecule containing tetraphenylporphyrin (TPP) and NDI parts and self-assembled the molecule into a nanotubular heterojunction structure (Figure 1.8) [131]. Samori's group synthesized a molecule combining HBC with perylene monoimide (PMI), which is linked by the ethinylene group. The self-assembled heterojunction structure from this new molecule showed balanced ambipolar transistor behavior (Figure 1.9) [132], Photoconductivity of these materials was studied by Kelvin probe force microscopy (KPFM) [133].

PTCDI molecules have also widely been used as building-blocks to fabricate one-dimensional heterojunction nanostructures. Hydrogen-bonded oligo(p-phenylene vinylene)s (OPVs) and PTCDI parts can coassemble into nanosupercoils, which exhibit photoinduced electron transfer on subpicosecond time scale [134]. Spiro-substituted PTCDI molecule can self-assembled into ultralong nanowires with an aspect ratio as high as 9200 [135]. Recently, Zang's group has fabricated well-defined ultrathin nanoribbons from an amphiphilic electron donor-acceptor supramolecule based on PTCDI (Figure 1.10) [136]. These nanoribbons demonstrate high photoconductivity and sensing efficiency for vapor detection of nitro-based explosives. However, these one-dimensional heterojunction structures were fabricated from the covalently linked D-A moieties, which require complicated molecular design and synthesis. Moreover, the complicated molecular structure and more flexible configuration make the self-assembly process more challenging regarding production of well-defined nanostructures with optimized intermolecular arrangement to minimize charge recombination.

1.5 Motivation and objectives

One-dimensional organic nanostructures assembled via π-π interactions have been proven to be a promising candidate for highly photoconductive materials due to their enhanced charge carrier mobility along the π-π stacking [100, 137–140]. However, only a few examples of photoconductive one-dimensional nanostructures have thus far been reported [11, 14, 123, 141–143], and most of the reported structures are focused on the covalently linked D-A molecules [11, 14, 123, 141]. Obvious disadvantages of these systems include complicated molecular design and synthesis and challenges in optimization of the intermolecular assembly so as to avoid charge carrier recombination, which make these materials impractical in large-scale applications. Therefore, it is highly demanded to develop simple and flexible methods to fabricate photoconductive organic materials.

PTCDI (n-type) and arylene ethynylene macrocycle (AEM, p-type) are two representative building-blocks for fabricating one-dimensional nanostructures due to their strong intermolecular π-π interaction and rigid planar molecule geometry (Figure 1.11). PTCDI has attracted great interest not only for its thermal and photochemical stability [144], but also for its extraordinary optoelectronic properties [99, 145]. Due to its strong absorption coefficient ($>7 \times 10^4\ M^{-1}cm^{-1}$) in the visible range and singlet fission phenomena observed in the solid state [146], PTCDI has been extensively studied and applied in organic photovoltaics. Shape-persistent AEMs can self-assemble into nanotubular structures; these tubular structures can detect chemical vapor with a very low detection limit [77, 147]. Taking on these unique features of PTCDI and AEM, we were motivated to fabricate these two classes of molecules into nanofibril heterojunction materials, which

are expected to yield enhanced conductivity when coated with electron donor (or acceptor) molecules on the surface.

The goal of this research is to investigate the structure-property relationship of D/A heterojunction nanomaterials by designing and synthesizing functional building block molecules, self-assembling the molecules into well-defined nanofibers, fabricating the nanofibers into optical and electrical devices, and testing their photoconductivity and sensor properties. The primary objectives of this research are to address the central problems in the field of organic electronics by investigating

(1) A new facile and efficient approach to fabricate nanofibril heterojunction through interfacial engineering,

(2) The effect of donor molecular structure and morphology on photoconductivity of nanofibril heterojunction,

(3) The design of an alternative nanofibril heterojunction through surface coating to achieve high dark conductivity and application in the VOC sensor,

(4) A new synthetic method for large scale production of the monoimides of PTCDI, which are the precursor for making a variety of perylene based building block molecules.

1.6 References

[1] Zhu, X.-H.; Peng, J.; Cao, Y.; Roncali, J. *Chem. Soc. Rev.* **2011**, *40*, 3509–3524.

[2] Grimsdale, A. C.; Leok Chan, K.; Martin, R. E.; Jokisz, P. G.; Holmes, A. B. *Chem. Rev.* **2009**, *109*, 897–1091.

[3] Kulkarni, A. P.; Tonzola, C. J.; Babel, A.; Jenekhe, S. A. *Chem. Mater.* **2004**, *16*, 4556–4573.

[4] Friend, R. H.; Gymer, R. W.; Holmes, A. B.; Burroughes, J. H.; Marks, R. N.; Taliani, C.; Bradley, D. D. C.; Santos, D. A. D.; Bredas, J. L.; Logdlund, M.; Salaneck, W. R. *Nature* **1999**, *397*, 121–128.

[5] Mei, J.; Diao, Y.; Appleton, A. L.; Fang, L.; Bao, Z. *J. Am. Chem. Soc.* **2013**, *135*, 6724–6746.

[6] Zaumseil, J.; Sirringhaus, H. *Chem. Rev.* **2007**, *107*, 1296–1323.

[7] Klauk, H. *Chem. Soc. Rev.* **2010**, *39*, 2643–2666.

[8] Coropceanu, V.; Cornil, J.; da Silva Filho, D. A.; Olivier, Y.; Silbey, R.; Brédas, J.-L. *Chem. Rev.* **2007**, *107*, 926–952.

[9] Shirota, Y.; Kageyama, H. *Chem. Rev.* **2007**, *107*, 953–1010.

[10] Arias, A. C.; MacKenzie, J. D.; McCulloch, I.; Rivnay, J.; Salleo, A. *Chem. Rev.* **2010**, *110*, 3–24.

[11] Yamamoto, Y.; Zhang, G.; Jin, W.; Fukushima, T.; Ishii, N.; Saeki, A.; Seki, S.; Tagawa, S.; Minari, T.; Tsukagoshi, K.; Aida, T. *Proc. Natl. Acad. Sci.* **2009**, *106*, 21051–21056.

[12] Charvet, R.; Acharya, S.; Hill, J. P.; Akada, M.; Liao, M.; Seki, S.; Honsho, Y.; Saeki, A.; Ariga, K. *J. Am. Chem. Soc.* **2009**, *131*, 18030–18031.

[13] Clarke, T. M.; Durrant, J. R. *Chem. Rev.* **2010**, *110*, 6736–6767.

[14] Che, Y.; Yang, X.; Liu, G.; Yu, C.; Ji, H.; Zuo, J.; Zhao, J.; Zang, L. *J. Am. Chem. Soc.* **2010**, *132*, 5743–5750.

[15] Che, Y.; Yang, X.; Zhang, Z.; Zuo, J.; Moore, J. S.; Zang, L. *Chem. Commun.* **2010**, *46*, 4127–4129.

[16] Zhang, X.; Jie, J.; Zhang, W.; Zhang, C.; Luo, L.; He, Z.; Zhang, X.; Zhang, W.; Lee, C.; Lee, S. *Adv. Mater.* **2008**, *20*, 2427–2432.

[17] Lewis, N. S. *Science* **2007**, *315*, 798–801.

[18] Service, R. F. *Science* **2011**, *332*, 293.

[19] Hains, A. W.; Liang, Z.; Woodhouse, M. A.; Gregg, B. A. *Chem. Rev.* **2010**, *110*, 6689–6735.

[20] Günes, S.; Neugebauer, H.; Sariciftci, N. S. *Chem. Rev.* **2007**, *107*, 1324–1338.

[21] Shirakawa, H.; Louis, E. J.; MacDiarmid, A. G.; Chiang, C. K.; Heeger, A. J. *Chem. Commun.* **1977**, 578–580.

[22] Facchetti, A. *Mater. Today* **2007**, *10*, 28–37.

[23] Chiang, C. K.; Fincher, C. R.; Park, Y. W.; Heeger, A. J.; Shirakawa, H.; Louis, E. J.; Gau, S. C.; MacDiarmid, A. G. *Phy. Rev. Lett.* **1977**, *39*, 1098–1101.

[24] Virkar, A.; Mannsfeld, S.; Oh, J. H.; Toney, M. F.; Tan, Y. H.; Liu, G.-y.; Scott, J. C.; Miller, R.; Bao, Z. *Adv. Funct. Mater.* **2009**, *19*, 1962–1970.

[25] Xiao, K.; Liu, Y.; Qi, T.; Zhang, W.; Wang, F.; Gao, J.; Qiu, W.; Ma, Y.; Cui, G.; Chen, S.; Zhan, X.; Yu, G.; Qin, J.; Hu, W.; Zhu, D. *J. Am. Chem. Soc.* **2005**, *127*, 13281–13286.

[26] Liu, Y.; Wang, Y.; Wu, W.; Liu, Y.; Xi, H.; Wang, L.; Qiu, W.; Lu, K.; Du, C.; Yu, G. *Adv. Funct. Mater.* **2009**, *19*, 772–778.

[27] Gao, J. H.; Li, R. J.; Li, L. Q.; Meng, Q.; Jiang, H.; Li, H. X.; Hu, W. P. *Adv. Mater.* **2007**, *19*, 3008–3011.

[28] Takimiya, K.; Ebata, H.; Sakamoto, K.; Izawa, T.; Otsubo, T.; Kunugi, Y. *J. Am. Chem. Soc.* **2006**, *128*, 12604–12605.

[29] Ebata, H.; Izawa, T.; Miyazaki, E.; Takimiya, K.; Ikeda, M.; Kuwabara, H.; Yui, T. *J. Am. Chem. Soc.* **2007**, *129*, 15732–15733.

[30] Yamamoto, T.; Takimiya, K. *J. Am. Chem. Soc.* **2007**, *129*, 2224–2225.

[31] Jones, B. A.; Facchetti, A.; Wasielewski, M. R.; Marks, T. J. *J. Am. Chem. Soc.* **2007**, *129*, 15259–15278.

[32] Yoon, M.-H.; Kim, C.; Facchetti, A.; Marks, T. J. *J. Am. Chem. Soc.* **2006**, *128*, 12851–12869.

[33] Bao, Z.; Dodabalapur, A.; Lovinger, A. J. *Appl. Phys. Lett.* **1996**, *69*, 4108–4110.

[34] Li, H.; Tee, B. C. K.; Cha, J. J.; Cui, Y.; Chung, J. W.; Lee, S. Y.; Bao, Z. *J. Am. Chem. Soc.* **2012**, *134*, 2760–2765.

[35] Usta, H.; Facchetti, A.; Marks, T. J. *Acc. Chem. Res.* **2011**, *44*, 501–510.

[36] Shukla, D.; Nelson, S. F.; Freeman, D. C.; Rajeswaran, M.; Ahearn, W. G.; Meyer, D. M.; Carey, J. T. *Chem. Mater.* **2008**, *20*, 7486–7491.

[37] Tatemichi, S.; Ichikawa, M.; Koyama, T.; Taniguchi, Y. *Appl. Phys. Lett.* **2006**, *89*, 112108–112103.

[38] Soeda, J.; Uemura, T.; Mizuno, Y.; Nakao, A.; Nakazawa, Y.; Facchetti, A.; Takeya, J. *Adv. Mater.* **2011**, *23*, 3681–3685.

[39] Tsao, H. N.; Mullen, K. *Chem. Soc. Rev.* **2010**, *39*, 2372–2386.

[40] Mas-Torrent, M.; Rovira, C. *Chem. Rev.* **2011**, *111*, 4833–4856.

[41] Mishra, A.; Bäuerle, P. *Angew. Chem. Int. Ed.* **2012**, *51*, 2020–2067.

[42] Coakley, K. M.; McGehee, M. D. *Chem. Mater.* **2004**, *16*, 4533–4542.

[43] Sirringhaus, H.; Brown, P. J.; Friend, R. H.; Nielsen, M. M.; Bechgaard, K.; Langeveld-Voss, B. M. W.; Spiering, A. J. H.; Janssen, R. A. J.; Meijer, E. W.; Herwig, P.; de Leeuw, D. M. *Nature* **1999**, *401*, 685–688.

[44] Braun, D. *Mater. Today* **2002**, *5*, 32–39.

[45] Mihailetchi, V. D.; van Duren, J. K. J.; Blom, P. W. M.; Hummelen, J. C.; Janssen, R. A. J.; Kroon, J. M.; Rispens, M. T.; Verhees, W. J. H.; Wienk, M. M. *Adv. Funct. Mater.* **2003**, *13*, 43–46.

[46] Mihailetchi, V. D.; Koster, L. J. A.; Blom, P. W. M.; Melzer, C.; de Boer, B.; van Duren, J. K. J.; Janssen, R. A. J. *Adv. Funct. Mater.* **2005**, *15*, 795–801.

[47] Wu, W.; Liu, Y.; Zhu, D. *Chem. Soc. Rev.* **2010**, *39*, 1489–1502.

[48] Wang, C.; Dong, H.; Hu, W.; Liu, Y.; Zhu, D. *Chem. Rev.* **2011**, *112*, 2208–2267.

[49] Payne, M. M.; Parkin, S. R.; Anthony, J. E.; Kuo, C.-C.; Jackson, T. N. *J. Am. Chem. Soc.* **2005**, *127*, 4986–4987.

[50] Moon, H.; Zeis, R.; Borkent, E.-J.; Besnard, C.; Lovinger, A. J.; Siegrist, T.; Kloc, C.; Bao, Z. *J. Am. Chem. Soc.* **2004**, *126*, 15322–15323.

[51] Chi, X.; Li, D.; Zhang, H.; Chen, Y.; Garcia, V.; Garcia, C.; Siegrist, T. *Org. Electron.* **2008**, *9*, 234–240.

[52] Reese, C.; Roberts, M. E.; Parkin, S. R.; Bao, Z. *Adv. Mater.* **2009**, *21*, 3678–3681.

[53] Kim, F. S.; Ren, G.; Jenekhe, S. A. *Chem. Mater.* **2011**, *23*, 682–732.

[54] Hu, J.; Odom, T. W.; Lieber, C. M. *Acc. Chem. Res.* **1999**, *32*, 435–445.

[55] Cui, Y.; Lieber, C. M. *Science* **2001**, *291*, 851–853.

[56] Pan, Z. W.; Dai, Z. R.; Wang, Z. L. *Science* **2001**, *291*, 1947–1949.

[57] Yin, Y.; Alivisatos, A. P. *Nature* **2005**, *437*, 664–670.

[58] Hochbaum, A. I.; Yang, P. *Chem. Rev.* **2009**, *110*, 527–546.

[59] Zang, L.; Che, Y.; Moore, J. S. *Acc. Chem. Res.* **2008**, *41*, 1596–1608.

[60] Wu, C.-G.; Bein, T. *Science* **1994**, *264*, 1757–1759.

[61] Cai, Z.; Lei, J.; Liang, W.; Menon, V.; Martin, C. R. *Chem. Mater.* **1991**, *3*, 960–967.

[62] C. Hulteen, J.; Martin, C. R. *J. Mater. Chem.* **1997**, *7*, 1075–1087.

[63] Chai, J.; Buriak, J. M. *ACS Nano* **2008**, *2*, 489–501.

[64] Jang, J.; Yoon, H. *Chem. Commun.* **2003**, 720–721.

[65] Lee, J. I.; Cho, S. H.; Park, S.-M.; Kim, J. K.; Kim, J. K.; Yu, J.-W.; Kim, Y. C.; Russell, T. P. *Nano. Lett.* **2008**, *8*, 2315–2320.

[66] Briseno, A. L.; Mannsfeld, S. C. B.; Ling, M. M.; Liu, S.; Tseng, R. J.; Reese, C.; Roberts, M. E.; Yang, Y.; Wudl, F.; Bao, Z. *Nature* **2006**, *444*, 913–917.

[67] Tang, Q.; Li, H.; He, M.; Hu, W.; Liu, C.; Chen, K.; Wang, C.; Liu, Y.; Zhu, D. *Adv. Mater.* **2006**, *18*, 65–68.

[68] Tang, Q.; Li, H.; Liu, Y.; Hu, W. *J. Am. Chem. Soc.* **2006**, *128*, 14634–14639.

[69] Tang, Q.; Li, H.; Song, Y.; Xu, W.; Hu, W.; Jiang, L.; Liu, Y.; Wang, X.; Zhu, D. *Adv. Mater.* **2006**, *18*, 3010–3014.

[70] Tang, Q.; Tong, Y.; Hu, W.; Wan, Q.; Bjørnholm, T. *Adv. Mater.* **2009**, *21*, 4234–4237.

[71] Zhao, Y. S.; Wu, J.; Huang, J. *J. Am. Chem. Soc.* **2009**, *131*, 3158–3159.

[72] Oh, J. H.; Lee, H. W.; Mannsfeld, S.; Stoltenberg, R. M.; Jung, E.; Jin, Y. W.; Kim, J. M.; Yoo, J.-B.; Bao, Z. *Proc. Natl. Acad. Sci.* **2009**, *106*, 6065–6070.

[73] Briseno, A. L.; Mannsfeld, S. C. B.; Reese, C.; Hancock, J. M.; Xiong, Y.; Jenekhe, S. A.; Bao, Z.; Xia, Y. *Nano. Lett.* **2007**, *7*, 2847–2853.

[74] Li, L.; Jacobs, D. L.; Bunes, B. R.; Huang, H.; Yang, X.; Zang, L. *Polym. Chem.* **2014**, *5*, 309–313.

[75] Che, Y.; Huang, H.; Xu, M.; Zhang, C.; Bunes, B. R.; Yang, X.; Zang, L. *J. Am. Chem. Soc.* **2011**, *133*, 1087–1091.

[76] Huang, H.; Chou, C.-E.; Che, Y.; Li, L.; Wang, C.; Yang, X.; Peng, Z.; Zang, L. *J. Am. Chem. Soc.* **2013**, *135*, 16490–16496.

[77] Che, Y.; Gross, D. E.; Huang, H.; Yang, D.; Yang, X.; Discekici, E.; Xue, Z.; Zhao, H.; Moore, J. S.; Zang, L. *J. Am. Chem. Soc.* **2012**, *134*, 4978–4982.

[78] Huang, H.; Gross, D. E.; Yang, X.; Moore, J. S.; Zang, L. *ACS Appl. Mater. Interfaces* **2013**, *5*, 7704–7708.

[79] Balakrishnan, K.; Datar, A.; Oitker, R.; Chen, H.; Zuo, J.; Zang, L. *J. Am. Chem. Soc.* **2005**, *127*, 10496–10497.

[80] Balakrishnan, K.; Datar, A.; Naddo, T.; Huang, J.; Oitker, R.; Yen, M.; Zhao, J.; Zang, L. *J. Am. Chem. Soc.* **2006**, *128*, 7390–7398.

[81] Datar, A.; Oitker, R.; Zang, L. *Chem. Commun.* **2006**, 1649–1651.

[82] O'Brien, G. A.; Quinn, A. J.; Tanner, D. A.; Redmond, G. *Adv. Mater.* **2006**, *18*, 2379–2383.

[83] Tang, Q.; Li, L.; Song, Y.; Liu, Y.; Li, H.; Xu, W.; Liu, Y.; Hu, W.; Zhu, D. *Adv. Mater.* **2007**, *19*, 2624–2628.

[84] Gemayel, M. E.; Treier, M.; Musumeci, C.; Li, C.; Müllen, K.; Samorì, P. *J. Am. Chem. Soc.* **2012**, *134*, 2429–2433.

[85] Che, Y.; Yang, X.; Loser, S.; Zang, L. *Nano Lett.* **2008**, *8*, 2219–2223.

[86] Che, Y.; Zang, L. *Chem. Commun.* **2009**, 5106–5108.

[87] Naddo, T.; Che, Y.; Zhang, W.; Balakrishnan, K.; Yang, X.; Yen, M.; Zhao, J.; Moore, J. S.; Zang, L. *J. Am. Chem. Soc.* **2007**, *129*, 6978–6979.

[88] Naddo, T.; Yang, X.; Moore, J. S.; Zang, L. *Sens. Actuators, B* **2008**, *B134*, 287–291.

[89] Zhang, C.; Che, Y.; Yang, X.; Bunes, B. R.; Zang, L. *Chem. Commun.* **2010**, *46*, 5560–5562.

[90] Che, Y.; Datar, A.; Yang, X.; Naddo, T.; Zhao, J.; Zang, L. *J. Am. Chem. Soc.* **2007**, *129*, 6354–6355.

[91] Che, Y.; Datar, A.; Balakrishnan, K.; Zang, L. *J. Am. Chem. Soc.* **2007**, *129*, 7234–7235.

[92] Che, Y.; Yang, X.; Zhang, Z.; Zuo, J.; Moore, J. S.; Zang, L. *Chem. Commun.* **2010**, *46*, 4127–4129.

[93] Xu, G.; Tang, Y.-B.; Tsang, C.-H.; Zapien, J.-A.; Lee, C.-S.; Wong, N.-B. *J. Mater. Chem.* **2010**, *20*, 3006–3010.

[94] Ng, A. M.-C.; Djurišić, A. B.; Tam, K.-H.; Kwok, W.-M.; Chan, W.-K.; Tam, W. Y.; Phillips, D. L.; Cheah, K.-W. *Adv. Funct. Mater.* **2008**, *18*, 566–574.

[95] Schmidt-Mende, L.; Fechtenkötter, A.; Müllen, K.; Moons, E.; Friend, R. H.; MacKenzie, J. D. *Science* **2001**, *293*, 1119–1122.

[96] Karak, S.; Ray, S. K.; Dhar, A. *Appl. Phys. Lett.* **2010**, *97*, 043306.

[97] Che, Y.; Yang, X.; Balakrishnan, K.; Zuo, J.; Zang, L. *Chem. Mater.* **2009**, *21*, 2930–2934.

[98] Zhang, C.; Zou, C.-L.; Yan, Y.; Hao, R.; Sun, F.-W.; Han, Z.-F.; Zhao, Y. S.; Yao, J. *J. Am. Chem. Soc.* **2011**, *133*, 7276–7279.

[99] Wurthner, F. *Chem. Commun.* **2004**, 1564–1579.

[100] Coropceanu, V.; Cornil, J.; Da Silva Filho, D. A.; Olivier, Y.; Silbey, R.; Bredas, J.-L. *Chem. Rev.* **2007**, *107*, 926–952.

[101] Delgado, M. C. R.; Kim, E.-G.; Filho, D. t. A. d. S.; Bredas, J.-L. *J. Am. Chem. Soc.* **2010**, *132*, 3375–3387.

[102] Jean-Michel, N. *C. R. Phys.* **2002**, *3*, 523–542.

[103] Peumans, P.; Yakimov, A.; Forrest, S. R. *J. Appl. Phys.* **2003**, *93*, 3693–3723.

[104] Miranda, P. B.; Moses, D.; Heeger, A. J. *Phys. Rev. B* **2001**, *64*, 081201.

[105] Mozer, A. J.; Sariciftci, N. S. *C. R. Phys.* **2006**, *9*, 568–577.

[106] Brédas, J.-L.; Beljonne, D.; Coropceanu, V.; Cornil, J. *Chem. Rev.* **2004**, *104*, 4971–5004.

[107] McCulloch, I.; Heeney, M.; Bailey, C.; Genevicius, K.; MacDonald, I.; Shkunov, M.; Sparrowe, D.; Tierney, S.; Wagner, R.; Zhang, W.; Chabinyc, M. L.; Kline, R. J.; McGehee, M. D.; Toney, M. F. *Nat. Mater.* **2006**, *5*, 328–333.

[108] Liang, Y.; Xu, Z.; Xia, J.; Tsai, S.-T.; Wu, Y.; Li, G.; Ray, C.; Yu, L. *Adv. Mater.* **2010**, *22*, E135–E138.

[109] Chang, C.-Y.; Wu, C.-E.; Chen, S.-Y.; Cui, C.; Cheng, Y.-J.; Hsu, C.-S.; Wang, Y.-L.; Li, Y. *Angew. Chem. Int. Ed.* **2011**, *50*, 9386–9390.

[110] Zhang, W.; Jin, W.; Fukushima, T.; Saeki, A.; Seki, S.; Aida, T. *Science* **2011**, *334*, 340–343.

[111] Duan, X.; Huang, Y.; Cui, Y.; Wang, J.; Lieber, C. M. *Nature* **2001**, *409*, 66–69.

[112] Lu, W.; Xiang, J.; Timko, B. P.; Wu, Y.; Lieber, C. M. *Proc. Natl. Acad. Sci.* **2005**, *102*, 10046–10051.

[113] Tian, B.; Zheng, X.; Kempa, T. J.; Fang, Y.; Yu, N.; Yu, G.; Huang, J.; Lieber, C. M. *Nature* **2007**, *449*, 885–889.

[114] Briseno, A. L.; Holcombe, T. W.; Boukai, A. I.; Garnett, E. C.; Shelton, S. W.; Fréchet, J. J. M.; Yang, P. *Nano. Lett.* **2010**, *10*, 334–340.

[115] Greene, L. E.; Law, M.; Yuhas, B. D.; Yang, P. *J. Phys. Chem. C* **2007**, *111*, 18451–18456.

[116] Cui, Q. H.; Jiang, L.; Zhang, C.; Zhao, Y. S.; Hu, W.; Yao, J. *Adv. Mater.* **2012**, *24*, 2332–2336.

[117] Hurst, S. J.; Payne, E. K.; Qin, L.; Mirkin, C. A. *Angew. Chem. Int. Ed.* **2006**, *45*, 2672–2692.

[118] Wang, H.; Sun, M.; Ding, K.; Hill, M. T.; Ning, C.-Z. *Nano. Lett.* **2011**, *11*, 1646–1650.

[119] Li, X.; Wang, T.; Zhang, J.; Zhu, D.; Zhang, X.; Ning, Y.; Zhang, H.; Yang, B. *ACS Nano* **2010**, *4*, 4350–4360.

[120] Zhang, Y.; Dong, H.; Tang, Q.; Ferdous, S.; Liu, F.; Mannsfeld, S. C. B.; Hu, W.; Briseno, A. L. *J. Am. Chem. Soc.* **2010**, *132*, 11580–11584.

[121] De Greef, T. F. A.; Smulders, M. M. J.; Wolffs, M.; Schenning, A. P. H. J.; Sijbesma, R. P.; Meijer, E. W. *Chem. Rev.* **2009**, *109*, 5687–5754.

[122] Hoeben, F. J. M.; Jonkheijm, P.; Meijer, E. W.; Schenning, A. P. H. J. *Chem. Rev.* **2005**, *105*, 1491–1546.

[123] Yamamoto, Y.; Fukushima, T.; Suna, Y.; Ishii, N.; Saeki, A.; Seki, S.; Tagawa, S.; Taniguchi, M.; Kawai, T.; Aida, T. *Science* **2006**, *314*, 1761–1764.

[124] Yamamoto, Y.; Zhang, G.; Jin, W.; Fukushima, T.; Ishii, N.; Saeki, A.; Seki, S.; Tagawa, S.; Minari, T.; Tsukagoshi, K.; Aida, T. *Proc. Natl. Acad. Sci.* **2009**, *106*, 21051–21056.

[125] Yamamoto, Y.; Fukushima, T.; Saeki, A.; Seki, S.; Tagawa, S.; Ishii, N.; Aida, T. *J. Am. Chem. Soc.* **2007**, *129*, 9276–9277.

[126] He, Y.; Yamamoto, Y.; Jin, W.; Fukushima, T.; Saeki, A.; Seki, S.; Ishii, N.; Aida, T. *Adv. Mater.* **2010**, *22*, 829–832.

[127] Hizume, Y.; Tashiro, K.; Charvet, R.; Yamamoto, Y.; Saeki, A.; Seki, S.; Aida, T. *J. Am. Chem. Soc.* **2010**, *132*, 6628–6629.

[128] Charvet, R.; Yamamoto, Y.; Sasaki, T.; Kim, J.; Kato, K.; Takata, M.; Saeki, A.; Seki, S.; Aida, T. *J. Am. Chem. Soc.* **2012**, *134*, 2524–2527.

[129] Sakai, N.; Bhosale, R.; Emery, D.; Mareda, J.; Matile, S. *J. Am. Chem. Soc.* **2010**, *132*, 6923–6925.

[130] Kishore, R. S. K.; Kel, O.; Banerji, N.; Emery, D.; Bollot, G.; Mareda, J.; Gomez-Casado, A.; Jonkheijm, P.; Huskens, J.; Maroni, P.; Borkovec, M.; Vauthey, E.; Sakai, N.; Matile, S. *J. Am. Chem. Soc.* **2009**, *131*, 11106–11116.

[131] Tu, S.; Kim, S. H.; Joseph, J.; Modarelli, D. A.; Parquette, J. R. *J. Am. Chem. Soc.* **2011**, *133*, 19125–19130.

[132] Mativetsky, J. M.; Kastler, M.; Savage, R. C.; Gentilini, D.; Palma, M.; Pisula, W.; Müllen, K.; Samorì, P. *Adv. Funct. Mater.* **2009**, *19*, 2486–2494.

[133] Treier, M.; Liscio, A.; Mativetsky, J. M.; Kastler, M.; Mullen, K.; Palermo, V.; Samori, P. *Nanoscale* **2012**, *4*, 1677–1681.

[134] Würthner, F.; Chen, Z.; Hoeben, F. J. M.; Osswald, P.; You, C.-C.; Jonkheijm, P.; Herrikhuyzen, J. v.; Schenning, A. P. H. J.; van der Schoot, P. P. A. M.; Meijer, E. W.; Beckers, E. H. A.; Meskers, S. C. J.; Janssen, R. A. J. *J. Am. Chem. Soc.* **2004**, *126*, 10611–10618.

[135] Lambrecht, J.; Saragi, T. P. I.; Onken, K.; Salbeck, J. *ACS Appl. Mater. Interfaces* **2011**, *3*, 1809–1812.

[136] Che, Y.; Yang, X.; Liu, G.; Yu, C.; Ji, H.; Zuo, J.; Zhao, J.; Zang, L. *J. Am. Chem. Soc.* **2010**, *132*, 5743–5750.

[137] Che, Y.; Datar, A.; Yang, X.; Naddo, T.; Zhao, J.; Zang, L. *J. Am. Chem. Soc.* **2007**, *129*, 6354–6355.

[138] Sofos, M.; Goldberger, J.; Stone, D. A.; Allen, J. E.; Ma, Q.; Herman, D. J.; Tsai, W.-W.; Lauhon, L. J.; Stupp, S. I. *Nat. Mater.* **2009**, *8*, 68–75.

[139] Ruiz Delgado, M. C.; Kim, E.-G.; da Silva Filho, D. A.; Bredas, J.-L. *J. Am. Chem. Soc.* **2010**, *132*, 3375–3387.

[140] Messmore, B. W.; Hulvat, J. F.; Sone, E. D.; Stupp, S. I. *J. Am. Chem. Soc.* **2004**, *126*, 14452–14458.

[141] Hizume, Y.; Tashiro, K.; Charvet, R.; Yamamoto, Y.; Saeki, A.; Seki, S.; Aida, T. *J. Am. Chem. Soc.* **2010**, *132*, 6628–6629.

[142] Jiang, L.; Fu, Y.; Li, H.; Hu, W. *J. Am. Chem. Soc.* **2008**, *130*, 3937–3941.

[143] Luo, J.; Yan, Q.; Zhou, Y.; Li, T.; Zhu, N.; Bai, C.; Cao, Y.; Wang, J.; Pei, J.; Zhao, D. *Chem. Commun.* **2010**, *46*, 5725–5727.

[144] Langhals, H.; Ismael, R. *Eur. J. Org. Chem.* **1998**, *1998*, 1915–1917.

[145] Zang, L.; Liu, R.; Holman, M. W.; Nguyen, K. T.; Adams, D. M. *J. Am. Chem. Soc.* **2002**, *124*, 10640–10641.

[146] Eaton, S. W.; Shoer, L. E.; Karlen, S. D.; Dyar, S. M.; Margulies, E. A.; Veldkamp, B. S.; Ramanan, C.; Hartzler, D. A.; Savikhin, S.; Marks, T. J.; Wasielewski, M. R. *J. Am. Chem. Soc.* **2013**, *135*, 14701–14712.

[147] Che, Y.; Yang, X.; Zhang, Z.; Zuo, J.; Moore, J. S.; Zang, L. *Chem. Commun.* **2010**, *46*, 4127–4129.

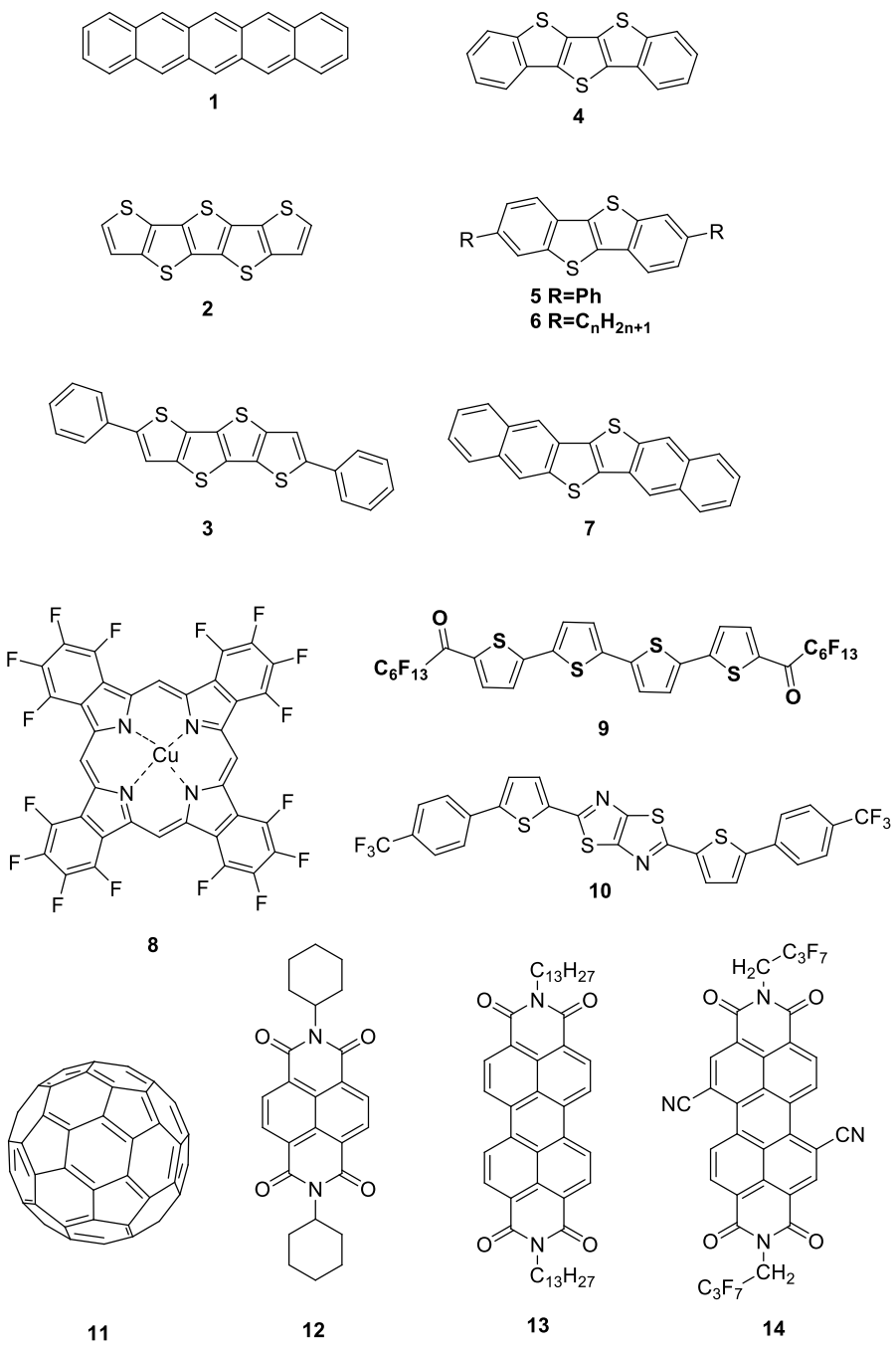

Figure 1.1 The molecular structures of p-type (**1** to **7**) and n-type (**8** to **14**) materials.

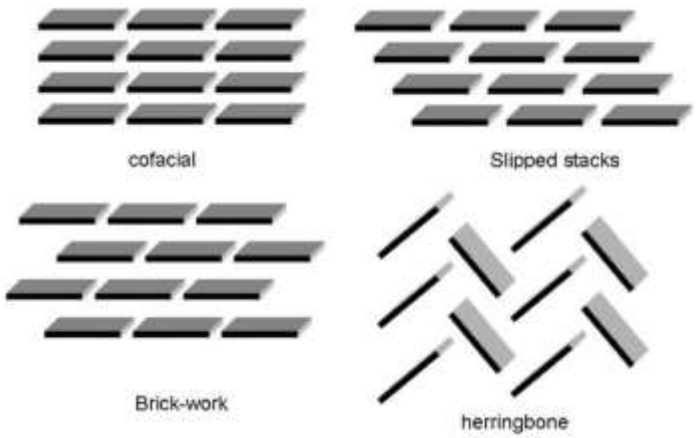

Figure 1.2 Some possible packing patterns for organic molecules (adapted from [40]).

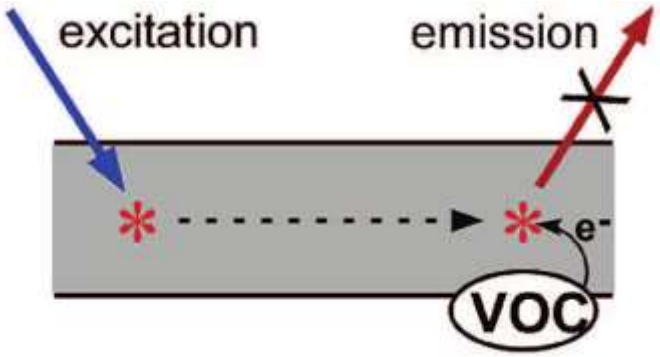

Figure 1.3 Amplified fluorescence quenching mechanism (adapted from [59]).

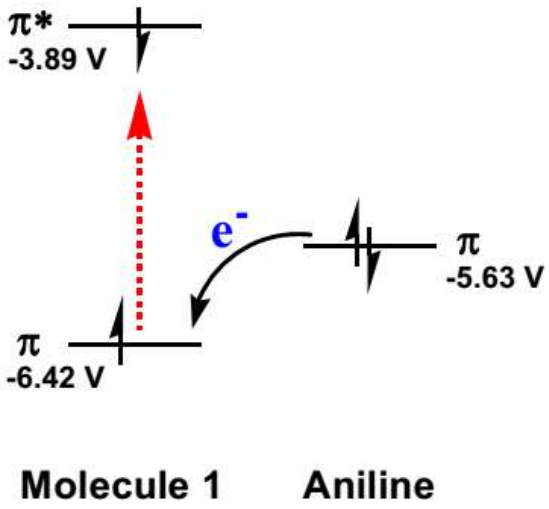

Figure 1.4 Photoinduced electron transfer process (adapted from [85]).

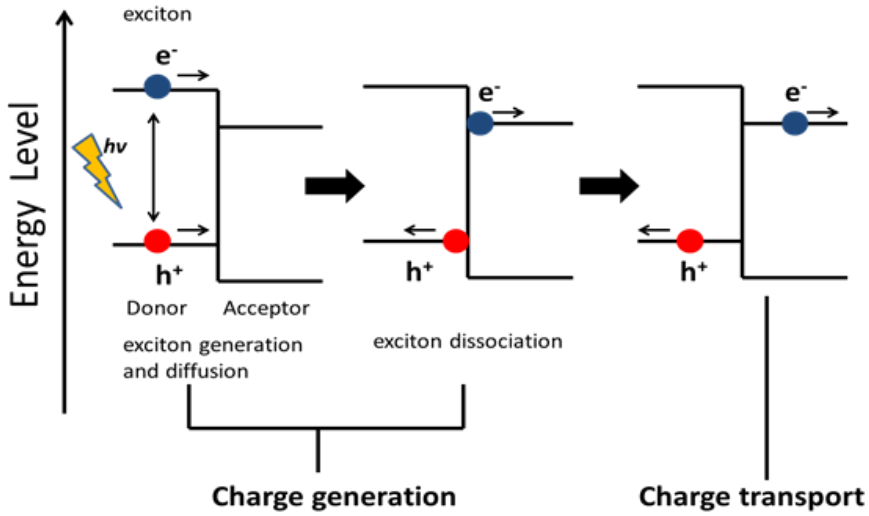

Figure 1.5 The charge generation and transport processes in organic solar cell.

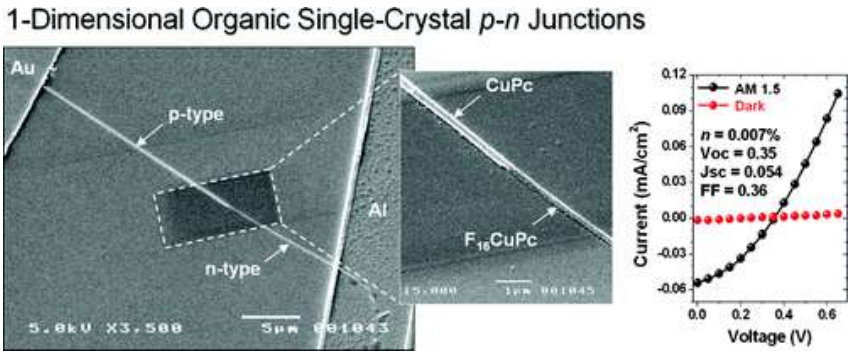

Figure 1.6 Copper phthalocyanine (CuPc) and copper hexadecafluorophthalocyanine (F16CuPc) based nanofibril heterojunction (adapted from [120]).

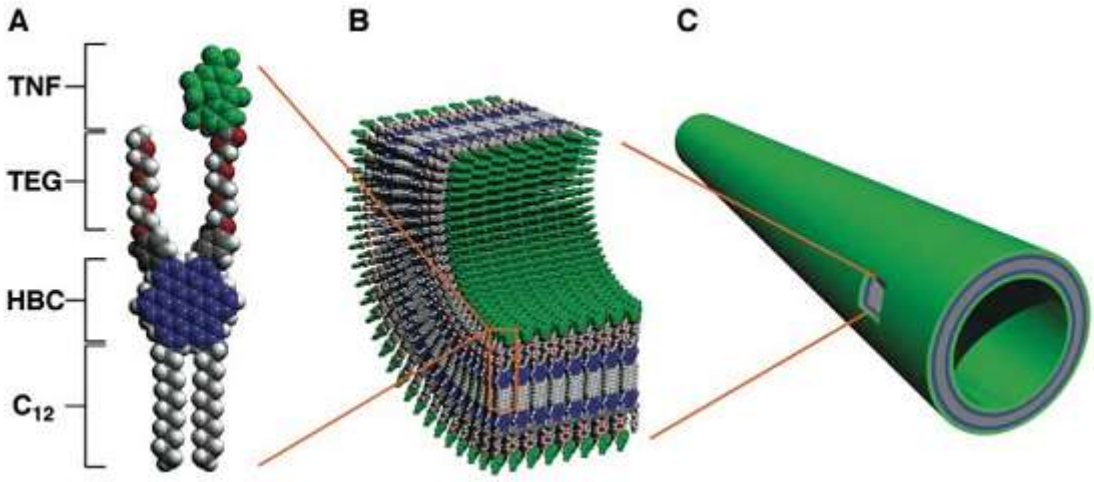

Figure 1.7 HBC based one-dimensional heterojunction nanotube (adapted from [123]).

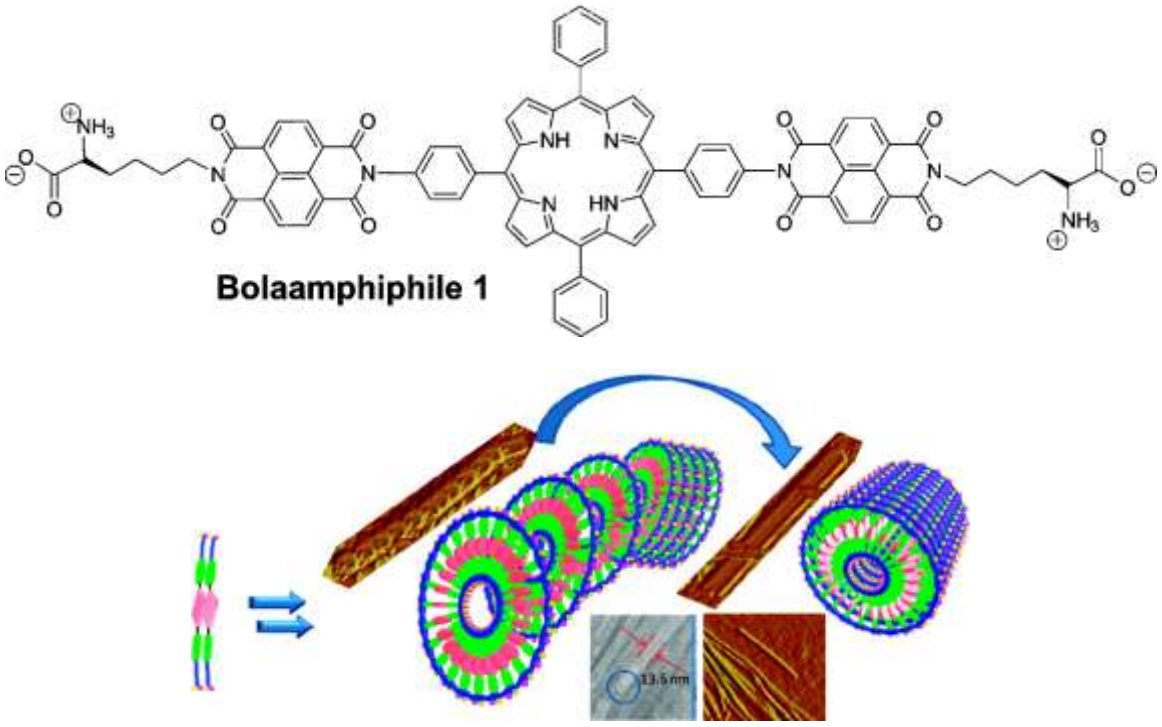

Figure 1.8 Tetraphenylporphyrin (TPP) and NDI based nanofibril heterojunction (adapted from [131]).

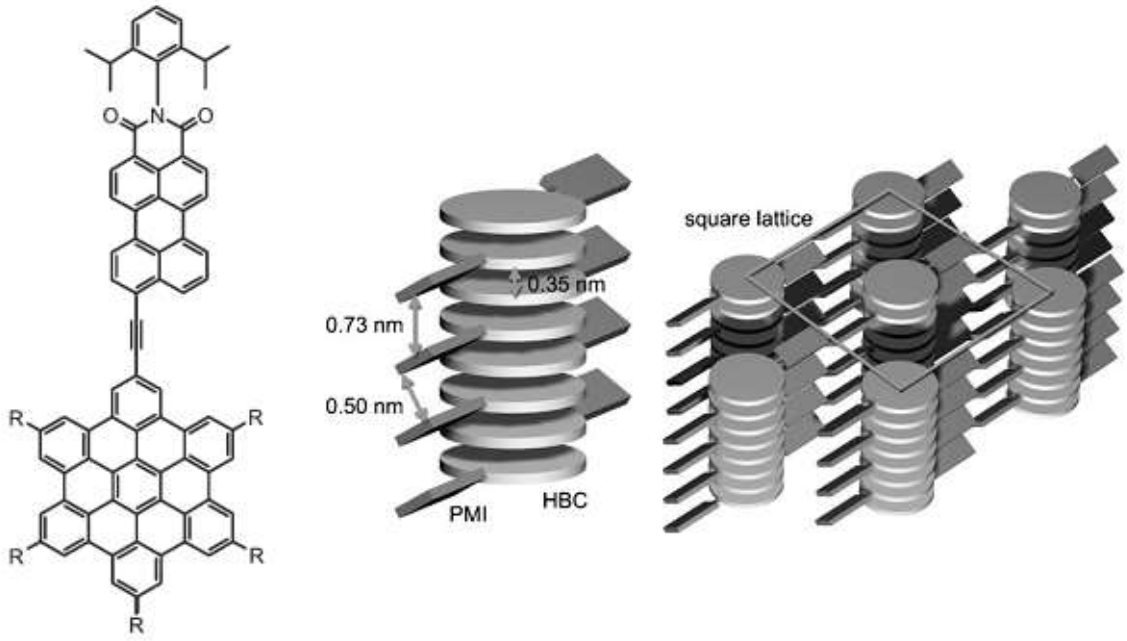

Figure 1.9 HBC part and perylene monoimide (PMI) based nanofibril heterojunction (adapted from [132]).

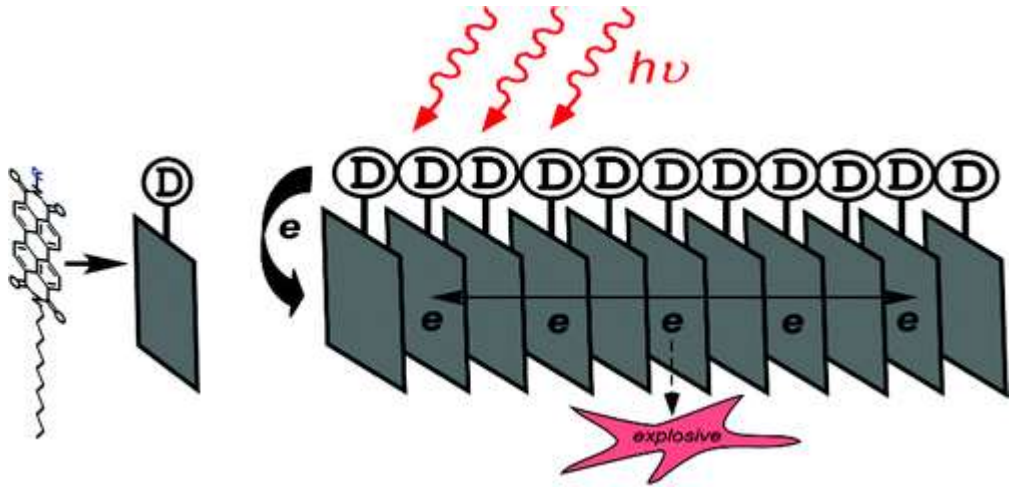

Figure 1.10 Amphiphilic electron donor-PTCDI nanofiber (adapted from [136]).

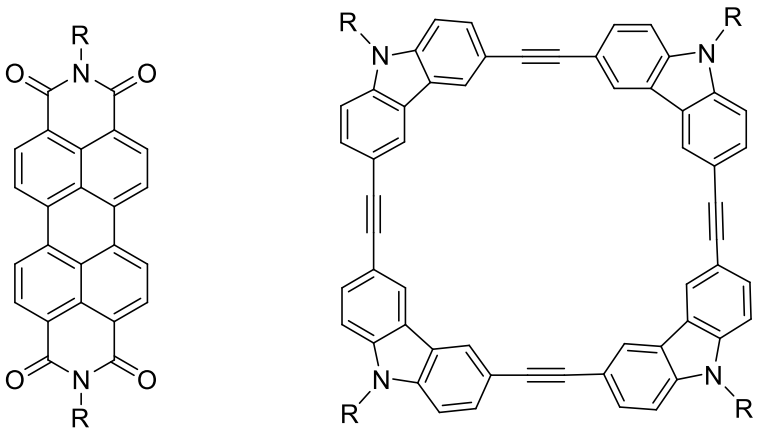

PTCDI AEM

Figure 1.11 The molecular structures of PTCDI and AEMs.

Table 1.1 The summary of energy levels and mobility of organic semiconductor materials.

p-type materials					*n*-type materials				
Molecule	LUMO (eV)	HOMO (eV)	Band gap (eV)	Mobility ($cm^2V^{-1}s^{-1}$)	Molecule	LUMO (eV)	HOMO (eV)	Band gap (eV)	Mobility ($cm^2V^{-1}s^{-1}$)
1	-2.9	-5	2.1	5	**8**	-4.8	-6.3	1.5	0.03
2	-2.04	-5.33	3.29	0.045	**9**	-3.96	-6.36	2.4	1.7
3	-2.82	-5.43	2.61	0.14	**10**	-2.9	-5.61	2.71	1.2
4	-2.14	-5.6	3.46	0.51	**11**	-4	-6.2	2.2	12
5	-2.4	-5.6	3.2	2	**12**	-4.01	-7.07	3.06	6
6	-2	-5.5	3.5	2.75	**13**	-3.69	-5.82	2.13	2.1
7	-1.81	-5.19	3.38	2.9	**14**	-4.5	-6.8	2.3	1.3

CHAPTER 2

INTERFACIAL ENGINEERING OF ORGANIC NANOFIBRIL HETEROJUNCTIONS INTO HIGHLY PHOTOCONDUCTIVE MATERIALS

2.1 Abstract

Photoconductive organic materials have gained increasing interest in various optoelectronics, such as sensors, photodetectors, and photovoltaics. However, the availability of such materials is very limited due to their intrinsic low charge carrier density and mobility. Here, we present a simple approach based on nanofibril heterojunction to achieve high photoconductivity with fast photoresponse (i.e., interfacial engineering of electron donor (**D**) coating onto acceptor (**A**) nanofibers via optimization of hydrophobic interaction between long alkyl side-chains). Such nanofibril heterojunctions possess two prominent features that are critical for efficient photocurrent generation: the nanofibers both create large **D/A** interface for increased charge separation and act as long-range transport pathways for photogenerated charge carriers towards the electrodes, and the alkyl groups employed not only enable effective surface adsorption of **D** molecules on the nanofibers for effective electron-transfer communication, but also spatially separate the photogenerated charge carriers to prevent their recombination. The reported approach represents a simple, adaptable method that allows for the development and optimization of photoconductive organic materials.

2.2 Introduction

Photoconductive organic materials have attracted increasing interest due to their potential applications in photodetectors [1–4], sensors [5–7], and photovoltaics [8–10]. However, the available organic materials are very limited due to their intrinsic low charge carrier density and mobility. Although bulk heterojunctions of electron donors (**D**) and acceptors (**A**) allow for generation of photocurrent, the formation of charge-transfer complex and the lack of long-range charge transport pathway result in loss of the photogenerated charge carriers through recombination [3, 11]. One-dimensional organic nanostructures assembled via π-π interactions present promising candidates for highly photoconductive materials due to their enhanced charge carrier mobility [12–16]. However, only a few examples of photoconductive one-dimensional nanostructures have been reported [3, 8, 17–20], and most of them are focused on the covalently linked **D-A** molecules [3, 8, 17, 18]. Obvious disadvantages of these systems include complicated molecular design and synthesis and challenges in optimization of the intermolecular assembly so as to avoid charge carrier recombination, making them impractical in large-scale applications. Therefore, it is highly demanded to develop simple and general methods to fabricate photoconductive organic materials.

Here, we present a simple approach based on nanofibril heterojunctions (Figure 2.1) to achieve high photoconductivity and fast photoresponse with a large on/off ratio above 10^4 for organic semiconductor materials (i.e., interfacial engineering of **D** molecule coating onto **A** nanofibers via optimization of the hydrophobic interaction between long alkyl side-chains). We find that the hydrophobic interaction between alkyl side-chains enables effective adsorption of **D** molecules onto **A** nanofibers, for which the surface binding of **D**

can be further strengthened by increasing the numbers of alkyl chains in **D** molecules. The resulting interface via alkyl interdigitattion was demonstrated to be capable of tuning both the photoinduced electron transfer from **D** to **A** and the charge recombination, thus providing optimization of the photoconductive performance of the nanofibril heterojunctions thus fabricated. We anticipate that this simple approach to fabrication of highly photoconductive organic materials will lead to more options for the new materials design and performance improvement and optimization.

2.3 Results and discussion

2.3.1 Fabrication of nanofibril heterojunctions

Figure 2.2 shows the nanofibers assembled from **A-1** molecules (Figure 2.1) using a previously reported method [21, 22]. These nanofibers are several microns long and tens of nanometers wide. Such thin nanofibers possess a large surface area allowing for surface adsorption of **D** molecules to produce wide **D**/**A** interface, which in turn leads to efficient dissociation of excitons into separated charge carriers through interfacial electron transfer as illustrated in Figure 2.1. Because the strong π-π stacking interaction between the **A** molecules (the perylene planes) results in effective π-electron delocalization (i.e., enhanced electron migration along the long axis of nanofiber [5, 11–13]), the separated charge carriers can be collected at two electrodes upon application of an electrical bias.

With the nanofiber as an efficient charge conduit, the next critical criterion for achieving high photocurrent with the fibril heterojunctions is to prevent the back electron transfer (i.e., the charge recombination between the photogenerated electron and hole), which indeed represents one of the major causes for charge loss in bulk heterojunction

materials (e.g., C60/polymers [10]). To this end, we designed and synthesized **D-1** molecule (Figure 2.1), which possesses three long alkyl chains and is expected to strongly bind to the surface of nanofibers that are self-assembled from the **A** molecules (e.g., **A-1**) with similar linear alkyl side-chains. Meanwhile, the space separation caused by the interdigitated alkyl chains would inhibit the charge recombination between the photogenerated anionic and cationic radicals. The nanofibril heterojunctions were fabricated simply by drop-casting an ethanol solution of **D-1** onto the **A-1** nanofibers deposited on silica substrate. Interestingly, as evidenced by SEM and AFM images (Figure 2.2), most **D-1** molecules were bound to the nanofibers upon vaporization of the solvent, and no apparent **D-1** materials similar to the film morphology formed by direct drop-casting of the ethanol solution of **D-1** onto the same substrate (Figure 2.3) were observed between the nanofibers. A close examination of AFM images clearly shows **D-1** molecules were mostly adsorbed on the surface of **A-1** nanofibers (Figure 2.2). The spontaneous adsorption and concentration of **D-1** molecules onto **A-1** nanofibers is likely driven by the hydrophobic interaction between the alkyl side-chains as mentioned above. In comparison, the highly hydrophilic surface of silica is not favored for strong binding with the **D-1** molecules. Indeed, drop-casting of the same **D-1** solution onto silica led to formation of broken films consisting of thin flakes and particulate aggregates (Figure 2.3), mainly caused by the surface dewetting. The observed one-step coating of **D** over **A** nanostructured materials provides a simple, clean method for construction of large area **D**/**A** heterojunctions with a wide interface.

Apparently, the nanofibril heterojunctions thus fabricated prevent the formation of charge-transfer complex of **D-A** as the **A-1** nanofibers were pre-assembled without the

interference of **D** molecules, and the fibril materials are robust against the drop-casting solvent (i.e., **A-1** molecules are insoluble in ethanol). In contrast, formation of **D-A** charge-transfer complex is usually difficult to avoid in bulk heterojunction materials [23–25], where the intracomplex charge recombination dominates the loss of charge carriers. The nanofibril heterojunction system as presented in Figure 2.1 also demonstrates practical advantages in comparison to the materials fabricated from covalently linked **D-A** molecules, which often require a much more complicated molecular design and synthesis and thus offer limited choices for the structural optimization of **D** and **A** molecules.

2.3.2 Photoconductivity of the nanofibril heterojunctions

As shown in Figure 2.4, high photoconductivity was observed for the nanofibril heterojunctions as presented in Figure 2.2, whereas negligible photocurrent was measured for the pristine **A-1** nanofibers or pure **D-1** film (Figure 2.5). The photocurrent also increased with the amount of **D-1** added at the initial stage until a saturated region is reached at a molecular molar ratio of **A-1** to **D-1** of about 2. At this molar composition, the nanofibril heterojunction demonstrated a photocurrent on/off ratio above 10^4 when measured on a micro-electrode pair (90 μm wide and 5 μm gap) under a bias of 10 V (Figure 2.6). Given that the average irradiation light is 550 nm, the quantum efficiency of the photocurrent generation can be estimated as ca. 8% under an electrical field of 2 V/μm by using the same calculation method as previously reported [26, 27]. The photocurrent was found also switching promptly with light on and off (Figure 2.7), indicating a response time of only 200 ms (Figure 2.8). The fast photoresponse as observed, together with the high on/off ratio, makes the nanofibril heterojunctions attractive for application in

optoelectronic devices.

Consistent with the high photocurrent generation, the fluorescence of A-1 nanofibers was also found to be effectively quenched upon adsorption of D-1 molecules (Figure 2.4). Since the absorption edge of D-1 is far below 400 nm, the observed fluorescence quenching of nanofibers is unlikely due to energy transfer, but rather solely to the interfacial electron transfer from D to the photoexcited A as illustrated in Figure 2.1. Such photoinduced electron transfer is highly favored with a driving force of 0.95 eV (Figure 2.9). As such, fluorescence quenching in such a system denotes the forward electron transfer from D to A-1 nanofibers upon irradiation. Interestingly, ca. 13% molar fraction of **D-1** quenched ca. 55% of the fluorescence of **A-1** nanofibers. This amplified fluorescence quenching implies the existence of exciton diffusion within **A-1** nanofibers, as previously indicated in other nanostructured systems [28]. Since the nanofibril heterojunctions are formed by the adsorption of **D-1** molecules via the hydrophobic interaction between alkyl groups, it is expected that the adsorption and de-adsorption of **D-1** can be readily switched, making the photoconductivity reversible. Indeed, the reversible photoconductivity was achieved simply by washing away the **D-1** molecules with ethanol and redeposition of its ethanol solution onto the nanofibers (Figure 2.10). Thinking to the potential degeneration of the photoconductivity of organic materials caused by the photooxidation, the easy regeneration of photoconductivity is attractive for practical applications.

2.3.3 Interfacial influence on the photoconductivity

Although efficient photoinduced electron transfer was previously observed for the perylene diimide-based supramolecular **D**/**A** systems [29–31], no significant

photoconductivity has yet been achieved with these materials. To gain an insight into the origin of the high photoconductivity as achieved in Figure 2.4, we investigated various **D** and **A** molecules bearing different side groups (Figure 2.1), which formulate the heterojunction interface and affect greatly the **D/A** interaction. As shown in Figure 2.7, all three **D** molecules demonstrated efficient fluorescence quenching of the **A-1** nanofibers when coated onto the surface, indicating the occurrence of photoinduced electron transfer from **D** to **A** upon photo-illumination. However, significant photocurrent was only obtained with **D-1** and **D-2** molecules bearing long alkyl groups, whereas **D-3** generated negligible current under the same conditions. This result implies that introduction of alkyl groups can effectively prevent the recombination of photogenerated charge carriers through spatial separation. Such spatial effect on the prevention of charge carrier recombination is analogous to that observed in the one-dimensional nanostructures composed of covalently linked **D-A** molecules [3, 17]. Here, it can be speculated that the spatial segregation can be optimized towards the photocurrent generation by altering the length of alkyl chains, and the work along this line is under progress.

Compared to **D-2**, **D-1** exhibited about six times higher photocurrent despite 15 times molar excess of **D-2** being used. This observation can be interpreted by the fact that the three alkyl chains borne with **D-1** make its binding to the nanofibers much stronger to allow electron-transfer communication more efficiently. The stronger interfacial binding is indeed supported by the higher fluorescence quenching efficiency as observed for even less **D-1** used (Figure 2.7). To further study the influence of side groups on the interfacial **D/A** interaction, we fabricated nanofibers from **A-2** molecules, which possess the same π-scaffold as **A-1**, but bear short, more hydrophilic side-chains, which are not compatible

with **D-1** bearing the hydrophobic side-chains. This should result in a separated interface between the **D-1** phase and **A-2** fibers, which thus inhibits the electron-transfer communication at **D/A** interface. Indeed, the heterojunction system fabricated from **A-2** fibers and **D-1** molecules exhibited neither fluorescence quenching nor photocurrent generation (Figure 2.7). This negative observation further supports the importance of alkyl groups to photocurrent generation.

To verify the critical effect of one-dimensional π-π stacking as envisioned in the nanofibril structure on the photocurrent generation, we investigated another heterojunction system fabricated by adsorption of **D** molecules on the film of **A-3**. Due to the steric hindrance of the branched side groups of **A-3**, it is impossible to fabricate highly organized materials from this molecule, particularly with π-π stacking along one dimension [21]. Although efficient electron transfer can take place at the **D/A** interface upon irradiation, as evidenced by the significant fluorescence quenching of the film upon coating with **D-3** and **D-1** (Figure 2.7), negligible photocurrent was observed for these film-based heterojunctions, likely owing to the lack of effective charge transport pathways within the film. This result indicates that the **A-1** nanofibers as employed indeed play a critical role enabling rapid transport of the charge carriers towards the electrodes.

2.4 Conclusion

In summary, highly photoconductive organic nanofibril heterojunctions have been fabricated through simple interfacial engineering of the hydrophobic interaction between alkyl side-chains. Such nanofibril heterojunctions possess two prominent features that are critical for efficient photocurrent generation: one is that the nanofibers both create a wide

D/A interface for increased charge separation and act as a long-range transport pathway for photogenerated charge carriers towards the electrodes; the other is that the alkyl groups employed not only enable effective surface adsorption of **D** molecules on the nanofibers for effective electron-transfer communication, but also spatially separate the photogenerated charge carriers to prevent their recombination. The reported approach represents a simple, adaptable method allowing for development and optimization of photoconductive supramolecular organic materials.

2.5 Experimental section

2.5.1 Molecular synthesis

Molecules **A-1, A-2, A-3** were synthesized following the previous methods developed in ours and others labs [32, 33]. **D-1** and **D-2** were synthesized as follows (Figure 2.11).

Intermediate compound **3** was synthesized following the protocol as previously reported [34]. 2,7-dibromo-9-octyl-9H-carbazole **2** (220 mg, 0.5 mmol), 9H-carbazole-2-boronic acid pinacol ester **1** (880 mg, 1.5 mmol), and benzyltriethylammonium chloride (50 mg) were added into a mixture of toluene (20 mL) and aqueous K_2CO_3 (2 M, 8 mL), followed by three freeze-pump-thaw cycles of degassing. $Pd(PPh_3)_4$ (5 mg) was then added under argon protection, again followed by three freeze-pump-thaw cycles of degassing. The mixture was refluxed for 24 h and the organic phase was separated and evaporated. The product was purified by column chromatography on silica gel (hexane/THF, 4:2) and dried in vacuum. A 220 mg (71%) yield of compound **3** was obtained as a light brown powder. ^{1}H NMR (THF-*d*8, 500 MHz): δ = 10.33 (s, 2 H), 8.15 (m, 4 H), 8.07 (d, *J* = 7.9, 2 H), 7.82 (m, 4 H), 7.6 (m, 4 H), 7.43 (d, *J* = 8.0, 2 H), 7.34 (m, 2 H), 7.15 (m, 2 H), 4.56

(t, *J* = 7.19, 2 H), 1.99 (m, 2 H), 1.29 (m, 10 H), 0.83 (t, *J* = 6.9, 3 H). MALDI-TOF MS: *m*/*z* 609.33 (100%).

Synthesis of **D-1**: Compound **3** (0.01 mmol) was dissolved in 15 ml of THF, followed by addition of the phase transfer catalyst benzyltriethylammonium chloride (50 mg), $C_9H_{19}Br$ (0.1 ml), and KOH (6 mg, 0.1 mmol). The mixture was then stirred and refluxed for 2 h. The reaction mixture was poured into water and extracted by chloroform. The organic phase was collected, washed with brine and water and dried. The raw product thus obtained was further purified by column chromatography on silica gel (hexane/CH_2Cl_2, 100:1) and dried in vacuum. A 5.4 mg (63%) yield of compound **D-1** was obtained as white powder. ^{1}HNMR ($CDCl_3$, 500 MHz): δ = 8.17 (m, 4 H), 8.12 (d, *J* = 7.5, 2 H), 7.71 (m, 4 H), 7.61 (m, 4 H), 7.43 (d, *J* = 8.0, 2 H), 7.42 (m, 2 H), 7.24 (m, 2 H), 4.11 (t, *J* = 6.9, 6 H), 1.65 (m, 6 H), 1.26–1.41 (m, 34 H), 0.87 (t, *J* = 6.9, 9 H). MALDI-TOF MS: *m*/*z* 861.60 (100%).

Synthesis of **D-2**: A mixture of 9H-Carbazole **4** (1.67 g, 10 mmol), KOH (0.84 g, 15 mmol), 1-Bromooctane (2.88 g, 15 mmol), and a small amount of KI (5%) in dry THF (100 mL) was stirred at 65 °C under argon atmosphere for 24 h. After cooling to room temperature, the reaction mixture was poured into water and the product was extracted with chloroform. The solvent was evaporated under reduced pressure, and the crude product was purified by column chromatography on silica gel (hexane as the fluent) to give a yellow oil product N-Octylcarbazole **D-2** (1.95 g, 70%). ^{1}H NMR (CDCl3, 500 MHz): δ = 8.09 (dd, *J* = 8.0 Hz, 2 H), 7.44 (ddd, *J* = 6.5, 6.2 Hz, 2 H), 7.39 (dd, *J* = 8.0 Hz, 2 H), 7.22 (ddd, *J* = 7.0 Hz, 2 H), 4.28 (t, *J* = 7.5 Hz, 2 H), 1.86 (tt, *J* = 7.5 Hz, 2 H), 1.24–1.40 (m, 10 H), 0.86 (t, *J* = 7.0 Hz, 3 H).

2.5.2 Fabrication of A-1 nanofibers and the nanofibril heterojunctions

A-1 nanofibers were fabricated by injecting 0.5 mL chloroform solution of **A-1** molecules (0.15 mM) into 3 mL ethanol in a test tube followed by 5 hours aging. The nanofibers thus formed can be transferred and cast onto the glass surface by pipetting. The nanofibril heterojunctions were fabricated by directly drop-casting the ethanol solution of **D** molecules onto the nanofibers predeposited on the silica substrate. The concentrations of ethanol solution as employed for **D-1**, **D-2**, and **D-3** were 0.1, 1, and 1 mM, respectively. The **A-2** nanofibers were fabricated in a similar way. The **A-3** film was fabricated by drop-casting a chloroform solution of **A-3** (20 nM) on the substrate.

2.5.3 Property characterization of nanofibers

Fluorescence spectra of **A-1** nanofibers and **A-3** film were measured on a LS 55 fluorometer. The fluorescence spectra of **A-2** fibers (with too low fluorescence quantum yield to be measured by ordinary fluorometer) were measured with a Leica DMI4000B inverted microscope (which provides excitation in the range of 530–560 nm) coupled with an Acton SP-2356 Imaging Spectrograph system and Acton PIXIS 400B Digital CCD Camera System for full spectra recording. SEM measurement was performed with a FEI NanoNova 6300 microscope, and the samples were directly drop-casting on a silica substrate. No metallic coating was needed for this field-emitting mode SEM, helping precisely reveal the morphology and size change of nanofibers upon coating D materials. AFM measurement was performed in tapping mode on a Veeco MultiMode V scanning probe microscope.

2.5.4 Electrical measurement with nanofibers

Electrical current measurements of the nanofibers were carried out using a two-probe method on a Signatone S-1160 Probe Station combined with an Agilent 4156C Precision Semiconductor Parameter Analyzer for high resolution current measurement. The probe station was equipped with a Motic Microscope for poisoning and a CCD camera for in situ imaging of the device. The whole measurement system was housed in a shielding dark box to eliminate the RF noise and/or scattering light for low current and/or light sensitive measurements. The microgap electrodes were fabricated by photolithography on a silicon wafer covered with a 300-nm thick SiO_2 dielectric layer. The gold electrode pair used here was 14 or 90 μm in width and 5 μm in gap and fully covered with nanofibers via drop-casting. A tungsten lamp (Quartzline, 21 V, 150 W) was used as the white light source for photocurrent generation, and the light was guided into the probe station through a glass optical fiber, followed by focusing on the sample through the objective lens. The light power reaching the sample surface was measured by a photon detector.

2.6 References

[1] Gong, X.; Tong, M.; Xia, Y.; Cai, W.; Moon, J. S.; Cao, Y.; Yu, G.; Shieh, C.-L.; Nilsson, B.; Heeger, A. J. *Science* **2009**, *325*, 1665–1667.

[2] Konstantatos, G.; Sargent, E. H. *Nat. Nanotechnol.* **2010**, *5*, 391–400.

[3] Yamamoto, Y.; Fukushima, T.; Suna, Y.; Ishii, N.; Saeki, A.; Seki, S.; Tagawa, S.; Taniguchi, M.; Kawai, T.; Aida, T. *Science* **2006**, *314*, 1761–1764.

[4] Zhu, H.; Li, T.; Zhang, Y.; Dong, H.; Song, J.; Zhao, H.; Wei, Z.; Xu, W.; Hu, W.; Bo, Z. *Adv. Mater.* **2010**, *22*, 1645–1648.

[5] Che, Y.; Yang, X.; Liu, G.; Yu, C.; Ji, H.; Zuo, J.; Zhao, J.; Zang, L. *J. Am. Chem. Soc.* **2010**, *132*, 5743–5750.

[6] Che, Y.; Yang, X.; Zhang, Z.; Zuo, J.; Moore, J. S.; Zang, L. *Chem. Commun.* **2010**, *46*, 4127–4129.

[7] Zhang, X.; Jie, J.; Zhang, W.; Zhang, C.; Luo, L.; He, Z.; Zhang, X.; Zhang, W.; Lee, C.; Lee, S. *Adv. Mater.* **2008**, *20*, 2427–2432.

[8] Yamamoto, Y.; Zhang, G.; Jin, W.; Fukushima, T.; Ishii, N.; Saeki, A.; Seki, S.; Tagawa, S.; Minari, T.; Tsukagoshi, K.; Aida, T. *Proc. Natl. Acad. Sci.* **2009**, *106*, 21051–21056.

[9] Charvet, R.; Acharya, S.; Hill, J. P.; Akada, M.; Liao, M.; Seki, S.; Honsho, Y.; Saeki, A.; Ariga, K. *J. Am. Chem. Soc.* **2009**, *131*, 18030–18031.

[10] Clarke, T. M.; Durrant, J. R. *Chem. Rev.* **2010**, *110*, 6736–6767.

[11] Neuteboom, E. E.; Meskers, S. C. J.; van Hal, P. A.; van Duren, J. K. J.; Meijer, E. W.; Janssen, R. A. J.; Dupin, H.; Pourtois, G.; Cornil, J.; Lazzaroni, R.; Brédas, J.-L.; Beljonne, D. *J. Am. Chem. Soc.* **2003**, *125*, 8625–8638.

[12] Coropceanu, V.; Cornil, J.; da Silva Filho, D. A.; Olivier, Y.; Silbey, R.; Brédas, J.-L. *Chem. Rev.* **2007**, *107*, 926–952.

[13] Che, Y.; Datar, A.; Yang, X.; Naddo, T.; Zhao, J.; Zang, L. *J. Am. Chem. Soc.* **2007**, *129*, 6354–6355.

[14] Sofos, M.; Goldberger, J.; Stone, D. A.; Allen, J. E.; Ma, Q.; Herman, D. J.; Tsai, W.-W.; Lauhon, L. J.; Stupp, S. I. *Nat. Mater.* **2009**, *8*, 68–75.

[15] Ruiz Delgado, M. C.; Kim, E.-G.; da Silva Filho, D. A.; Bredas, J.-L. *J. Am. Chem. Soc.* **2010**, *132*, 3375–3387.

[16] Messmore, B. W.; Hulvat, J. F.; Sone, E. D.; Stupp, S. I. *J. Am. Chem. Soc.* **2004**, *126*, 14452–14458.

[17] Che, Y.; Yang, X.; Liu, G.; Yu, C.; Ji, H.; Zuo, J.; Zhao, J.; Zang, L. *J. Am. Chem. Soc.* **2010**, *132*, 5743–5750.

[18] Hizume, Y.; Tashiro, K.; Charvet, R.; Yamamoto, Y.; Saeki, A.; Seki, S.; Aida, T. *J. Am. Chem. Soc.* **2010**, *132*, 6628–6629.

[19] Jiang, L.; Fu, Y.; Li, H.; Hu, W. *J. Am. Chem. Soc.* **2008**, *130*, 3937–3941.

[20] Luo, J.; Yan, Q.; Zhou, Y.; Li, T.; Zhu, N.; Bai, C.; Cao, Y.; Wang, J.; Pei, J.; Zhao, D. *Chem. Commun.* **2010**, *46*, 5725–5727.

[21] Balakrishnan, K.; Datar, A.; Naddo, T.; Huang, J.; Oitker, R.; Yen, M.; Zhao, J.; Zang, L. *J. Am. Chem. Soc.* **2006**, *128*, 7390–7398.

[22] Zang, L.; Che, Y.; Moore, J. S. *Acc. Chem. Res.* **2008**, *41*, 1596–1608.

[23] Neuteboom, E. E.; Meskers, S. C. J.; Van Hal, P. A.; Van Duren, J. K. J.; Meijer, E. W.; Janssen, R. A. J.; Dupin, H.; Pourtois, G.; Cornil, J.; Lazzaroni, R.; Bredas, J.-L.; Beljonne, D. *J. Am. Chem. Soc.* **2003**, *125*, 8625–8638.

[24] Pisula, W.; Kastler, M.; Wasserfallen, D.; Robertson Joseph, W. F.; Nolde, F.; Kohl, C.; Mullen, K. *Angew. Chem. Int. Ed.* **2006**, *45*, 819–823.

[25] Percec, V.; Glodde, M.; Bera, T. k.; Miura, Y.; Shiyanovsaya, I.; Singer, K. D.; Balagurusamy, V. S. K.; Helney, P. A.; Schnell, I.; Rapp, A.; Spiess, H. W.; Hudson, S. D.; Duan, H. *Nature* **2002**, *417*, 384–387.

[26] Schwab, A. D.; Smith, D. E.; Bond-Watts, B.; Johnston, D. E.; Hone, J.; Johnson, A. T.; dePaula, J. C.; Smith, W. F. *Nano Lett.* **2004**, *4*, 1261–1265.

[27] O'Brien, G. A.; Quinn, A. J.; Tanner, D. A.; Redmond, G. *Adv. Mater.* **2006**, *18*, 2379–2383.

[28] Yamamoto, Y.; Fukushima, T.; Saeki, A.; Seki, S.; Tagawa, S.; Ishii, N.; Aida, T. *J. Am. Chem. Soc.* **2007**, *129*, 9276–9277.

[29] Wurthner, F.; Chen, Z.; Hoeben, F. J. M.; Osswald, P.; You, C. C.; Jonkheijm, P.; Herrikhuyzen, J. v.; Schenning, A. P. H. J.; vanderSchoot, P. P. A. M.; Meijer, E. W.; Beckers, E. H. A.; Meskers, S. C. J.; Janssen, R. A. J. *J. Am. Chem. Soc.* **2004**, *126*, 10611–10618.

[30] Van Herrikhuyzen, J.; Syamakumari, A.; Schenning, A. P. H. J.; Meijer, E. W. *J. Am. Chem. Soc.* **2004**, *126*, 10021–10027.

[31] Beckers Edwin, H. A.; Meskers Stefan, C. J.; Schenning Albertus, P. H. J.; Chen, Z.; Wurthner, F.; Marsal, P.; Beljonne, D.; Cornil, J.; Janssen Rene, A. J. *J. Am. Chem. Soc.* **2006**, *128*, 649–657.

[32] Zang, L.; Che, Y.; Moore, J. S. *Acc. Chem. Res.* **2008**, *41*, 1596–1608.

[33] Langhals, H. *Heterocycles* **1995**, *40*, 477–500.

[34] Zhang, C.; Che, Y.; Yang, X.; Bunes, B. R.; Zang, L. *Chem. Commun.* , *46*, 5560–5562.

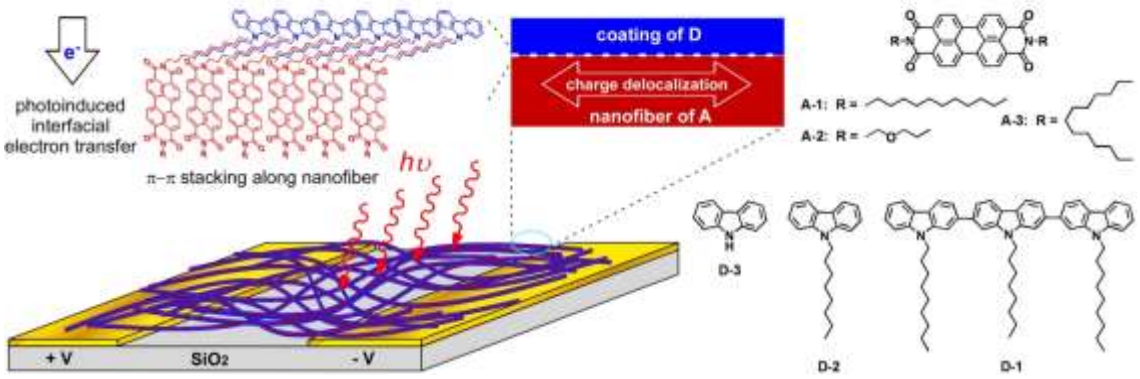

Figure 2.1 Schematic illustration of nanofibril heterojunctions composed of electron donor (D) coated nanofibers that function as electron acceptor (A). The π-stacking along the long axis of the nanofiber is conducive to enhancement of charge transport due to the intermolecular π-electron delocalization. The photoinduced electron transfer in this case is more of an interfacial process, where the interdigitated alkyl chains can inhibit the back electron transfer to a certain extent depending on the length of the alkyl chains. Molecular structures of the three electron acceptors (**A-1**, **A-2**, **A-3)** and three electron donors (**D-1**, **D-2**, **D-3**) are shown in the right panel.

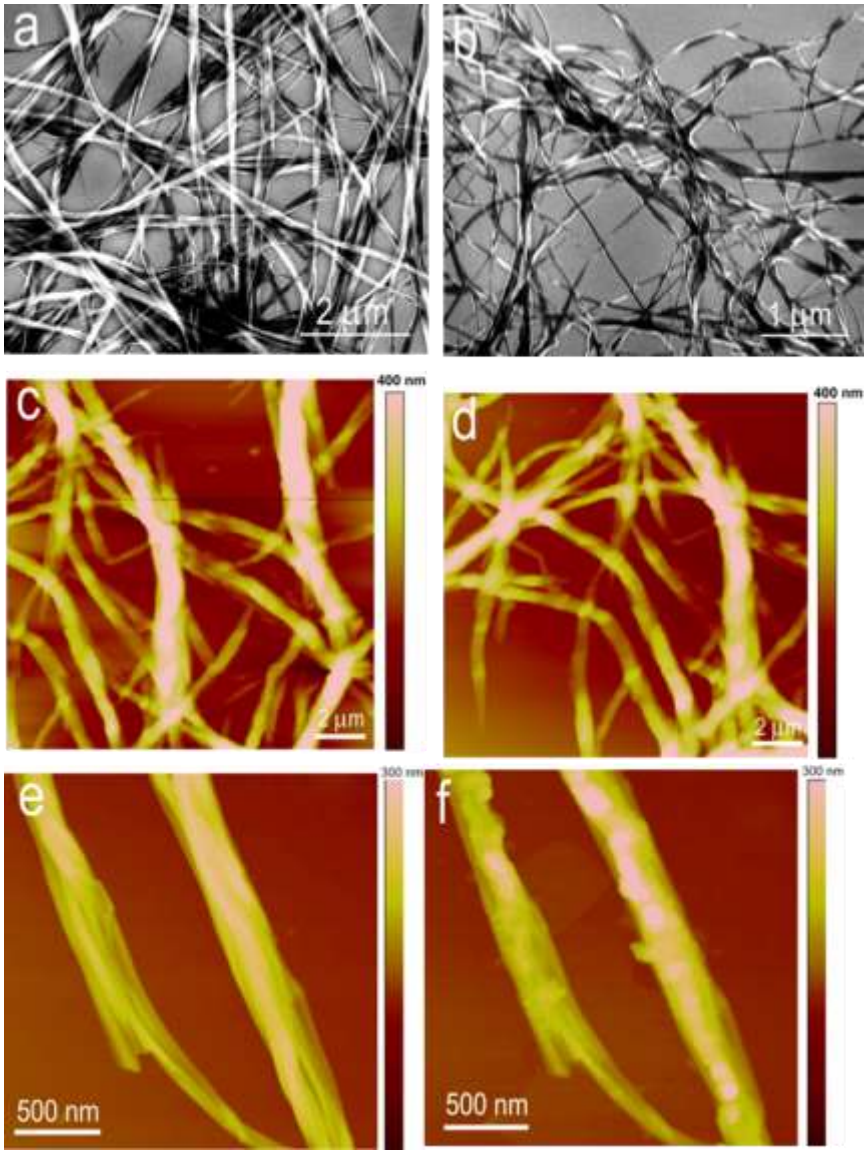

Figure 2.2 A-1 nanofibers before (a, c, e) and after (b, d, f) coated with D-1 molecules. **a)** SEM image of pristine nanofibers deposited on the silica. **b)** SEM image of the nanofibers (7.5 nmol **A-1** molecules) after being coated with **D-1** by drop-casting an ethanol solution of **D-1** (4 nmol) onto the fibril network as shown in 1a, where almost no separate phase of **D-1** was formed in between the nanofibers. **c)** and **e)** AFM image of the same **A-1** nanofibers as shown in 1a. **d)** and **f)** AFM image of the **D-1** coated nanofibers as shown in 1b. AFM imaging clearly shows the surface deposition of **D-1** as envisioned by the increased z-height of the line scanning profile. However, no apparent thickness increase was found for the spare area between the nanofibers, indicating effective concentration of **D-1** onto the nanofibers.

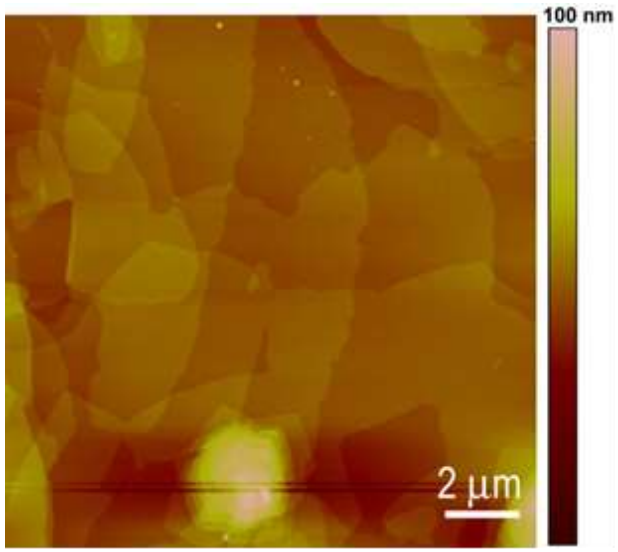

Figure 2.3 AFM image of a **D-1** film formed by drop-casting the ethanol solution (0.1 mM) onto a silica substrate. Due to the surface dewetting, the film was formed in a broken pattern, consisting of thin flakes and some chunky aggregates.

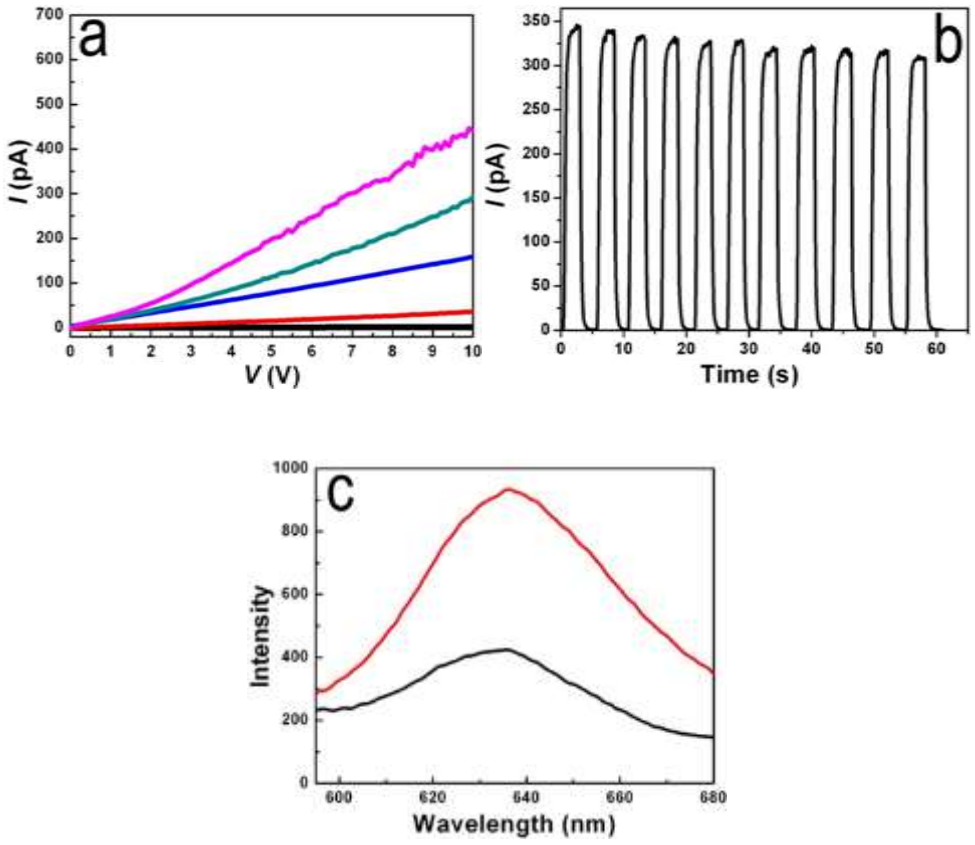

Figure 2.4 The photocurrent and fluorescence spectra of **D-1**/**A-1** heterojunction. I-V curves (a) measured over the **A-1** nanofibers with increasing deposition of **D-1** through drop-casting of the ethanol solution (0.1 mM) (black: pristine nanofibers containing 7.5 nmol **A-1**; red, blue, green, magenta: deposition of 1, 2, 3, 4 nmol **D-1**, respectively); white light irradiation was set at a power density of 0.17 mW/mm^2. Photocurrent (b) measured at 10 V of bias in response to turning on and off the white light irradiation (0.17 mW/mm^2). Fluorescence spectra (c) of **A-1** nanofibers (containing 7.5 nmol **A-1**) measured before (red) and after (black) deposition of 1 nmol **D-1**. Electrode-pairs used: 5 μm in gap, 14 μm in width. All measurements were carried out under ambient condition.

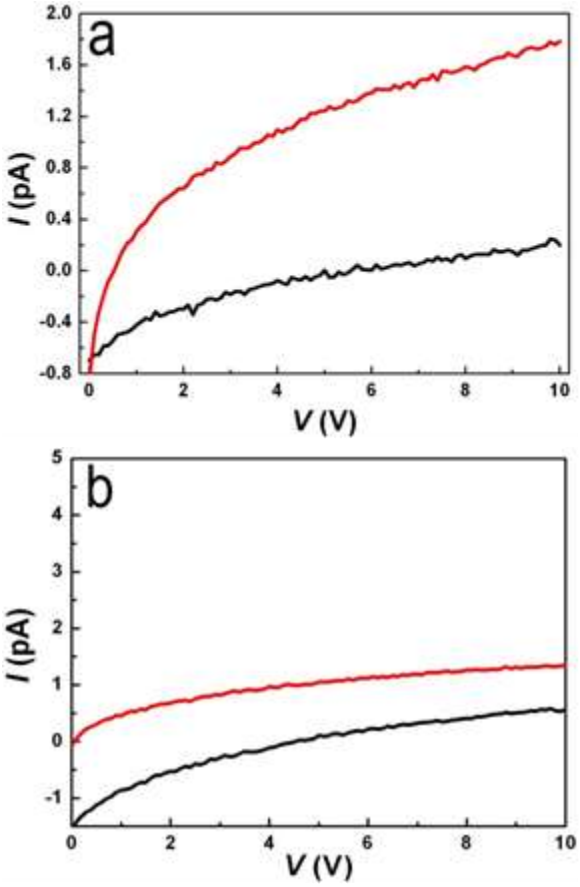

Figure 2.5. The photocurrent of **D-1** and **A-1**. I-V curve (a) measured over pristine **A-1** nanofibers in the dark (black) and under white light irradiation of power density 0.17 mW/mm^2 (red). I-V curve (b) measured over **D-1** film in the dark (black) and under white light irradiation of power density 0.17 mW/mm^2 (red).

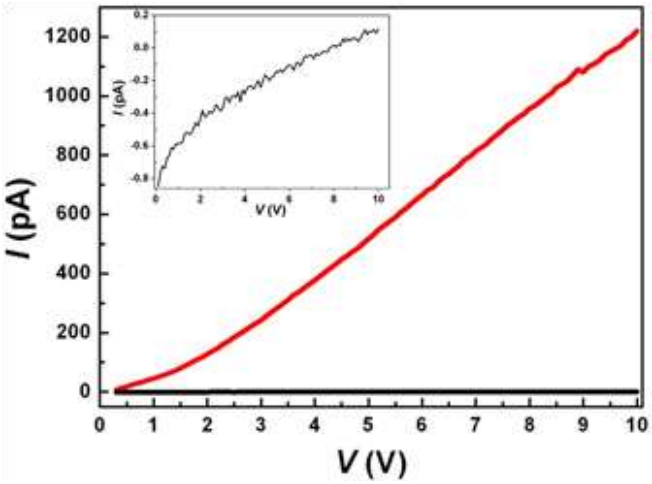

Figure 2.6 The photocurrent of **D-1**/**A-1** heterojunction. I-V curves measured over the nanofibers of **A-1** (7.5 nmol) coated with 4 nmol **D-1** molecules as deposited on a wide electrode-pair (90 μm in width and 5 μm in gap): (black) in the dark and (red) under white light irradiation of power density 0.17 mW/mm^2. Inset: dark current (black) in zoom-in scale.

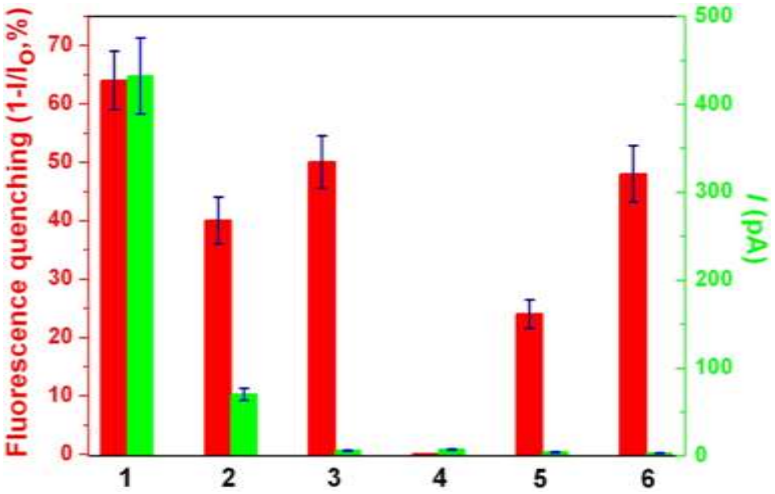

Figure 2.7 Comparison of optical and electrical performance between various **D/A** heterojunctions. The red and green columns denote fluorescence quenching and photocurrent measurement, respectively. (**1)** nanofibers of **A-1** (7.5 nmol) deposited with 4 nmol **D-1**; (**2)** nanofibers of **A-1** (7.5 nmol) deposited with 60 nmol **D-2**; (**3)** nanofibers of **A-1** (7.5 nmol) deposited with 20 nmol **D-3**; (**4)** nanofibers of **A-2** (7.5 nmol) deposited with 15 nmol **D-1**; (**5)** film of **A-3** (10 nmol) deposited with 20 nmol **D-1**; (**6)** film of **A-3** (10 nmol) deposited with 60 nmol **D-3** (10 nmol and 60 nmol, respectively). Electrode configuration and measurement conditions are the same as employed in Figure 2.4.

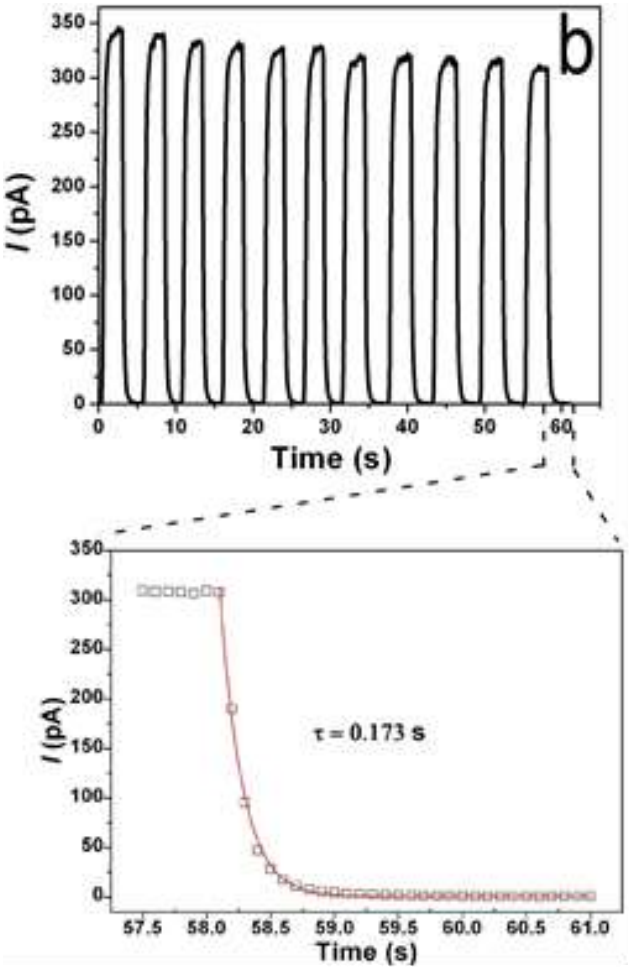

Figure 2.8 Exponential fitting of the generation and decay of the photocurrent, giving the response time of ca. ms.

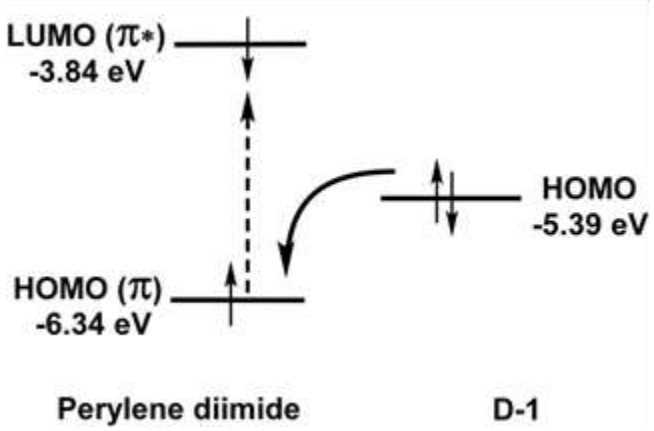

Figure 2.9 Energy level of HOMO (π) and LUMO (π*) orbitals of perylene diimide (**A**) and HOMO orbital of **D-1** (-5.39 eV) showing the favorable photoinduced electron transfer with large driving force (0.95 eV). Since the absorption of carbazole compounds is in the UV region (< 400 nm), visible irradiation of the heterojunction materials causes excitation of only the perylene diimide part. Geometry optimization and energy calculation were performed with density-functional theory (B3LYP/6-311g**// B3LYP/6-31g*) using Gaussian 03 package.

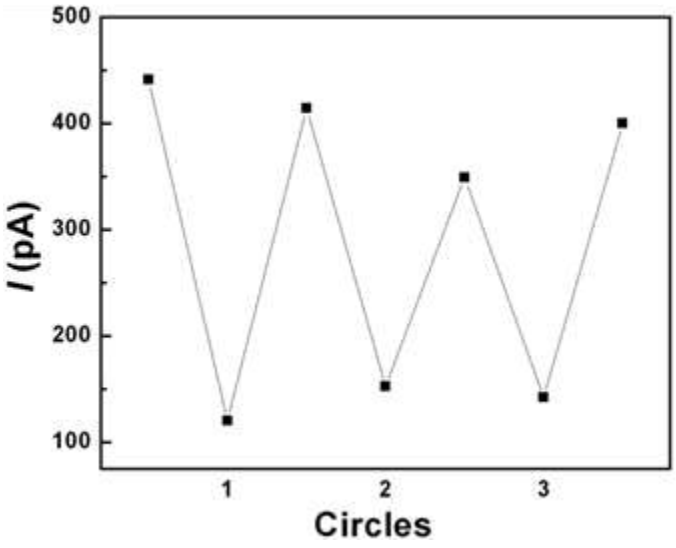

Figure 2.10 Reversible photocurrent generation of **A-1** nanofibers upon desorption and readsorption of **D-1** molecules.

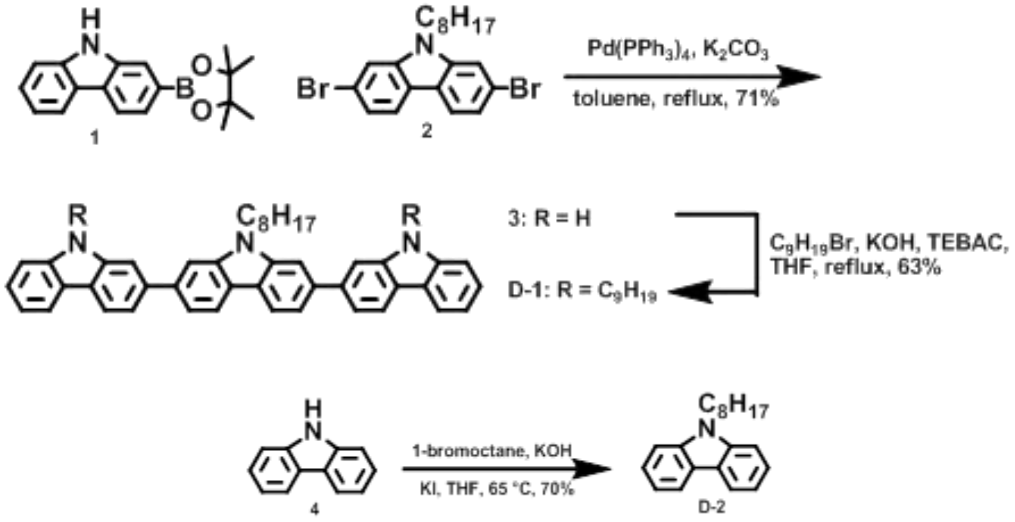

Figure 2.11 Synthesis steps for **D-1** and **D-2**.

CHAPTER 3

MORPHOLOGY CONTROL OF NANOFIBRIL DONOR-ACCEPTOR HETEROJUNCTION TO ACHIEVE HIGH PHOTOCONDUCTIVITY: EXPLORATION OF NEW MOLECULAR DESIGN RULE

3.1 Abstract

Donor-acceptor nanofibril composites have been fabricated, and the dependence of their photocurrent response on the structure and morphology of the donor part have been systematically investigated. The nanofibril composites were composed of template nanofibers, assembled from an electron acceptor molecule, perylene tetracarboxylic diimide (PTCDI), onto which (through drop-casting) various electron donor molecules (**D1**–**D4**) were coated. The donor molecules have the same π-conjugated core, but different side groups. Due to the different side groups, the four donor molecules showed a distinctly different propensity for intermolecular aggregation, with **D1**–**D3** form segregated phases, while **D4** prefers homogeneous molecular distribution within the film. It was found that the nanofibril composites with **D4** exhibit the highest photocurrent, whereas those with aggregation-prone **D1**–**D3** exhibited much lower photocurrent under the same illumination condition. Solvent annealing is found to further enhance the aggregation of **D1**–**D3** but facilitate more uniform molecular distribution of **D4** molecules. As a result, the photocurrent response of PTCDI fibers coated with **D1**–**D3** while those coated with **D4**

further increased. The detrimental effect of the aggregation of donor molecules on the PTCDI fiber is likely due to the enhanced local electrical field built up by the high charge density around the aggregate-nanofiber interface, which hinders the charge separation of the photogenerated electron-hole pair. The results reported in this study give further insight into the molecular structural effect on photoconductivity of hybrid materials, particularly those based on donor-acceptor composites or interfaces, and provide new molecular design rules and material processing guidelines to achieve high photoconductivity.

3.2 Introduction

Fabrication of effective donor-acceptor heterojunction structures remains critical for developing high-performance organic photovoltaics and the relevant photoelectric switches and sensors [1–5]. However, most of the research efforts to date have focused on bulk heterojunctions, which are formed through the not-easily-controlled phase separation process [6–12]. More ordered heterojunction structures, particularly those controllable at the nanometer scale through molecular design and engineering, are desirable in order to achieve high photoconversion efficiency [13]. Self-assembly has proven to be an efficient bottom-up method to construct well-defined nanostructures that may afford high photoconductivity [14–16]. A few examples have been reported on the design and fabrication of nanostructured heterojunction systems through molecular self-assembly [3, 17–24]. Most of these systems, however, either form a well-ordered structure only on a small area or require complicated molecular synthesis and thus are not suited for practical applications.

Recently, we have developed a novel approach based on nanofibril heterojunction to

achieve high photoconductivity for organic materials [3]. The approach relies on interfacial structural modification of nanofibers fabricated from electron acceptor (A) molecules onto which a layer of electron donor (D) molecules is coated. The A molecules are based on derivatives of perylene tetracarboxylic diimide (PTCDI), which represent a robust class of semiconductor materials with high thermal- and photostability [25]. The strong hydrophobic interdigitation between the long alkyl side-chains of D and A molecules enables efficient charge transfer between the two under photoexcitation. Such nanofibril heterojunctions possess two prominent features that are critical for efficient photocurrent generation: one is that the nanofibers both create a wide D/A interface for increased charge separation and act as long-range transport pathway for photogenerated charge carriers toward the electrodes and the other is that the alkyl side-chains employed not only enable effective surface adsorption of D molecules on the nanofibers for effective electron-transfer communication, but also facilitate spatial separation the photogenerated charge carriers to prevent their recombination. The surface coating method thus developed represents a simple, adaptable method that will allow for further improvement of organic photoconductivity through molecular design and supramolecular engineering. In the present work, we aim to explore the effects of aggregation of D molecules on the photoconductivity of nanofibril heterojunctions. A series of D molecules with varying side-chain modifications were synthesized [26] and investigated for the different intermolecular arrangements caused by π-π stacking in balance with steric hindrance of side-chains. Interestingly, it was observed that the different molecular assemblies of D resulted in distinctive phase segregation between D and A (the nanofiber), which significantly affects the interfacial charge transfer and separation as indicated from the measurements of

fluorescence quenching and photocurrent generation.

3.3 Results and discussion

3.3.1 Nanofibril heterojunction fabrication

Figure 3.1 shows the structures of the four D molecules employed in this study, which are based on the same tribenzopentaphene (TBP) core. The rigid, planar π-conjugated TBP core is conducive for cofacial π-π stacking that often leads to the formation of one-dimensional molecular assembly. The highest occupied molecular orbital (HOMO) of TBP molecules is significantly higher than that of PTCDI, providing sufficient driving force for the photoinduced TBP to PTCDI electron transfer. All four TBP molecules (**D1**–**D4**) have two dodecyl chains attached at the same positions. These linear alkyl chains help anchoring the D molecules onto the nanofiber of A through hydrophobic alkyl chain interdigitation as observed before [3, 25, 27]. At the periphery of the TBP core, different side chains were attached for **D1**–**D4** so that the intermolecular arrangement between TBP cores could be modulated, whereas the interfacial interaction between PTCDI and the four D molecules is expected to be comparable due to their identical dodecyl anchoring chains. Systematic investigation on how the intermolecular aggregation of the coated D molecules affect the photocurrent response of the PTCDI nanofibers would provide deeper understanding of the photoinduced charge separation process at the nanofibril heterojunction and open more options to further increase the photocurrent through structural optimization of the D component.

Side group modification has proven to be an effective way for tuning the intermolecular interactions, leading to different aggregated morphologies and electronic properties [28].

Such molecular structural effect can be more clearly manifested under solvent vapor annealing, which facilitates the self-assembly of molecules to reach the thermodynamically stable (energy minimal) state by removing the grain boundaries formed during the fast solvent vaporization process. Indeed, solvent vapor annealing has been extensively studied for organic semiconductor materials and devices in order to improve the crystallinity and charge carrier mobility [29–32]. In this study, we adopted this annealing process to facilitate the assembly of D molecules so that the effect of peripheral side group modification can be revealed more illustriously. Among the four D molecules, **D4** is expected to have the most severe steric hindrance for π-π stacking due to its bulkier side groups. The other three molecules on the other hand possess relatively small peripheral groups and are thus prone for π-π staking aggregation. As shown below, the different extent of intermolecular aggregation in the four D molecules has a dramatic effect on the photocurrent response of the core PTCDI nanofibers. With the coating of **D4**, which shows no π-π stacking even after solvent annealing, the PTCDI nanofibers exhibit the highest photocurrent. When coated with **D1**, **D2,** and **D3** molecules, which are prone to aggregation, the photocurrent response is significantly lower. The difference is more dramatic for the D-A nanofibril heterojunctions after solvent vapor annealing.

The nanofiber of A was fabricated from a PTCDI molecule (Figure 3.1) following the previously published self-assembly protocol [27]. The PTCDI molecule has a dodecyl chain at both imide positions to ensure strong hydrophobic alkyl chain interdigitation with the D molecules. The nanofibers were subsequently surface-coated with D molecules using the drop-casting method previously employed for creating similar nanofibril heterojunctions [3]. The as-prepared nanofibers possess well-defined morphologies and

large aspect ratios, providing large interface for surface adsorption of D molecules. Figure 3.2 shows the insitu AFM images of PTCDI nanofibers before and after surface coating of **D4** molecules. Almost all of the D molecules are coated onto the surface of nanofibers after drop-casting, leaving little residue on the silicon oxide substrate. Similar phenomena were observed for other three D molecules, **D1**–**D3** (Figure 3.3). The clean and selective deposit of D molecules onto the PTCDI fibers is attributed to the strong hydrophobic interdigitation between the dodecyl chains of D and that of PTCDI molecules on the nanofiber surface. Meanwhile, the morphology of individual nanofibers and the intertwining configuration remain unchanged after drop-casting, indicating the robustness of nanofibril structures on the substrate. Such a feature enables comparative studies of PTCDI nanofibers modified with different D molecules, allowing the pinpoint of different photocurrent response on the surface-coated D molecules.

3.3.2 Effect of intermolecular aggregation photoconductivity

Figure 3.4 (a) shows the fluorescence spectra of the PTCDI nanofibers before and after the coating of **D4** molecules, which indicates that 80% of the PTCDI fluorescence was quenched after **D4**-coating. The significant fluorescence quenching is due to the forward electron transfer from **D4** molecules to the photoexcited PTCDIs. This photoinduced electron transfer is thermodynamically favored with a driving force of 1.13 eV, calculated between the highest occupied molecular orbital (HOMO) levels of **D4** and PTCDI molecules (Figure 3.5). Consistent with the efficient fluorescence quenching, high photoconductivity was observed for the **D4**/PTCDI nanofibril heterojunction (Figure 3.4 (b)), for which an on/off ratio of ca. 10^4 was obtained under a 10 V bias. The high

photoconductivity was due to an optimal balance between the forward and back electron transfer between **D4** coating and the PTCDI nanofibers as discussed below. It is possible that the increased photocurrent may be due to the conductivity of the **D4** coating itself. However, this possibility was excluded since the dark- and photocurrent of **D4** film under the same light illumination (Figure 3.6) was only around 1 pA under 10 V bias, which is three orders of magnitude lower than that of **D4**/PTCDI nanofibers (Figure 3.4 (b)). Moreover, the **D4** film does not demonstrate photoconductivity response (i.e., the I-V curves obtained under dark and light illumination remained almost the same) (Figure 3.6).

The same experiments shown in Figure 3.4 were also performed on the PTCDI nanofibers coated with other three D molecules, **D1**–**D3**, in order to investigate the effect of molecular structure of D on the photoconductivity of D/A nanofibril heterojunctions. Figure 3.7 shows the results of fluorescence quenching and photocurrent measurements performed on the four different nanofibril heterojunctions. While all four nanofibers showed comparable fluorescence quenching after D-coating, the photocurrents generated were dramatically different, with the **D4**/PTCDI nanofiber giving the highest photocurrent. The efficient fluorescence quenching is consistent with the energetically favorable forward electron transfer from the D molecule to the photoexcited A, for which the driving force was calculated to be in the range of 0.7–1.1 eV (Figure 3.5). However, efficient forward electron transfer does not necessarily produce high electrical current, which also depends on other factors such as the subsequent charge separation of the photogenerated D^+-A^- pair to free charge carriers and the charge carrier mobility. Charge recombination (or back electron transfer) within D^+-A^- pair is often one of the major reasons for low photocurrent.

It is particularly intriguing to compare **D3** and **D4**. Both have alkoxy side groups and

very close HOMO levels. When coated on PTCDI fibers, they exhibit identical extent of fluorescence quenching. The photocurrent response of the two heterojunctions, however, differ by almost five times. The difference in photocurrent was even more dramatic for the nanofibers coated with **D1** and **D2**, which showed photocurrent values more than 10 and 50 times, respectively lower than that of **D4**-coated fibers (Figure 3.7). Considering the similar fluorescence quenching efficiency among the four nanofibers, we suspected that the lower photocurrent observed with the nanofibers coated with **D1**–**D3** (compared to that of **D4**) was primarily due to the less efficient charge separation (or faster charge recombination) of the photogenerated D^+-A^- pair, which has something to do with the phase segregation of surface-coated D molecules. The bulky side group of **D4** prevents intermolecular π-π stacking, resulting in uniform molecular distribution of **D4** onto the PTCDI nanofibers. In contrast, **D1**–**D3**, with relatively small side groups, are prone to π-π stacking, which leads to the formation of segregated phases of aggregated D molecules. AFM images of the drop-casting films of **D1**–**D3** confirmed their self-assembly. Particularly for **D1** and **D3**, the preferred columnar stacking enabled formation of nanofibril structures (Figure 3.8 and Figure 3.9).

Results in Figure 3.7 suggest that aggregates of **D1**–**D3** can quench the fluorescence of PTCDI nanofiber in similar (or comparable) efficiency as the homogeneous coating of **D4**. This can be explained by the long distance exciton migration within the single crystalline nanofiber of PTCDI, where the exciton migration distance was in the range of hundreds of nanometers [25, 33]. Once the quenchers (molecules or aggregates) are distributed on the surface with sufficient density (i.e., spatially separated within the distance of exciton migration), the fluorescence of nanofibers can be effectively quenched as an exciton can

always encounter a quencher when migrating along the nanofiber within its lifetime [34]. Considering the high molar ratio (4/7) of D/A used in this study, it is reasonable to assume that the aggregates of **D1**–**D3** can cover the PTCDI nanofiber with high enough density, and the separation between the aggregates is significantly smaller than the exciton migration distance of PTCDI.

Although the aggregation of **D1**–**D3** does not affect fluorescence quenching efficiency, it caused a significant decrease in photocurrent compared to the case of **D4**. This is likely due to the locally enhanced recombination (rather than separation) of D^+-A^- charge pair photogenerated around the aggregate of D. The interfacial charge separation of D^+-A^- at PTCDI nanofiber is primarily caused by the intermolecular electron delocalization among the π-π stacked PTCDI molecules [3, 5, 35], and this charge delocalization can be further extended under electrical bias applied to the nanofiber. At the fibril section with an aggregated D domain, there may be multiple pairs of D^+-A^- photogenerated by quenching multiple excitons (as discussed above), making the electron delocalization along the PTCDI stacks more difficult due to the increased charge density [36–37]. Moreover, multiple charge pairs form a strong local electrical field, which can prevent the charge separation. These two effects result in enhanced charge recombination of D^+-A^-. In contrast, the homogenous coating of **D4** produces more uniform distribution of D^+-A^- pairs on the nanofiber, which can be effectively separated through the intermolecular electron delocalization along the nanofiber, leading to the generation of high photocurrent as shown in Figure 3.7.

It is interesting to note that among the three D molecules (**D1**–**D3**) that produced relatively low photocurrent (Figure 3.7), **D2** demonstrated the lowest current value,

significantly lower than the other two, although the fluorescence quenching efficiency of **D2** is even the highest. This additional lowering of photoconductivity is likely due to the hydroxyl side groups of **D2** (–OH), which affords redox interaction with electrons, functioning as a charge carrier trap as previously observed in n-type organic field effect transistors [38–40].

3.3.3 Surface potential of nanofibril heterojunction under illumination

To gain further insight into the photoinduced charge separation process within the nanofibril heterojunction of PTCDI, Kelvin probe force microscopy (KPFM) was used to image the surface potential change upon illumination in a similar way as previously performed on other organic heterojunctions [41, 42]. **D3** was chosen as a representative of the three donors (**D1**–**D3**) to form D/A heterojunction with PTCDI; these three donors prefer to form aggregates, which are easy to be imaged by AFM and distinguished from PTCDI fiber. The **D3**/PTCDI nanofibers were deposited onto an indium-doped tin oxide (ITO) coated glass slide and measured simultaneously for topography and surface potential images both in the dark and under white light illumination.

As shown in Figure 3.10 (a), well-defined morphology was observed for the PTCDI nanofiber with surface coating of **D3**. Figure 3.10 (b) shows the line scan profile of surface potential corresponding to the red line marked in Figure 3.10 (a). In the dark, the surface potential PTCDI fiber (domain I as marked) appears higher than that of **D3** aggregate (domain II), consistent with their HOMO level difference as shown in Figure 3.5. Upon white light illumination, PTCDI gets excited, initiating electron transfer from **D3** to the fiber. This charge separation was imaged as an increase in surface potential of the **D3**

phase, but a decrease for the PTCDI fiber (red plot in Figure 3.10 (b)). For comparison, the same KPFM measurements were also performed on a bare **D3** aggregate (domain III) for which no surface potential change was observed before and after white illumination (Figure 3.10 (c)). This is simply because that **D3** can barely be excited by visible light (Figure 3.11), and thus no charge separation can be initiated.

3.3.4 Solvent-annealing influence on photoconductivity

It is well known that fast evaporation of solvents during the drop-casting process rarely produces the thermodynamically stable (energy minimized) state with regard to the intermolecular arrangement and phase growth within organic materials. A large number of defects and grain boundaries can be formed during the rapid assembly of molecules, and the growth of small nuclei may be quenched when the solvent is dried. Postassembly treatment, like solvent vapor annealing (i.e., aging of organic materials in saturated solvent vapor), has proven to be an effective method to reorganize and optimize the intermolecular arrangement, and facilitate the phase growth to reach the thermodynamic stable state [29, 43–46]. Indeed, solvent vapor annealing has been commonly used in solar cell material processing to improve the crystalline organization of D and A phases, with the aim to facilitate the charge transportation [9, 47–53]. We expected that the above mentioned difference of photocurrent between the nanofibers coated with **D4** and **D1**–**D3** would be more profound if the nanofibers were subject to solvent vapor annealing, considering that the difference of phase morphology and its dependence on the molecular structure between **D4** and **D1**–**D3** can be maximized at the thermodynamic stable state.

D3 was chosen as a representative of **D1**–**D3** to study the effects of solvent vapor

annealing on the surface aggregation and the subsequent photoconductivity; the results were compared to those observed with **D4**. The annealing was performed in ethanol vapor as ethanol is a good solvent for **D1**–**D4**, but a poor one for the PTCDI. During the annealing process the crystalline structure of PTCDI nanofibers was expected to remain intact. Under the same annealing conditions, **D3** and **D4** coatings underwent a dramatically different transition of the aggregation state. For **D3**, optical microscopy imaging showed the growth of small aggregates into large needle-like structures (Figure 3.9). AFM imaging revealed that the small aggregates of **D3** are actually composed of fine nanofibril structures, which were formed during the drop-casting process. Formation of nanofibril structure is indicative of the favorable columnar π-π stacking of **D3**, which is consistent with planar geometry of TBP π-conjugation. Upon solvent vapor annealing these small nanofibers grew into needle-like chunks, though still remaining in an elongated shape (Figure 3.9). This observation indicates that **D3** is prone to crystallize into large elongated structures driven by the strong π-π stacking interaction. The **D4** coating on the other hand showed no obvious aggregation even after solvent vapor annealing (Figure 3.12).

The different behavior of **D3** and **D4** under solvent vapor annealing led to a distinct effect on the photocurrent response as measured over the PTCDI nanofibers coated with these two molecules (Figure 3.13). For **D3**, the photocurrent decreased to 14% of its pre-annealing value, whereas for **D4**, the photocurrent increased by 60%. The significant decrease in photoconductivity of **D3**/PTCDI nanofiber is likely due to the increased aggregation of **D3** induced by the solvent vapor annealing. As discussed above, the enlarged aggregated domains of D molecules are detrimental to the charge separation of D^+-A^- pairs due to the enhanced local electrical field. In contrast, for **D4**/PTCDI nanofiber

the bulky isopropoxyl substitution at **D4** prevents molecular aggregation, instead favoring the homogeneous distribution of molecules on surface. Such molecular distribution can be further facilitated under solvent vapor annealing, producing a coating layer with minimized aggregation, as indicated by the 60% increase in photocurrent shown in Figure 3.13. This annealing-enhanced molecular distribution of **D4** was supported by the solid-state fluorescence spectral measurement on a thin **D4** film drop-casting on a glass slide. The glass slide was pretreated with trichloro(octadecyl)silane (OTS) to generate a hydrophobic surface similar to that of PTCDI nanofiber. Before solvent vapor annealing, the fluorescence spectrum of **D4** film possesses a major peak at 465 nm, along with a shoulder peak at a shorter wavelength, 440 nm. Compared to the fluorescence spectrum of **D4** molecularly dispersed in ethanol (Figure 3.14), the fluorescence emission in solid state becomes more dominant at a longer wavelength (Figure 3.15), consistent with the enhanced intermolecular interaction as commonly observed for molecular assemblies. The 440 nm emission (characteristic of the fluorescence of individual molecules) remains in the solid film of **D4**, indicating the relatively weak intermolecular π-π interaction in comparison with the film of **D3**, where the strong π-π stacking results in almost no emission observed for the individual molecules (Figure 3.14 and Figure 3.15). After solvent vapor annealing, the 440 nm peak of **D4** film was significantly enhanced (Figure 3.16), implying more molecules originally "frozen" as aggregates during the fast evaporation of drop-casting now transformed into homogeneous molecular distribution. In contrast, for **D3** film there was no obvious change observed in the fluorescence spectrum upon solvent vapor annealing under the same condition (Figure 3.17). This is consistent with the strong intermolecular stacking, which leads to the formation of stable aggregates in the specific

nanofibril morphology (Figure 3.9). Although solvent vapor annealing facilitates the growth of the nanofibers of **D3** into larger elongated crystals, the electronic property of the solid phase still remains dominant with the π-π stacking as indicated by the unchanged fluorescence spectra.

3.4 Conclusion

In summary, we have investigated a series of electron donor molecules (**D1**–**D4**) that share the same π-conjugation core, but modified with different side groups. PTCDI fibers coated with such donor molecules showed a dramatically different photocurrent response. It was found that the nanofibers coated with homogeneously and molecularly distributed donor molecules (such as **D4)** exhibit the highest photocurrent, whereas those coated with segregated donor aggregates (such as **D1**–**D3)** show much lower photocurrent under the same illumination conditions. The aggregation of donor molecules on the surface of the PTCDI fibers may lead to the buildup of the local electrical field, which hinders the charge separation of the photogenerated electron-hole pairs. The different morphologies of molecular aggregates were mostly the result of side group modification of the donor molecules. Such structural effect was more clearly manifested by investigating the structure and morphology change of the drop-casting films upon solvent vapor annealing. The findings presented provide new insight into the molecular structural effect on photoconductivity of organic semiconductor materials, particularly those based on donor-acceptor composites or interfaces and open alternative ways to improve the photoconductivity by structural design and modification.

3.5 Experimental section

3.5.1 Materials

Synthesis of PTCDI and the nanofibril fabrication followed the previous reported methods [25, 54]. Detailed synthesis and structural characterization of **D1**–**D4** were published elsewhere [26]. A brief description of the synthesis is described here as the following. As shown in Figure 3.18, the key steps are the Suzuki–Miyaura coupling of biarylboronic acid derivatives (4a, 4b, 4c) with 1,2-bis(dodecyloxy)-4,5-diiodobenzene to form o-quinquephenyls (5a, 5b, 5c) and the subsequent Scholl oxidative cyclization to yield the TBP cores. The Suzuki-Miyaura coupling went smoothly and could proceed directly from 2-bromobiaryal derivatives (3a, 3b, 3c) as a one-pot synthesis with good overall yields (around 50%). The Scholl reactions were carried out using 5–10 equivalents of FeCl3 in a nitromethane/dichoromethane solvent mixture at 0 °C. Under these conditions, compounds D1, D3, and D4 were obtained in 15–30% yields. Compound D2 was synthesized from D4 in excellent yields using B-bromo-9-BBN as the dealkylation reagent. The structures and purity of all four donor molecules (**D1**–**D4**) have been characterized and confirmed by 1H and 13C NMR, 2D COSY NMR, MAlDI-TOF mass spectrometry measurements, and elemental analysis.

To coat the PTCDI nanofibers with D molecules, 7 nmol of nanofibers were deposited onto a 5 mm × 5 mm silicon wafer covered with 300-nm thick SiO_2, followed by drop-casting of 4 nmol of **D1**–**D4** dissolved in a 0.1 mM ethanol solution.

3.5.2 General characterization

UV-vis absorption spectra were measured on a PerkinElmer Lambda 25 spectrophotometer. The fluorescence spectra were taken on a PerkinElmer LS 55 spectrophotometer. Bright field and fluorescence optical microscopy images were obtained with a Leica DMI4000B inverted microscope equipped with an Acton SP-2356 Imaging Spectrograph system and Princeton Instrument Acton PIXIS:400B Digital CCD Camera System for high resolution full spectral recording. AFM measurement was performed in tapping mode on a Veeco MultiMode V scanning probe microscope, for which samples were directly drop-casting on a silicon wafer covered with a 300-nm thick SiO_2 layer. The electrical conductivity was measured using a two-probe method on a Signatone S-1160 Probe Station combined with an Agilient 4156C Precision Semiconductor Analyzer. A tungsten lamp was used as the light source with a light intensity of 0.17 mW/mm^2 on the testbed. The gold-electrode pair used was 14 μm in width and 5 μm in gap.

3.5.3 Kelvin probe force microscopy (KPFM)

Indium-doped tin oxide (ITO) coated glass slides (Delta Technology, R = 5–15 Ω) were used as substrates for KPFM measurements. Before use, ITO glass substrates were rinsed thoroughly with distilled water and ethanol, followed by drying with nitrogen blowing. Donor coated PTCDI nanofibers were deposited onto the ITO glass via drop-casting. KPFM experiments were performed with Bruker Dimension Icon equipped with an Extender Electronics module. Conductive antimony (n) doped silicon tips (SCM-PIT, Bruker) were used along with a cantilever coated with 20 nm Pt/Ir on both sides. Surface potential was measured using Lift Mode [55]. Briefly, a topographic line scan was first

recorded with Tapping Mode, and then the same line was rescanned in Lift Mode with 20 nm constant distance between the tip and substrate. The white light illumination was provided by a tungsten lamp, which delivered a light intensity of 10 mW/cm^2 on the substrate.

3.5.4 Preparation of surface-modified glass slides

The glass slides were first thoroughly cleaned in acetone and isopropanol for 3 min each in an ultrasonic bath and then cleaned with a piranha solution (70 vol% H_2SO_4: 30 vol% 30% H_2O_2) for 20 min, followed by rinsing with deionized water and drying in air flow. To form monolayer of octadecyl-trichlorosilane (OTS) on the surface, the glass slides were immersed in an anhydrous toluene solution of OTS (3 mM) for 3 h, followed by ultrasonic cleaning in fresh toluene solvent for 2 min to remove the excessive OTS residues. The glass slides were then baked on a 150 ºC hot plate for 1 h to enhance the surface crosslinking.

3.6 References

[1] Günes, S.; Neugebauer, H.; Sariciftci, N. S. *Chem. Rev.* **2007**, *107*, 1324–1338.

[2] Thompson, B. C.; Fréchet, J. M. J. *Angew. Chem. Int. Ed.* **2008**, *47*, 58–77.

[3] Che, Y.; Huang, H.; Xu, M.; Zhang, C.; Bunes, B. R.; Yang, X.; Zang, L. *J. Am. Chem. Soc.* **2011**, *133*, 1087–1091.

[4] Konstantatos, G.; Sargent, E. H. *Nat. Nanotechnol.* **2010**, *5*, 391–400.

[5] Che, Y.; Yang, X.; Liu, G.; Yu, C.; Ji, H.; Zuo, J.; Zhao, J.; Zang, L. *J. Am. Chem. Soc.* **2010**, *132*, 5743–5750.

[6] Halls, J. J. M.; Walsh, C. A.; Greenham, N. C.; Marseglia, E. A.; Friend, R. H.; Moratti, S. C.; Holmes, A. B. *Nature* **1995**, *376*, 498–500.

[7] Yu, G.; Gao, J.; Hummelen, J. C.; Wudl, F.; Heeger, A. J. *Science* **1995**, *270*, 1789–1791.

[8] Peumans, P.; Uchida, S.; Forrest, S. R. *Nature* **2003**, *425*, 158–162.

[9] Li, G.; Shrotriya, V.; Huang, J.; Yao, Y.; Moriarty, T.; Emery, K.; Yang, Y. *Nat. Mater.* **2005**, *4*, 864–868.

[10] Kim, J. Y.; Lee, K.; Coates, N. E.; Moses, D.; Nguyen, T.-Q.; Dante, M.; Heeger, A. J. *Science* **2007**, *317*, 222–225.

[11] Park, S. H.; Roy, A.; Beaupre, S.; Cho, S.; Coates, N.; Moon, J. S.; Moses, D.; Leclerc, M.; Lee, K.; Heeger, A. J. *Nat. Photon.* **2009**, *3*, 297–302.

[12] He, Z.; Zhong, C.; Huang, X.; Wong, W.-Y.; Wu, H.; Chen, L.; Su, S.; Cao, Y. *Adv. Mater.* **2011**, *23*, 4636–4643.

[13] Chang, C.-Y.; Wu, C.-E.; Chen, S.-Y.; Cui, C.; Cheng, Y.-J.; Hsu, C.-S.; Wang, Y.-L.; Li, Y. *Angew. Chem. Int. Ed.* **2011**, *50*, 9386–9390.

[14] Hoeben, F. J. M.; Jonkheijm, P.; Meijer, E. W.; Schenning, A. P. H. J. *Chem. Rev.* **2005**, *105*, 1491–1546.

[15] De Greef, T. F. A.; Smulders, M. M. J.; Wolffs, M.; Schenning, A. P. H. J.; Sijbesma, R. P.; Meijer, E. W. *Chem. Rev.* **2009**, *109*, 5687–5754.

[16] Aida, T.; Meijer, E. W.; Stupp, S. I. *Science* **2012**, *335*, 813–817.

[17] Percec, V.; Glodde, M.; Bera, T. K.; Miura, Y.; Shiyanovskaya, I.; Singer, K. D.; Balagurusamy, V. S. K.; Heiney, P. A.; Schnell, I.; Rapp, A.; Spiess, H. W.; Hudson, S. D.; Duan, H. *Nature* **2002**, *417*, 384–387.

[18] Würthner, F.; Chen, Z.; Hoeben, F. J. M.; Osswald, P.; You, C.-C.; Jonkheijm, P.; Herrikhuyzen, J. v.; Schenning, A. P. H. J.; van der Schoot, P. P. A. M.; Meijer, E. W.; Beckers, E. H. A.; Meskers, S. C. J.; Janssen, R. A. J. *J. Am. Chem. Soc.* **2004**, *126*, 10611–10618.

[19] Yamamoto, Y.; Fukushima, T.; Suna, Y.; Ishii, N.; Saeki, A.; Seki, S.; Tagawa, S.; Taniguchi, M.; Kawai, T.; Aida, T. *Science* **2006**, *314*, 1761–1764.

[20] Sisson, A. L.; Sakai, N.; Banerji, N.; Fürstenberg, A.; Vauthey, E.; Matile, S. *Angew. Chem. Int. Ed.* **2008**, *47*, 3727–3729.

[21] Yamamoto, Y.; Zhang, G.; Jin, W.; Fukushima, T.; Ishii, N.; Saeki, A.; Seki, S.; Tagawa, S.; Minari, T.; Tsukagoshi, K.; Aida, T. *Proc. Natl. Acad. Sci.* **2009**, *106*, 21051–21056.

[22] Sakai, N.; Bhosale, R.; Emery, D.; Mareda, J.; Matile, S. *J. Am. Chem. Soc.* **2010**, *132*, 6923–6925.

[23] Zhang, W.; Jin, W.; Fukushima, T.; Saeki, A.; Seki, S.; Aida, T. *Science* **2011**, *334*, 340–343.

[24] Sakai, N.; Matile, S. *J. Am. Chem. Soc.* **2011**, *133*, 18542–18545.

[25] Zang, L.; Che, Y.; Moore, J. S. *Acc. Chem. Res.* **2008**, *41*, 1596–1608.

[26] Chou, C.-E.; Li, Y.; Che, Y.; Zang, L.; Peng, Z. *RSC Advances* **2013**, *43*, 20666–20672.

[27] Balakrishnan, K.; Datar, A.; Naddo, T.; Huang, J.; Oitker, R.; Yen, M.; Zhao, J.; Zang, L. *J. Am. Chem. Soc.* **2006**, *128*, 7390–7398.

[28] Nguyen, L. H.; Hoppe, H.; Erb, T.; Günes, S.; Gobsch, G.; Sariciftci, N. S. *Adv. Funct. Mater.* **2007**, *17*, 1071–1078.

[29] Datar, A.; Oitker, R.; Zang, L. *Chem. Commun.* **2006**, 1649–1651.

[30] Dickey, K. C.; Anthony, J. E.; Loo, Y. L. *Adv. Mater.* **2006**, *18*, 1721–1726.

[31] Lu, G.; Li, L.; Yang, X. *Small* **2008**, *4*, 601–606.

[32] Chen, H.; Hu, S.; Zang, H.; Hu, B.; Dadmun, M. *Adv. Funct. Mater.* **2013**, *23*, 1701–1710.

[33] Chaudhuri, D.; Li, D.; Che, Y.; Shafran, E.; Gerton, J. M.; Zang, L.; Lupton, J. M. *Nano Lett.* **2011**, *11*, 488–492.

[34] Naddo, T.; Che, Y.; Zhang, W.; Balakrishnan, K.; Yang, X.; Yen, M.; Zhao, J.; Moore, J. S.; Zang, L. *J. Am. Chem. Soc.* **2007**, *129*, 6978–6979.

[35] Che, Y.; Datar, A.; Yang, X.; Naddo, T.; Zhao, J.; Zang, L. *J. Am. Chem. Soc.* **2007**, *129*, 6354–6355.

[36] Delgado, M. C. R.; Kim, E.-G.; Filho, D. t. A. d. S.; Bredas, J.-L. *J. Am. Chem. Soc.* **2010**, *132*, 3375–3387.

[37] Coropceanu, V.; Cornil, J.; da Silva Filho, D. A.; Olivier, Y.; Silbey, R.; Brédas, J.-L. *Chem. Rev.* **2007**, *107*, 926–952.

[38] Chua, L.-L.; Zaumseil, J.; Chang, J.-F.; Ou, E. C. W.; Ho, P. K. H.; Sirringhaus, H.; Friend, R. H. *Nature* **2005**, *434*, 194–199.

[39] Yoon, M.-H.; Kim, C.; Facchetti, A.; Marks, T. J. *J. Am. Chem. Soc.* **2006**, *128*, 12851–12869.

[40] Baeg, K.-J.; Facchetti, A.; Noh, Y.-Y. *J. Mater. Chem.* **2012**, *22*, 21138–21143.

[41] Liscio, A.; De Luca, G.; Nolde, F.; Palermo, V.; Müllen, K.; Samorì, P. *J. Am. Chem. Soc.* **2008**, *130*, 780–781.

[42] Palermo, V.; Otten, M. B. J.; Liscio, A.; Schwartz, E.; de Witte, P. A. J.; Castriciano, M. A.; Wienk, M. M.; Nolde, F.; De Luca, G.; Cornelissen, J. J. L. M.; Janssen, R. A. J.; Müllen, K.; Rowan, A. E.; Nolte, R. J. M.; Samorì, P. *J. Am. Chem. Soc.* **2008**, *130*, 14605–14614.

[43] Campoy-Quiles, M.; Ferenczi, T.; Agostinelli, T.; Etchegoin, P. G.; Kim, Y.; Anthopoulos, T. D.; Stavrinou, P. N.; Bradley, D. D. C.; Nelson, J. *Nat. Mater.* **2008**, *7*, 158–164.

[44] De Luca, G.; Liscio, A.; Battagliarin, G.; Chen, L.; Scolaro, L. M.; Mullen, K.; Samori, P.; Palermo, V. *Chem. Commun.* **2013**, *49*, 4322–4324.

[45] De Luca, G.; Liscio, A.; Maccagnani, P.; Nolde, F.; Palermo, V.; Müllen, K.; Samorì, P. *Adv. Funct. Mater.* **2007**, *17*, 3791–3798.

[46] De Luca, G.; Liscio, A.; Nolde, F.; Scolaro, L. M.; Palermo, V.; Mullen, K.; Samori, P. *Soft Matter* **2008**, *4*, 2064–2070.

[47] Hoppe, H.; Sariciftci, N. S. *J. Mater. Chem.* **2006**, *16*, 45–61.

[48] Yang, X.; Loos, J.; Veenstra, S. C.; Verhees, W. J. H.; Wienk, M. M.; Kroon, J. M.; Michels, M. A. J.; Janssen, R. A. J. *Nano. Lett.* **2005**, *5*, 579–583.

[49] Kim, H. J.; Lee, H. H.; Kim, J.-J. *Macromol. Rapid Commun.* **2009**, *30*, 1269–1273.

[50] Zhao, Y.; Xie, Z.; Qu, Y.; Geng, Y.; Wang, L. *Appl. Phys. Lett.* **2007**, *90*, 043504.

[51] Jo, J.; Na, S.-I.; Kim, S.-S.; Lee, T.-W.; Chung, Y.; Kang, S.-J.; Vak, D.; Kim, D.-Y. *Adv. Funct. Mater.* **2009**, *19*, 2398–2406.

[52] Bavel, S. S. v.; Sourty, E.; With, G. d.; Loos, J. *Nano. Lett.* **2008**, *9*, 507–513.

[53] Li, G.; Yao, Y.; Yang, H.; Shrotriya, V.; Yang, G.; Yang, Y. *Adv. Funct. Mater.* **2007**, *17*, 1636–1644.

[54] Che, Y.; Huang, H.; Xu, M.; Zhang, C.; Bunes, B. R.; Yang, X.; Zang, L. *J. Am. Chem. Soc.* **2011**, *133*, 1087–1091.

[55] Palermo, V.; Palma, M.; Samorì, P. *Adv. Mater.* **2006**, *18*, 145–164.

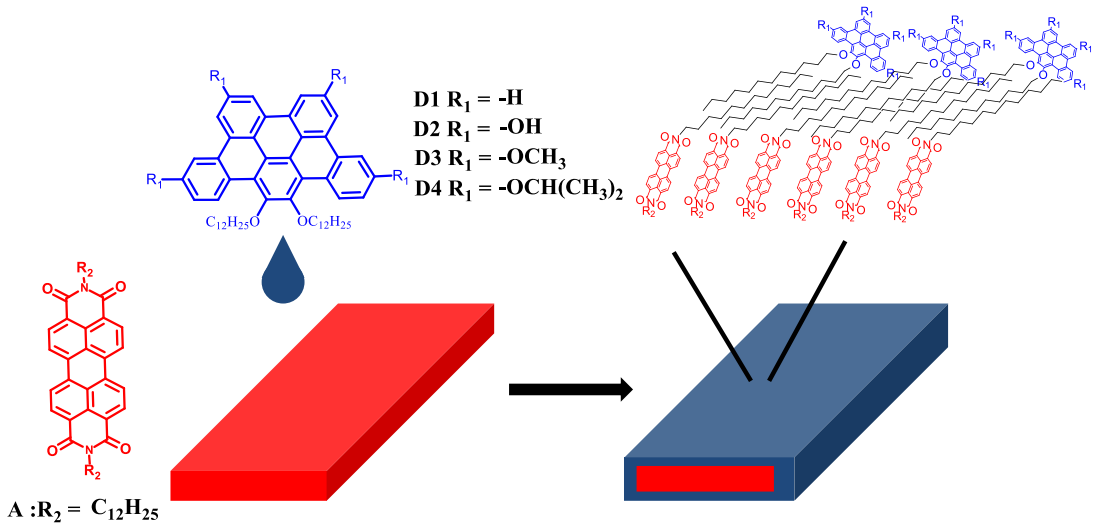

Figure 3.1 Schematic illustration of core-shell structured nanofibril heterojunction composed of **D1**–**D4** coating and PTCDI nanofiber.

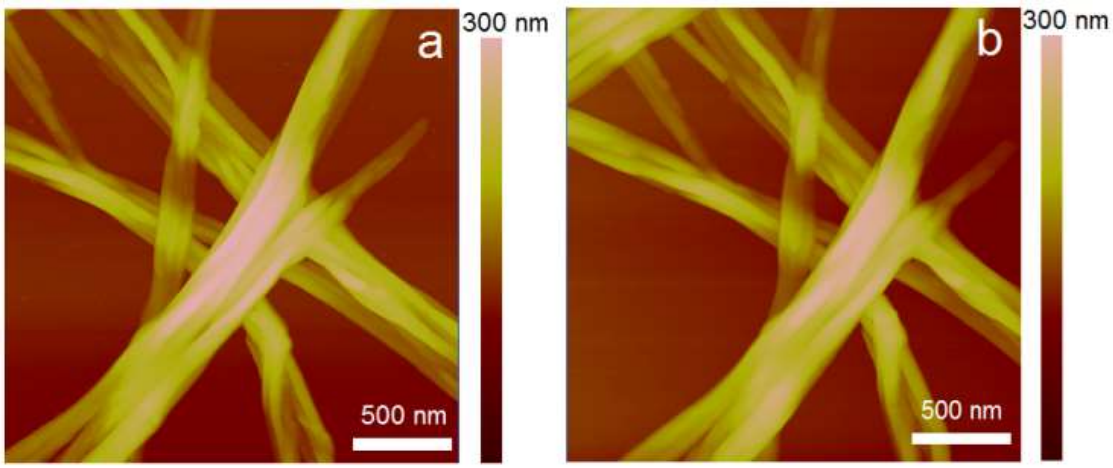

Figure 3.2 AFM images of PTCDI nanofibers (molecular amount of 7 nmol) deposited on a 5 mm × 5 mm silicon wafer covered with 300-nm thick SiO_2 before (a) and after (b) surface coating of **D4** (4 nmol).

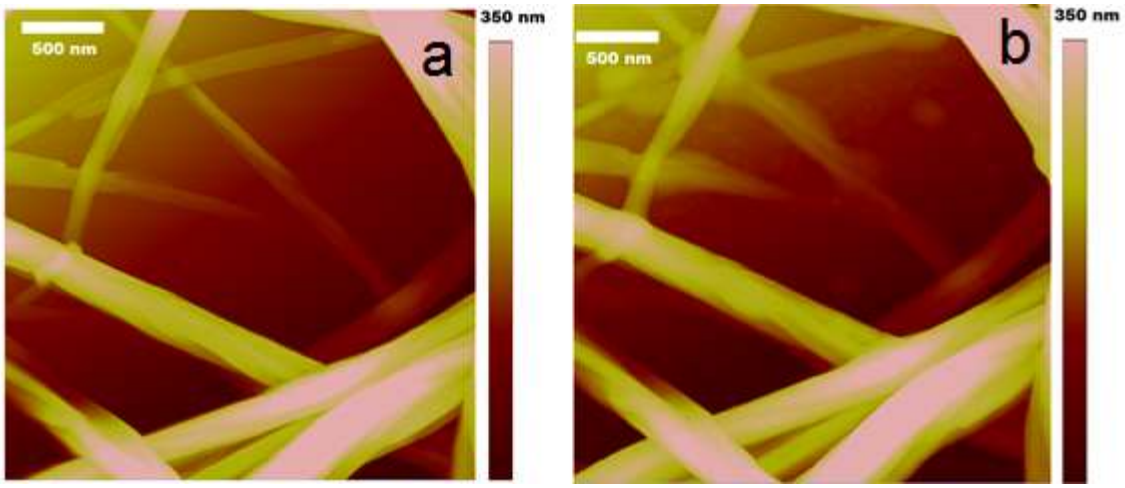

Figure 3.3 AFM images of PTCDI nanofibers drop-casting on the surface of silicon wafer covered with 300-nm thick SiO_2 before (a) and after (b) coating with **D2**.

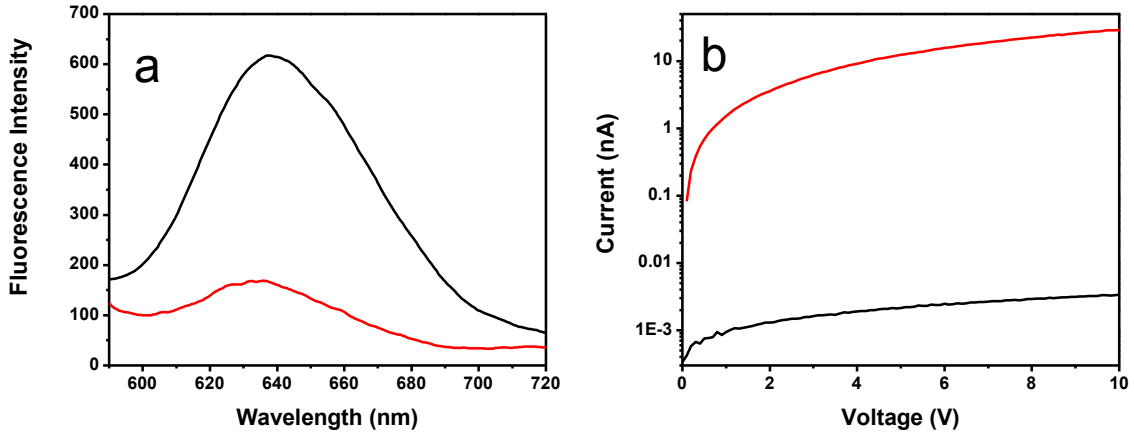

Figure 3.4 Photocurrent of fluorescence spectra of **D4** based heterojunction. Fluorescence spectra (a) of PTCDI nanofibers before (black) and after (red) drop-casting of **D4** and I-V curves (b) measured over the **D4** coated PTCDI nanofibers in the dark (black) and under white light irradiation of 0.17 mW/mm^2 (red).

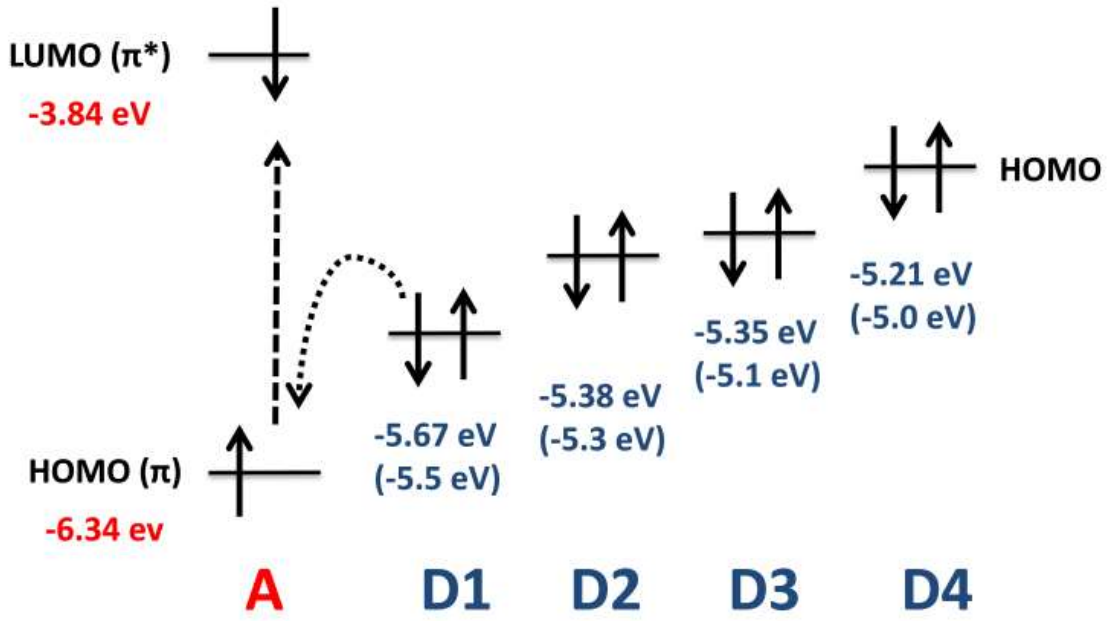

Figure 3.5 Electronic energy levels of PTCDI and **D1**–**D4**. The HOMO levels of **D1**–**D4** were determined by cyclic voltammetry using Fc/Fc^{+} as an internal standard [26]. The energy levels of PTCDI (A) and **D1**–**D4** (in parenthesis) were calculated with density-functional theory (B3LYP/6-311g**//B3LYP/6-31g*) using Gaussian 09 package.

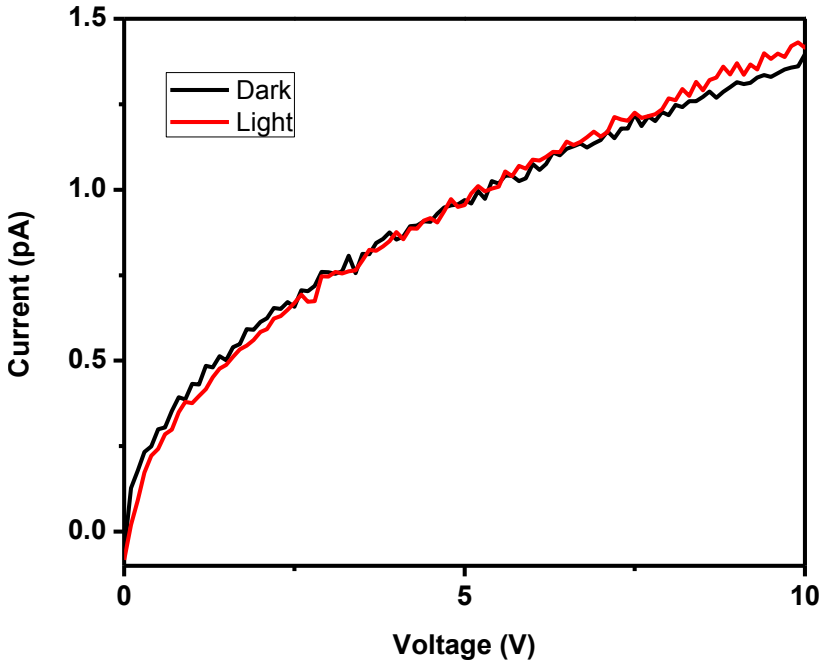

Figure 3.6 I-V curves measured for **D4** film in dark (black) and under light illumination (red).

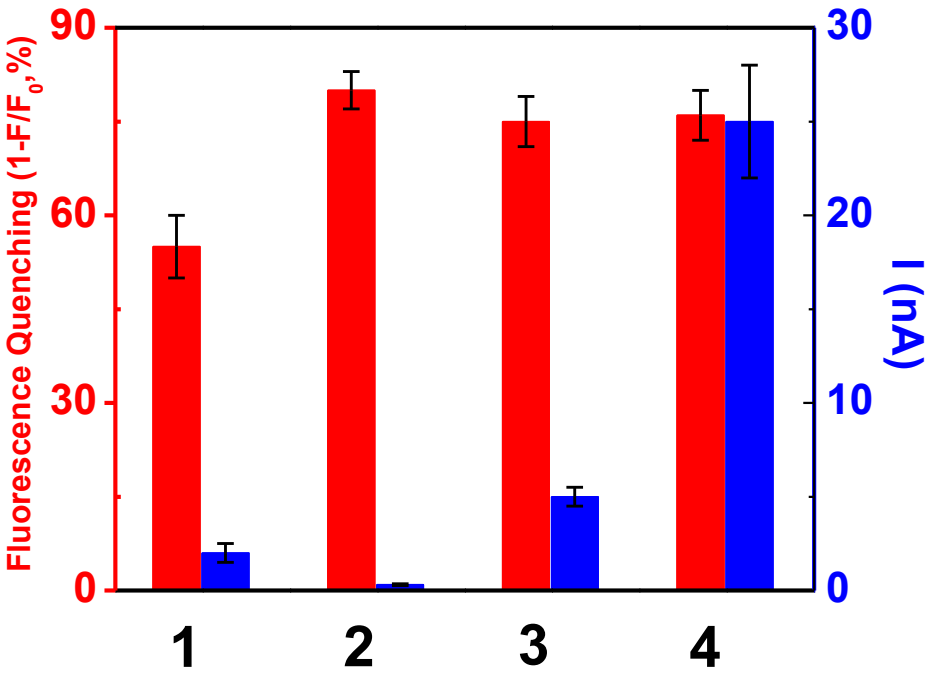

Figure 3.7 Comparison of fluorescence quenching (red) and photocurrent generation (blue) between the PTCDI nanofibers coated with the four donor molecules, **D1**–**D4**. Photocurrent values used in this plot were obtained at a bias voltage of 10 V.

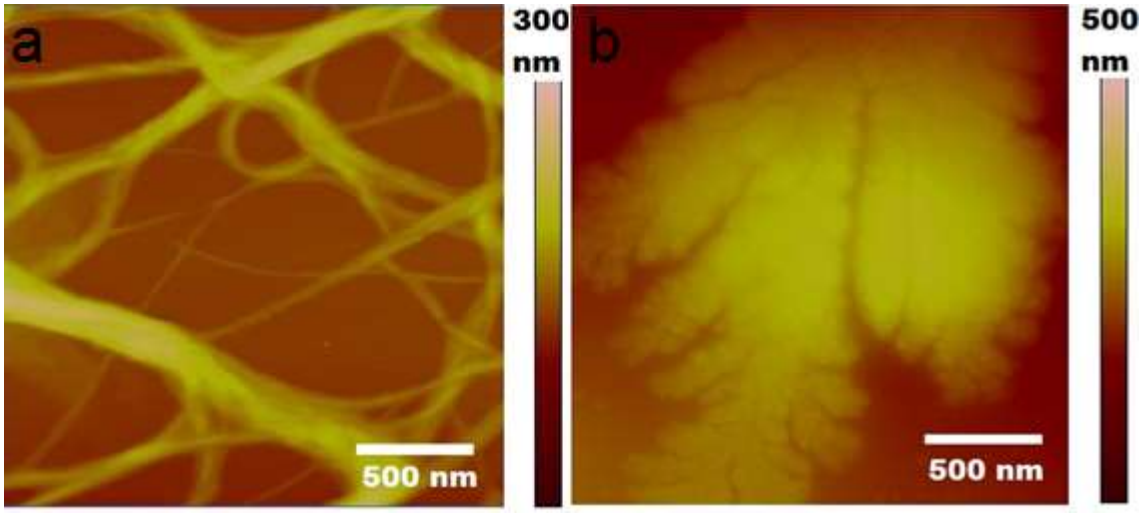

Figure 3.8 AFM images of **D1** (a) and **D2** (b) drop-casting on the surface of silicon wafer covered with 300-nm thick SiO_2.

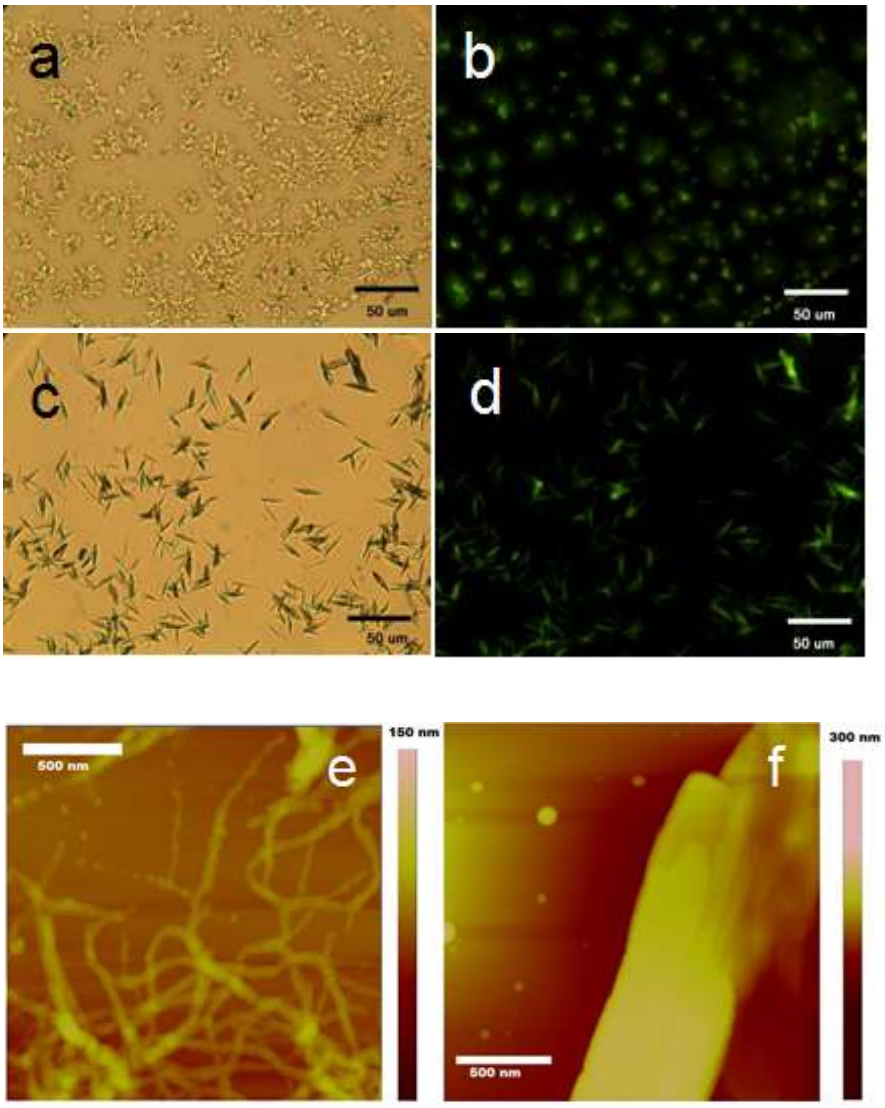

Figure 3.9 Microscopic images of **D3**. Bright field microscopy (a, c) and fluorescence microscopy images (b, d) of **D3** drop-casting on OTS modified glass surface before (a, b) and after (c, d) ethanol vapor annealing. AFM images of the same sample before (e) and after (f) ethanol vapor annealing.

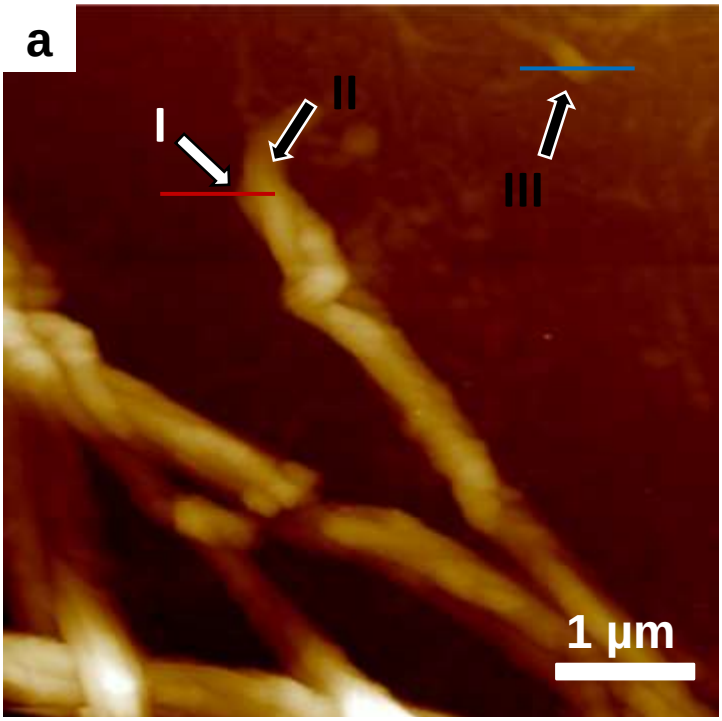

Figure 3.10 KPFM measurement of **D3**/PTCDI nanofibril heterojunction. (a) Topograhy image of the nanofibril heterojunction (Z height range 400 nm). PTCDI nanofiber, **D3** coating, and isolated **D3** aggregate are marked as domain (I), (II), and (III), respectively. (b, c) Line scans surface potential profiles obtained by tracing the corresponding lines marked (red, blue) in (a) under dark (black plot) and white light illumination of 10 mW/cm^2 (red plot).

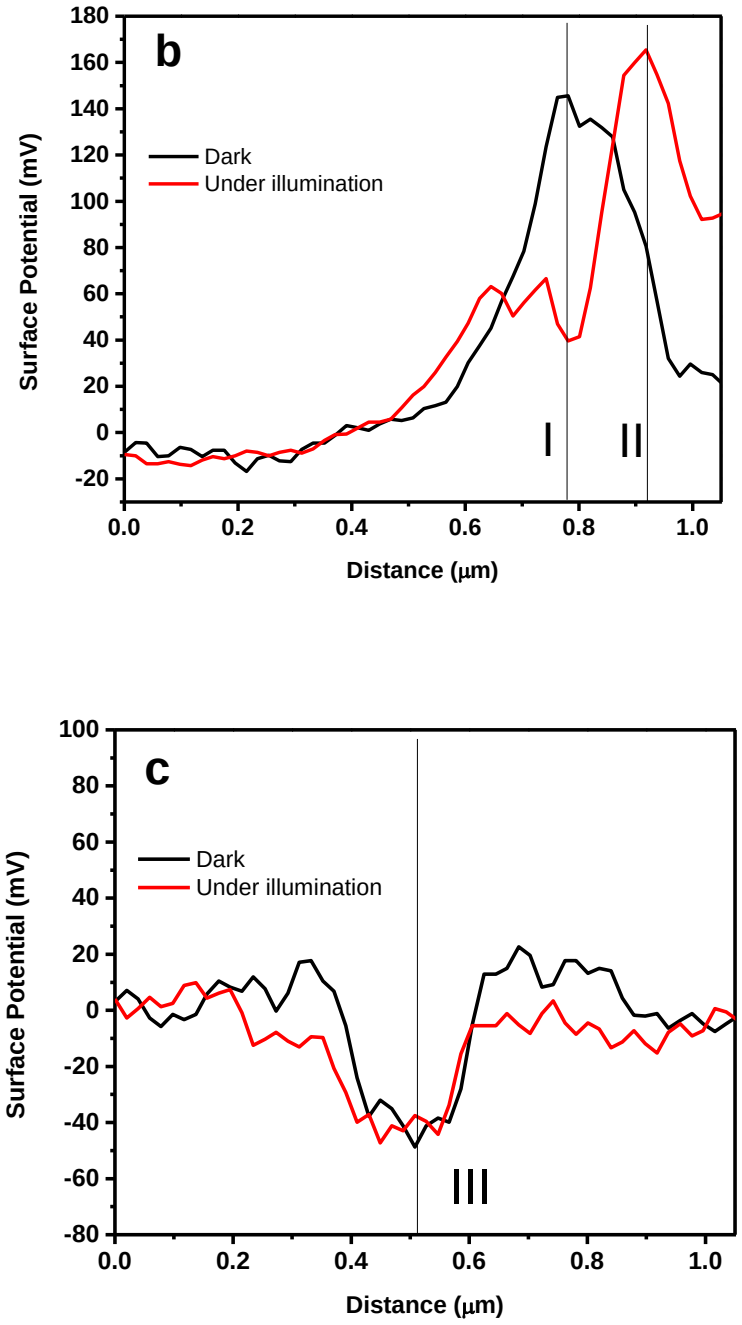

Figure 3.10 continued.

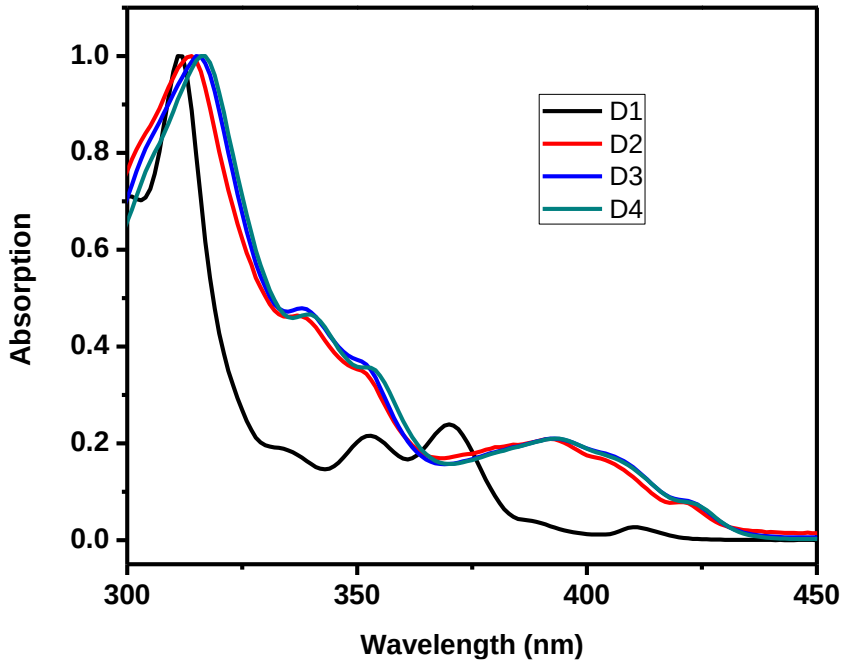

Figure 3.11 Normalized absorption of **D1**–**D4** in ethanol solution.

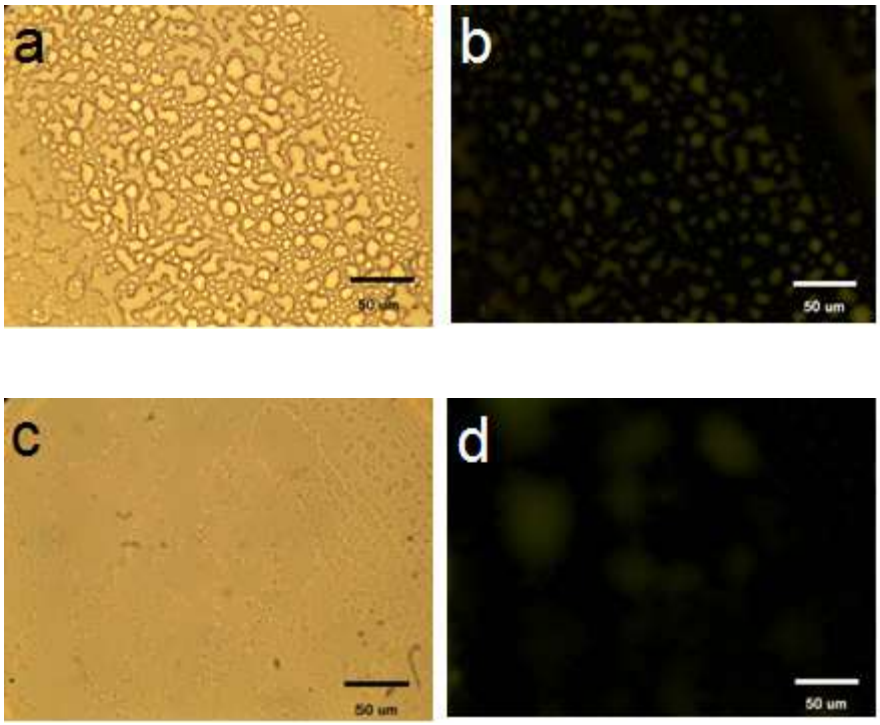

Figure 3.12 Microscopic images of **D4**. Bright field microscopy (a, c) and fluorescence microscopy images (b, d) of **D4** drop-casting on OTS modified glass surface before (a, b) and after (c, d) ethanol vapor annealing.

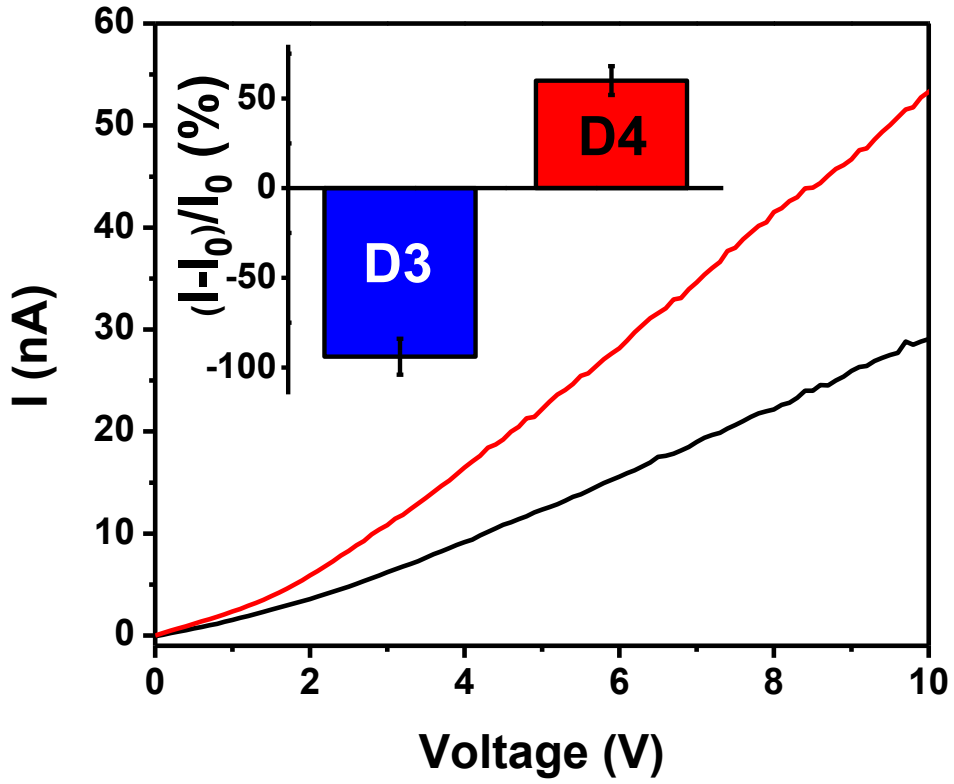

Figure 3.13 I-V curves measured over **D4** coated PTCDI nanofibers under light irradiation before (black) and after (red) solvent vapor annealing. Inset: relative photocurrent change (in percentage) for **D3** and **D4** coated nanofibers after solvent vapor annealing. Photocurrent values used in this plot were obtained at a bias voltage of 10 V.

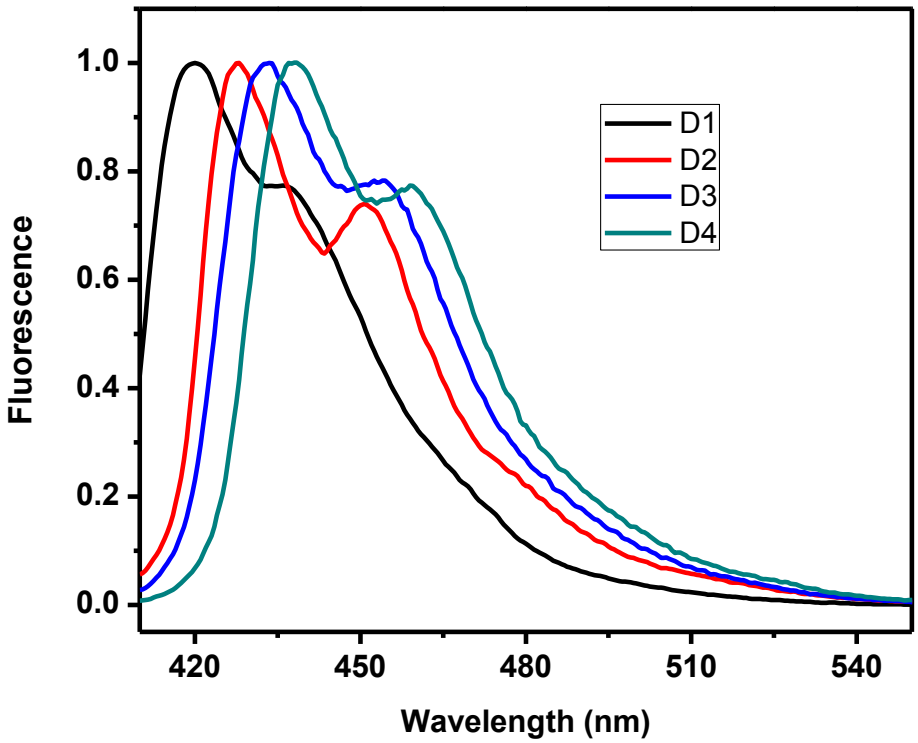

Figure 3.14 Normalized fluorescence spectra of **D1**–**D4** in ethanol solution.

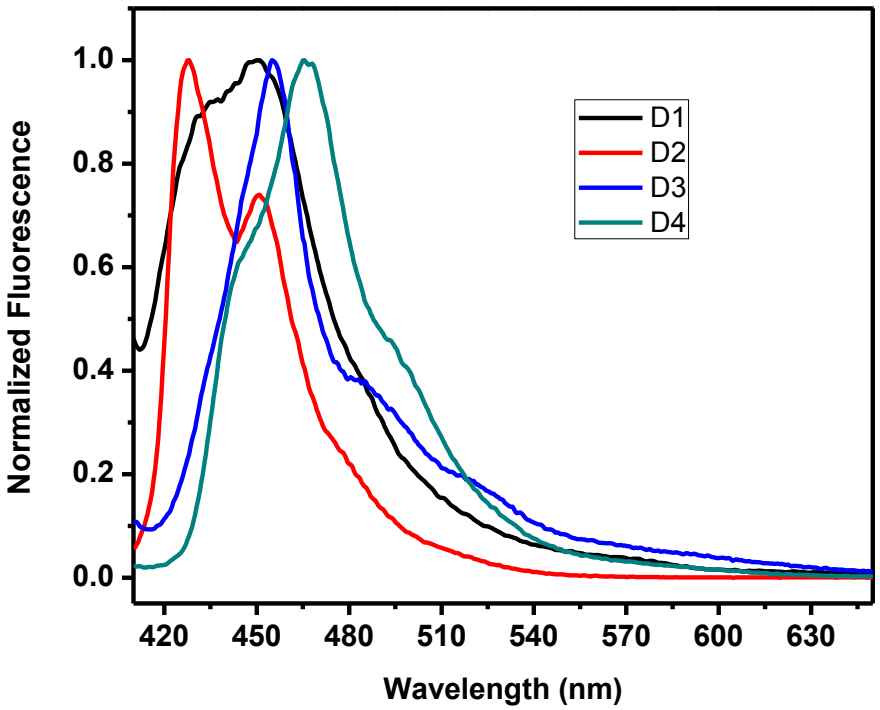

Figure 3.15 Normalized fluorescence spectra of **D1**–**D4** drop-casting on glass surface.

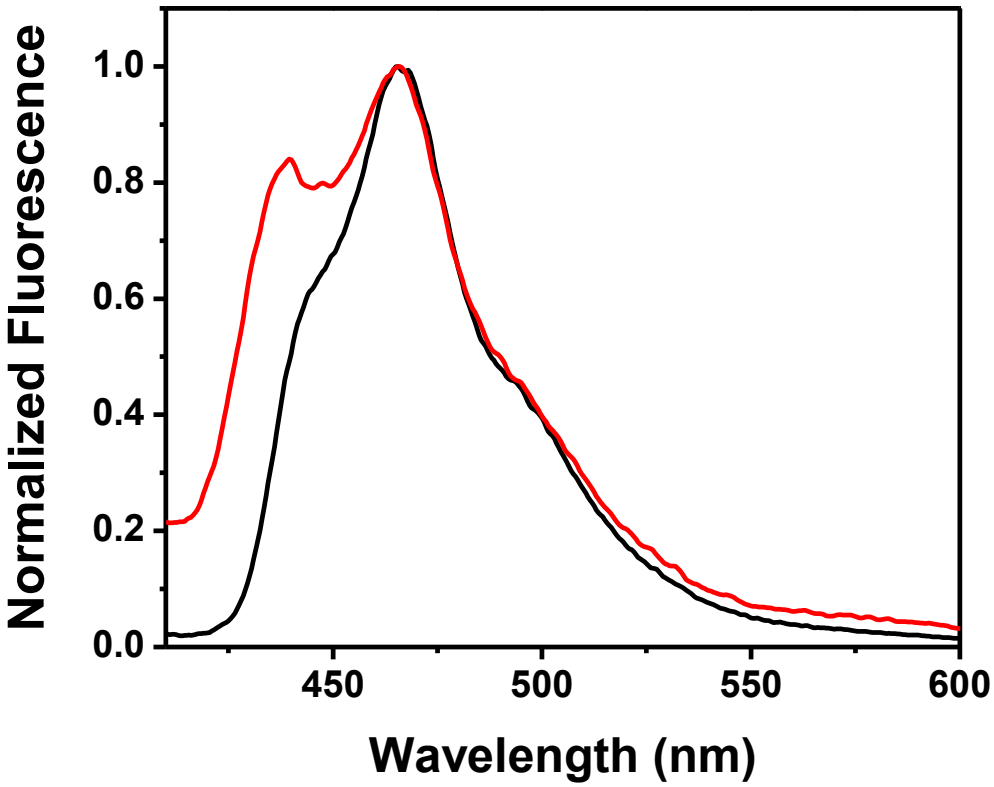

Figure 3.16 Fluorescence spectra of **D4** drop-casting on a glass surface modified with trichloro(octadecyl)silane (OTS) before (black) and after (red) solvent vapor annealing. The two spectra are normalized at 465 nm.

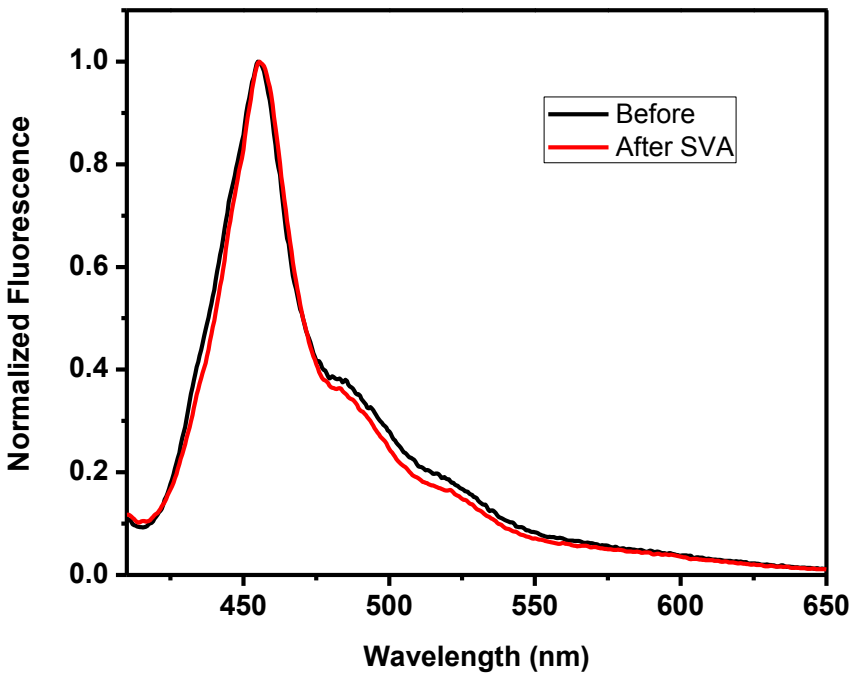

Figure 3.17 Fluorescence spectra recorded on **D3** film deposited on OTS modified glass surface before (black) and after (red) solvent vapor annealing.

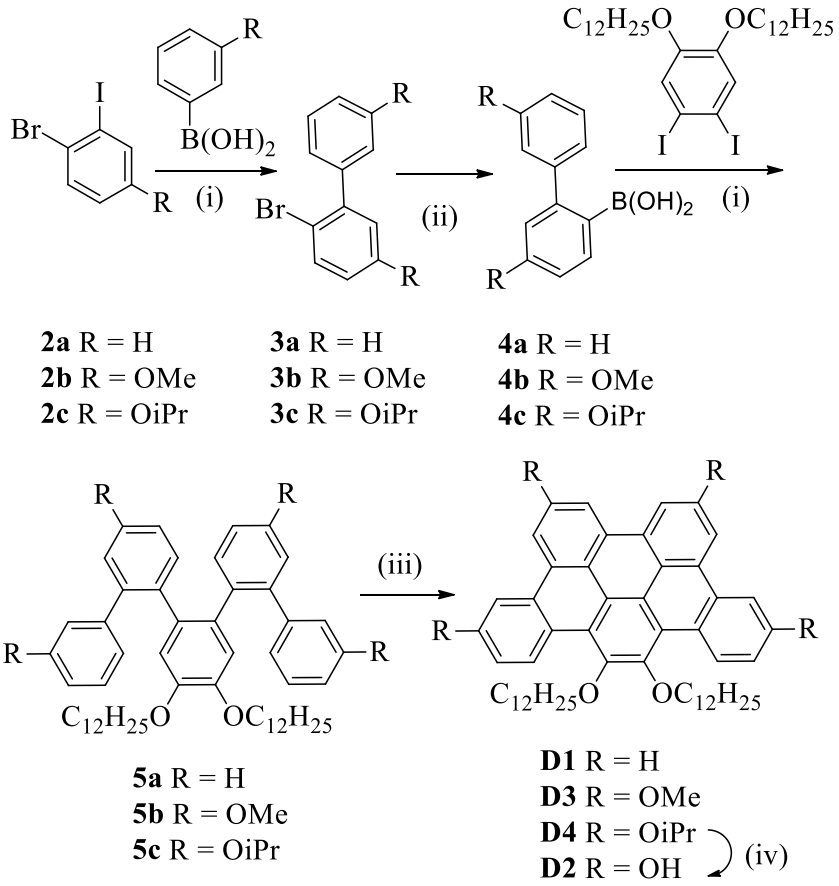

i) $Pd(PPh_3)_4$, Na_2CO_3, Toluene, reflux ; ii) n-BuLi, $B(OCH_3)_3$, THF ; iii) $FeCl_3$, $MeNO_2$, DCM, 0 ^oC; (iv) B-Br-BBN, CH_2Cl_2

Figure 3.18 Synthesis of TBP molecules.

CHAPTER 4

ONE-STEP SURFACE DOPING OF ORGANIC NANOFIBERS TO ACHIEVE HIGH DARK CONDUCTIVITY AND CHEMIRESISTOR SENSING OF AMINES

4.1 Abstract

High dark electrical conductivity was obtained for a p-type organic nanofibril material simply through one-step surface doping. The nanofibril composite thus fabricated has been proven robust under ambient conditions. The high conductivity, combined with the intrinsic large surface area of the nanofibers, enables development of chemiresistor sensors for trace vapor detection of amines, with a detection limit down to sub-ppb range.

4.2 Introduction

Organic semiconductor nanomaterials have gained increasing research interest due to their broad applications in photodetectors [1–5], sensors [6–8], and photovoltaics [9–11]. These materials are superior to their inorganic counterparts regarding synthetic variability, low-temperature and solution processing ability, and the feasibility of fabrication into lightweight, flexible, and low-cost devices [12–14]. However, most organic materials suffer from their intrinsically low charge carrier density and mobility. Current work to improve conductivity has involved blending electron donor (D) and acceptor (A) molecules

into bulk phase heterojunctions, as evidenced in organic photovoltaics. In general these D-A systems provide efficient photoinduced charge separation, although further charge transport is often limited by the intermolecular arrangement disordering and/or mesoscopic grain boundaries [4, 15].

Recently, we have developed a simple approach to fabricate nanofibril D-A heterojunctions, wherein the A molecules were assembled through π-π stacking interaction into nanofibers, and the D component was coated on the nanofiber surface via drop-casting [16]. The strong hydrophobic interdigitation between the side chains of D and A produces an interface that is optimal for photoinduced charge separation. Moreover, the intermolecular π-π stacking along the long axis of nanofiber facilitates the long range charge transport through π-delocalization [17–22]. This continuous charge transport pathway, in combination with the wide D-A interfacial contact intrinsic to the nanofibril structure, makes nanofibril heterojunctions an ideal approach to highly photoconductive organic materials. However, it still remains challenging to achieve high dark conductivity for organic nanomaterials using this simple coating methodology.

In this work, we report on a new nanofibril heterojunction structure that is composed of nanofibers (assembled from a D molecule) coated with a monolayer of A molecule. As shown in Figure 4.1, D is a decyl substituted carbazole-cornered, arylene-ethynylene tetracyclic π-conjugated molecule (DTC) and A is (tridecafluoro-1,1,2,2-tetrahydrooctyl)trichlorosilane (FTS), which has proven to be effective to form a well-defined monolayer on an organic material substrate under ambient conditions [23, 24]. Remarkably, due to the strong redox (charge transfer) interaction between DTC and FTS, the nanofibril junction thus fabricated demonstrated high conductivity even without light

illumination. The high dark conductivity makes this material suitable for applications in chemiresistor sensors for detection of volatile organic compounds (VOCs), particularly amines.

4.3 Results and discussion

In order to achieve uniform coating of FTS molecules onto the nanofibril surface, we used a vapor deposition method (Figure 4.2) that was previously developed by others and successfully employed for coating a monolayer of FTS onto molecular crystals and polymer surfaces through cross-linking of the siloxanes [23, 24]. This vapor transfer approach is particularly suited for surface coating of nanofibril networks, wherein a large number of nanofibers are intertwined and the interstices formed are hard to reach for solvent (due to surface tension) (i.e., difficult to coat through drop-casting). Moreover, the solvent free processing avoids potential damage to the nanofiber (e.g., distortion of the intermolecular arrangement), which often occurs when exposed to certain organic solvents.

In this study, we fabricated nanofibers from the DTC molecules (Figure 4.1) according to the previously developed method [17]. Due to its strong electron donating property, DTC forms a p-type semiconductor as previously evidenced in our lab [25]. Surface doping of DTC nanofibers with electron withdrawing species is expected to enhance the electrical conductivity. Remarkably, the highest occupied molecular orbital (HOMO) of DTC (-4.8 eV) is almost the same as that of rubrene (-4.9 eV) (Figure 4.3). This implies that FTS should act as an effective p-type doping for DTC, as it did for rubrene [23]. The doped charge carrier (here the hole) will transport along the long axis of nanofiber through the intermolecular charge delocalization that is enabled by the stacking interaction [17–22].

This combination of effective surface doping and one-dimensional enhanced charge transport would result in a significant increase in electrical conductivity. Indeed, as shown in Figure 4.4, a more than thousand-fold increase in magnitude was obtained for DTC nanofibers upon surface coating with a FTS thin layer.

To confirm that the observed conductivity increase is due to the p-type doping of FTS, we performed the same experiment with DTC nanofibers but with coating of a unfluorinated silane, n-octadecyltrichlorosilane (OTS, Figure 4.1), which possesses much lower electron affinity than the fluorinated silane. As expected, the electrical conductivity remained almost unchanged upon coating of OTS (Figure 4.4 and Figure 4.5) due to the lack of charge transfer interaction between DTC and OTS. As discussed above, the effective charge transport pathway along the nanofiber also plays a critical role in the conductivity enhancement. To further prove this role, we fabricated a thin film by drop-casting a 15 μM chloroform solution of TDTC (Figure 4.1), an analogue of DTC but with longer alkyl side chains. Although the electron donating capability (HOMO level) remains almost the same for the central tetracycle core, the longer side chains of TDTC are not favorable for columnar π-π stacking under conditions of fast evaporation, thus leading to the formation of film structure that lacks extended intermolecular π-stacking (i.e., a nanofibril morphology). Investigation of this thin film under the same FTS coating showed only a few-fold increase in electrical conductivity (Figure 4.6). The observed low conductivity is consistent with the poor charge transport within the film material. Similar observation was previously obtained on the photoconductivity of TDTC film upon exposure to oxygen under UV irradiation, for which only slight enhancement of photocurrent was obtained [25]. In contrast, the nanofibers of TDTC (fabricated through

solution-based self-assembly) demonstrated three orders of magnitude increase in photocurrent under the same measurement conditions.

In order to further characterize the surface morphology of the DTC nanofibers before and after FTS coating, Atomic Force Microscopy (AFM) was used to image the nanofibril network deposited on the SiO_2 substrate (Figure 4.7). Both the size and morphology of the nanofibers are consistent with the electronic microscopy imaging performed previously on the same nanofibers [26]. Vapor deposition of the FTS monolayer did not cause any morphology change of the nanofibril structure, indicating that the surface modification is noninvasive to the intermolecular arrangement within the nanofibers. As clearly shown in Figure 4.7 (d), the vapor transfer of FTS allowed for interstitial diffusion throughout the nanofibril network and surface deposition onto the bare SiO_2 substrate. Separate investigations proved the effective surface deposition of FTS onto the SiO_2 substrate. Such full surface coverage of FTS (on both nanofibers and SiO_2 substrate in between) turned the whole sample surface highly hydrophobic, with a contact angle as large as 136° (Figure 4.8). A highly hydrophobic surface prevents the condensation of humidity, thus helping increasing the robustness of the nanofibril materials. Previously, water was found to be detrimental to the electrical conductivity of conducting polymers modified with FTS, causing a more than 50% decrease in conductivity when exposed to saturated water vapour [24]. In contrast, the FTS-modified DTC nanofibers are sustainable even under saturated water vapor (23,000 ppm) at room temperature (Figure 4.9). This water resistance is conducive to development of the nanofibers into ambient sensors.

When deposited on a substrate, the nanofibers form an intertwined network, possessing porosity on a number of length scales depending on the density of nanofibers. The mesh-

like porosity not only provides increased surface area for enhanced analyte adsorption, but also expedites the diffusion of guest molecules across the film matrix, leading to efficient air sampling of VOCs [17]. Since the surface modification of FTS does not change the global morphology of DTC nanofibers, we expected that the FTS-modified DTC nanofibers still possess the large porosity and wide interface as the bare nanofibers, which were previously proven efficient for trace vapor sensing of explosives through fluorescence quenching [26, 27]. The high dark conductivity obtained here for the FTS-modified DTC nanofibers would ease the use of these nanofibers directly as chemiresistor sensors, for which the high electrical current is conducive to the enhancement of signal-to-noise ratio. Compared to fluorescence sensors, which demand installation and alignment of both the excitation light source and photon detector, the chemiresistor sensor simply relies on electrical current modulation that can be performed with a micron-sized electrode pair, thereby facilitating miniaturization of the whole sensor system. Unfortunately, most of the organic nanofiber chemiresistor sensors reported thus far still suffer from the low current, which causes hard to control fluctuation under ambient conditions due to the effect of oxygen [6, 25].

Figure 4.10 shows the electrical current measured over the FTS-modified DTC nanofibers in response to the diluted vapor of aniline. Aniline, with saturated vapor pressure of 880 ppm under ambient condition, represents one of the common organic amines that have been widely used in various industries. Successive exposure to 80 ppb aniline vapor resulted in a significant decrease in current. By measuring the current decrease under varying vapor concentrations of aniline and fitting the data with the Langmuir adsorption model, we can project the detection limit for aniline vapor down to

0.38 ppb, for which we set the detectable current change as three times the standard deviation of the current measurement (1 nA) under our experimental condition. This detection limit is about six orders of magnitude lower than the saturated vapor of aniline. Such high sensitivity of VOC detection is quite rare for chemiresistor based sensors. The high sensing sensitivity obtained for FTS-modified DTC nanofibers is largely due to the three-dimensional mesh network formed by the nanofibers in combination with the strong interfacial interaction between aniline and the nanofiber. While the former enhances the vapor sampling, the latter produces effective charge depletion from the nanofiber. The strong surface adsorption of aniline is also consistent with the fast sensor response as observed (i.e., as shown in Figure 4.10, Figure 4.11, and Figure 4.12), and the current decreases in the time scale of 2.8 sec upon exposure to aniline vapor.

Though the detailed chemistry of the surface adsorption of aniline is not completely clear, it is most likely that aniline binds directly with FTS through charge transfer interaction, considering the strong electron donating capability of aniline, with HOMO of -5.6 eV [28]. The binding of aniline thereby decreases the electron affinity of FTS, which in turn weakens the charge separation with DTC. The overall result is that binding of aniline depletes the charge carriers (holes) of DTC nanofiber. The strong binding of aniline within the nanofibril network is also consistent with the fact that no sensor recovery was observed after removal of aniline vapor. Moreover, the nanofibril composite sensor also demonstrates high selectivity for amines by giving no response to other common organic solvents and reagents as shown in Figure 4.11. The same FTS- modified DTC nanofibers were also tested for vapor sensing against other organic amines (Table 4.1) following the same procedure as employed in Figure 4.10. Similar to the response to aniline, the

nanofibers demonstrated significant conductivity modulation upon exposure to the diluted vapor of both aliphatic and aromatic amines (Table 4.1), indicating that the reported nanofiber composite functions as a general amine sensor, in the similar manner as the inorganic n-type semiconductor chemiresistors.

4.4 Conclusion

High dark electrical conductivity was obtained for a p-type organic nanofibril material simply through a one-step surface coating (doping) of electron withdrawing molecules. The nanofibril composite thus fabricated has been proven robust under ambient conditions. The high conductivity, combined with the intrinsic large surface area of nanofibers, enables the development of chemiresistor sensors for trace vapor detection of amines, with detection limits down to the sub-ppb range. The reported work represents a simple approach to the fabrication of highly conductive nanofibril materials, which may find broad application in sensors and other electronic systems.

4.5 Experimenal section

4.5.1 Materials

All solvents and reagents were purchased from Sigma-Aldrich and used without purification. Synthesis and purification of DTC and TDTC macrocyclic molecules followed the previously published methods and procedures [29, 30].

4.5.2 Fabrication of nanofibers and devices

Fabrication of nanofibers: 0.5 mL of 15 μM chloroform solution of DTC was injected rapidly into 5 mL ethanol in a test tube. Nanofibers were produced immediately through precipitation driven self-assembly. The suspension was then aged in the refrigerator for 24 hours to achieve more uniform nanofibers. The nanofibers thus generated can be transferred onto the surface by the drop-casting method. Typically, after removing the excess solvent in the nanofiber suspension, 0.2 mL of such suspension was drop-casted onto a 5 mm × 5 mm glass substrate, followed by fast solvent evaporation in fume hood under ambient condition. The glass slide was first cleaned in acetone and isopropanol for 3 min each in an ultrasonic bath and then cleaned with a piranha solution (70 vol% H_2SO_4: 30 vol% 30% H_2O_2) for 20 min, followed by rinsing with deionized water and drying in air flow. The glass supported nanofibers thus made are suited for microscopy, optical, and contact angle measurements.

Preparation of thin-film of TDTC: 0.5 mL of 15 μM chloroform solution of TDTC was drop-casted onto a 5 mm × 5 mm silicon wafer covered with 300-nm thick SiO_2, followed by fast solvent evaporation in fume hood.

Surface coating of FTS was performed using a vapor deposition procedure (Figure 4.2) that was previously developed by others [23]. Briefly, the nanofibers predeposited on a substrate were placed in a vacuum chamber (volume ~25 cm^3); a small container (volume ~5 cm^3) with a few drops of FTS were placed in a different chamber separate from the vacuum chamber by a three-way valve that was connected with a membrane pump (BUCHI V500P). The vacuum chamber was evacuated first to reach the maximal vacuum level. Then, the FTS chamber was connected to the vacuum chamber through the three-way valve

to start the vapor diffusion of FTS. The vapor deposition process was completed in about 5 hours.

Single pair electrodes were fabricated on a highly doped p-type silicon wafer covered with 300-nm-thick thermal oxide film. Using the traditional photolithography and lift-off approach, 30-nm thick Au/Cr electrode pairs were patterned on the wafer with a gap of 5 μm in width and 10 μm in length. Onto the electrode-pair thus fabricated, the nanofibers can be deposited by drop-casting, the same procedure as described above for the deposition on glass substrate. This small volume drop-casting method produced devices that demonstrated quite good reproducibility (i.e., only slight variation in electrical current was observed between the different batches of devices) (Figure 4.5).

4.5.3 Materials characterization

Contact angle measurement was performed with a Dataphysics OCA15EC instrument. A water droplet with a volume between 1 to 3 μL was placed on the sample surface, followed by immediate image capturing to measure the static contact angle. Atomic Force Microscopy (AFM) measurements were carried out on SiO_2 substrates, which were cleaned with acetone.

The electrical conductivity (chemiresistor) properties of nanofibers were characterized under ambient conditions using a Signatone S-1160 Probe Station combined with an Agilent 4156C Precision Semiconductor Parameter Analyzer. The probe station was equipped with a Motic Microscope for positioning and a CCD camera for insitu imaging of the device. The current-time (I-V) curves were measured with a bias voltage of 30 V between the electrodes. The sensor testing experiments were conducted by injecting 5 mL

of vapor containing different concentrations of amine over the nanofibers. Diluted aniline vapor was obtained by mixing concentrated vapor with the appropriate volume of clean air in a sealed container. The concentration of the diluted vapor was determined by the volume ratio of the concentrated vapor and air. Within the experimental vapor pressure range, this dilution method was proven effective for adjusting the aniline concentration [25].

4.5.4 Langmuir fitting of the current change versus vapor concentration of aniline

As shown in Figure 4.13, we can get the current change ($\Delta I = I_0 - I$) from the current (I) versus time (s) curve. This method considers the slow drifting of the baseline. The data presented in this plot are from Figure 4.11 upon exposure to 8 ppm aniline. Using the same method, we can get the ΔI values for the case of exposure to 880 ppm (Figure 4.12) and 80 ppb (Figure 4.10), and the results are summarized in Table 4.2.

Assuming an equilibrium was reached upon exposure to aniline vapor (which is reasonable considering the strong surface binding of aniline), the data shown in Table 4.2 should follow the Langmuir adsorption model. First, the surface adsorption of aniline (i.e., surface density, *X*) is related to the vapor pressure of aniline as described by the Langmuir Equation (4.1),

$$X = \frac{k \cdot [\text{aniline}]}{1 + k \cdot [\text{aniline}]} \tag{4.1}$$

where k is a constant, and [aniline] is the vapor pressure (concentration) of aniline.

The decrease in electrical current is proportional to the surface density of aniline molecules. Then, we have

$$\Delta I/I_0 = \frac{a \cdot k \cdot [\text{aniline}]}{1 + k \cdot [\text{aniline}]} \tag{4.2}$$

where a is a proportional constant.

Fitting this equation with all the four data points in the table above gives the plot shown in Figure 4.14.

However, considering the fact that the sensor was likely saturated under high vapor pressure of aniline (880 ppm, see Figure 4.12), which led to close to 100% decrease in current, we decided to fit the three data points in low vapor concentration range (as shown in Figure 4.15), which gives a = 0.35, k = 23 with $R^2 = 1$.

The standard derivation of the electrical current measurements under vapor pressure of 80 ppb (Figure 4.10), 8 ppm (Figure 4.11), and 880 ppm (Figure 4.12) was (on average) about 1 nA. If we set the threshold of detectable current change at a value three times the standard derivation, that is ΔI = 3 nA, the corresponding detection limit can be determined by using the above fitting (by setting I_0 at a regular level of 1000 nA). This gives a detection limit of aniline vapor at 0.38 ppb.

4.6 References

[1] Weiss, D. S.; Abkowitz, M. *Chem. Rev.* **2009**, *110*, 479–526.

[2] Gong, X.; Tong, M.; Xia, Y.; Cai, W.; Moon, J. S.; Cao, Y.; Yu, G.; Shieh, C. L.; Nilsson, B.; Heeger, A. J. *Science* **2009**, *325*, 1665–1667.

[3] Konstantatos, G.; Sargent, E. H. *Nat. Nanotechnol.* **2010**, *5*, 391–400.

[4] Yamamoto, Y.; Fukushima, T.; Suna, Y.; Ishii, N.; Saeki, A.; Seki, S.; Tagawa, S.; Taniguchi, M.; Kawai, T.; Aida, T. *Science* **2006**, *314*, 1761–1764.

[5] Zhu, H.; Li, T.; Zhang, Y.; Dong, H.; Song, J.; Zhao, H.; Wei, Z.; Xu, W.; Hu, W.; Bo, Z. *Adv. Mater.* **2010**, *22*, 1645–1648.

[6] Che, Y.; Yang, X.; Liu, G.; Yu, C.; Ji, H.; Zuo, J.; Zhao, J.; Zang, L. *J. Am. Chem. Soc.* **2010**, *132*, 5743–5750.

[7] de la Escosura, A.; Janssen, P. G. A.; Schenning, A. P. H. J.; Nolte, R. J. M.; Cornelissen, J. J. L. M. *Angew. Chem. Int. Ed.* **2010**, *49*, 5335–5338.

[8] Zhang, X.; Jie, J.; Zhang, W.; Zhang, C.; Luo, L.; He, Z.; Zhang, X.; Zhang, W.; Lee, C.; Lee, S. *Adv. Mater.* **2008**, *20*, 2427–2432.

[9] Yamamoto, Y.; Zhang, G.; Jin, W.; Fukushima, T.; Ishii, N.; Saeki, A.; Seki, S.; Tagawa, S.; Minari, T.; Tsukagoshi, K.; Aida, T. *Proc. Natl. Acad. Sci.* **2009**, *106*, 21051–21056.

[10] Charvet, R.; Acharya, S.; Hill, J. P.; Akada, M.; Liao, M.; Seki, S.; Honsho, Y.; Saeki, A.; Ariga, K. *J. Am. Chem. Soc.* **2009**, *131*, 18030–18031.

[11] Clarke, T. M.; Durrant, J. R. *Chem. Rev.* **2010**, *110*, 6736–6767.

[12] Günes, S.; Neugebauer, H.; Sariciftci, N. S. *Chem. Rev.* **2007**, *107*, 1324–1338.

[13] Placencia, D.; Wang, W.; Shallcross, R. C.; Nebesny, K. W.; Brumbach, M.; Armstrong, N. R. *Adv. Funct. Mater.* **2009**, *19*, 1913–1921.

[14] Yang, F.; Shtein, M.; Forrest, S. R. *Nat. Mater.* **2005**, *4*, 37–41.

[15] Neuteboom, E. E.; Meskers, S. C. J.; van Hal, P. A.; van Duren, J. K. J.; Meijer, E. W.; Janssen, R. A. J.; Dupin, H.; Pourtois, G.; Cornil, J.; Lazzaroni, R.; Brédas, J.-L.; Beljonne, D. *J. Am. Chem. Soc.* **2003**, *125*, 8625–8638.

[16] Che, Y.; Huang, H.; Xu, M.; Zhang, C.; Bunes, B. R.; Yang, X.; Zang, L. *J. Am. Chem. Soc.* **2011**, *133*, 1087–1091.

[17] Zang, L.; Che, Y.; Moore, J. S. *Acc. Chem. Res.* **2008**, *41*, 1596–1608.

[18] Coropceanu, V.; Cornil, J.; da Silva Filho, D. A.; Olivier, Y.; Silbey, R.; Brédas, J.-L. *Chem. Rev.* **2007**, *107*, 926–952.

[19] Che, Y.; Datar, A.; Yang, X.; Naddo, T.; Zhao, J.; Zang, L. *J. Am. Chem. Soc.* **2007**, *129*, 6354–6355.

[20] Sofos, M.; Goldberger, J.; Stone, D. A.; Allen, J. E.; Ma, Q.; Herman, D. J.; Tsai, W.-W.; Lauhon, L. J.; Stupp, S. I. *Nat. Mater.* **2009**, *8*, 68–75.

[21] Delgado, M. C. R.; Kim, E.-G.; Filho, D. t. A. d. S.; Bredas, J.-L. *J. Am. Chem. Soc.* **2010**, *132*, 3375–3387.

[22] Messmore, B. W.; Hulvat, J. F.; Sone, E. D.; Stupp, S. I. *J. Am. Chem. Soc.* **2004**, *126*, 14452–14458.

[23] Calhoun, M. F.; Sanchez, J.; Olaya, D.; Gershenson, M. E.; Podzorov, V. *Nat. Mater.* **2008**, *7*, 84–89.

[24] Kao, C. Y.; Lee, B.; Wielunski, L. S.; Heeney, M.; McCulloch, I.; Garfunkel, E.; Feldman, L. C.; Podzorov, V. *Adv. Funct. Mater.* **2009**, *19*, 1906–1911.

[25] Che, Y.; Yang, X.; Zhang, Z.; Zuo, J.; Moore, J. S.; Zang, L. *Chem. Commun.* **2010**, *46*, 4127–4129.

[26] Che, Y.; Gross, D. E.; Huang, H.; Yang, D.; Yang, X.; Discekici, E.; Xue, Z.; Zhao, H.; Moore, J. S.; Zang, L. *J. Am. Chem. Soc.* **2012**, *134*, 4978–4982.

[27] Naddo, T.; Che, Y.; Zhang, W.; Balakrishnan, K.; Yang, X.; Yen, M.; Zhao, J.; Moore, J. S.; Zang, L. *J. Am. Chem. Soc.* **2007**, *129*, 6978–6979.

[28] Che, Y.; Yang, X.; Loser, S.; Zang, L. *Nano Lett.* **2008**, *8*, 2219–2223.

[29] Zhang, W.; Moore, J. S. *J. Am. Chem. Soc.* **2004**, *126*, 12796–12796.

[30] Gross, D. E.; Moore, J. S. *Macromolecules* **2011**, *44*, 3685–3687.

[31] Kobayashi, S.; Nishikawa, T.; Takenobu, T.; Mori, S.; Shimoda, T.; Mitani, T.; Shimotani, H.; Yoshimoto, N.; Ogawa, S.; Iwasa, Y. *Nat. Mater.* **2004**, *3*, 317–322.

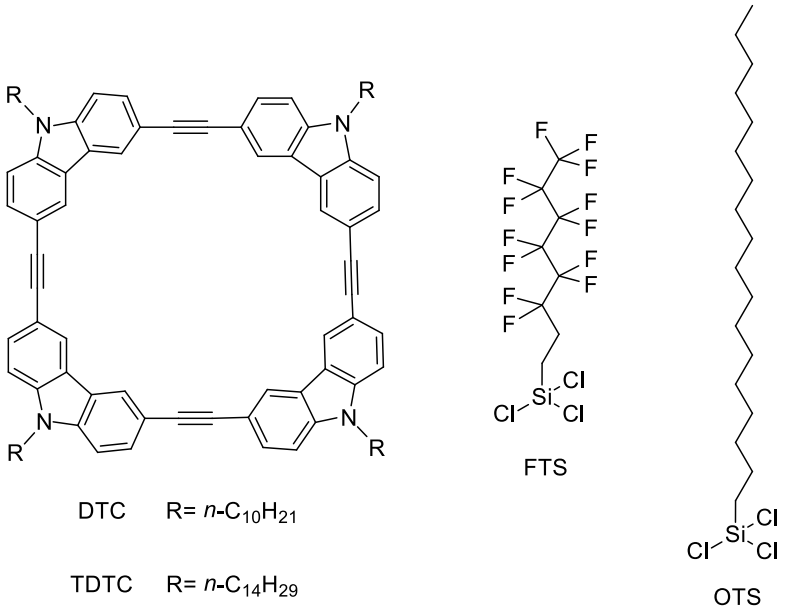

Figure 4.1 Molecular structures of DTC, TDTC, FTS and OTS.

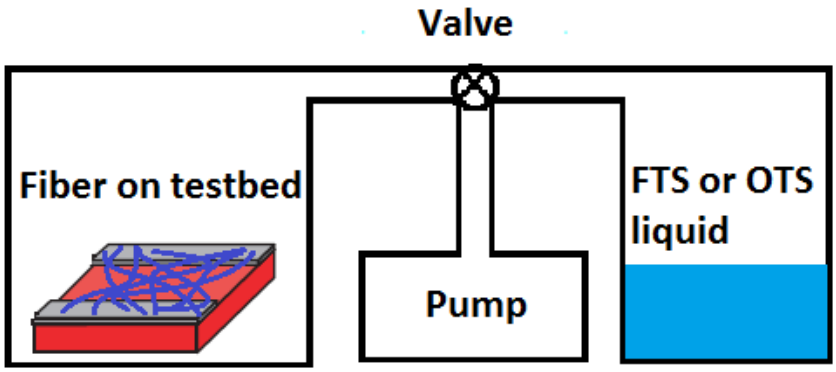

Figure 4.2 Diagram of the vapor deposition setup.

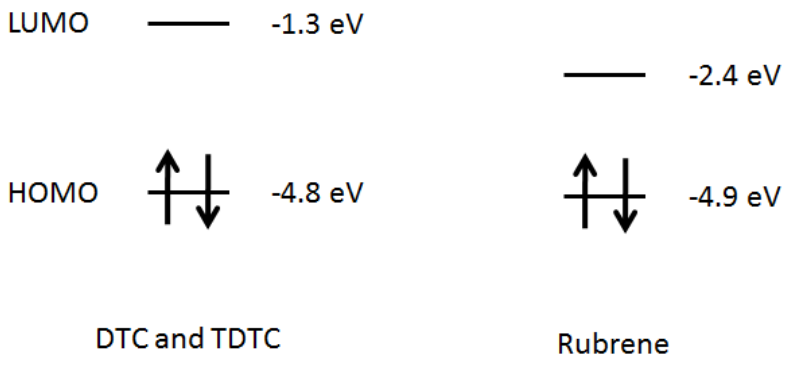

Figure 4.3 Molecular orbital energy levels of DTC, TDTC, and rubrene. Geometry optimization and energy calculations were performed with density-functional theory (B3LYP/6-311g**//B3LYP/6-31g*) using Gaussian 09 package. The direct electron transfer between the rubrene and FTS molecules has been proven in the previous literature with electron spin resonance experiments [23]. Since the HOMO levels of DTC are even slightly higher than rubrene, the direct electron transfer between DTC and FTS molecules is thus expected.

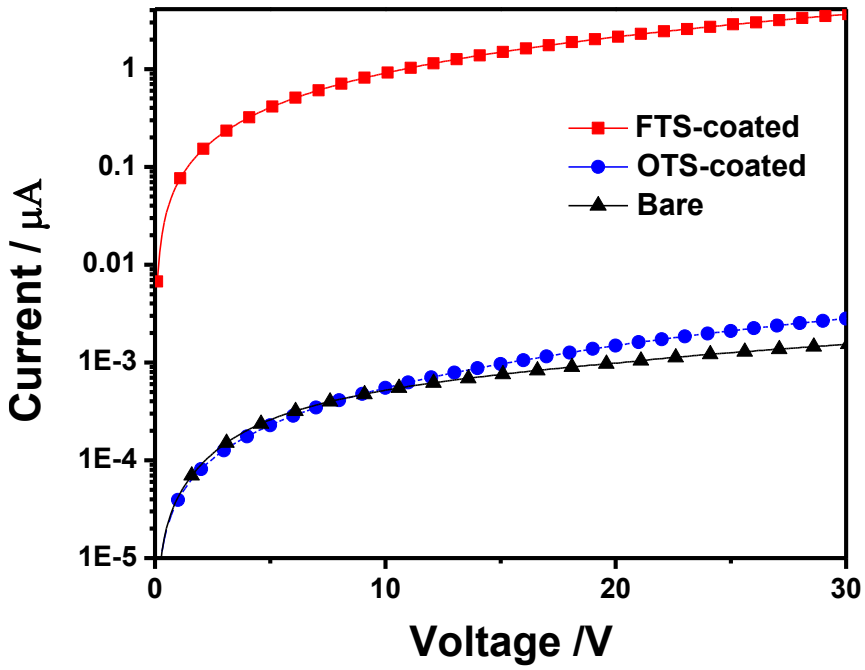

Figure 4.4 Current-Voltage curve for bare, OTS, and FTS-coated DTC nanofibers. Nanofibers were deposited on a gold electrode pair with a gap of 5 μm and width of 10 μm.

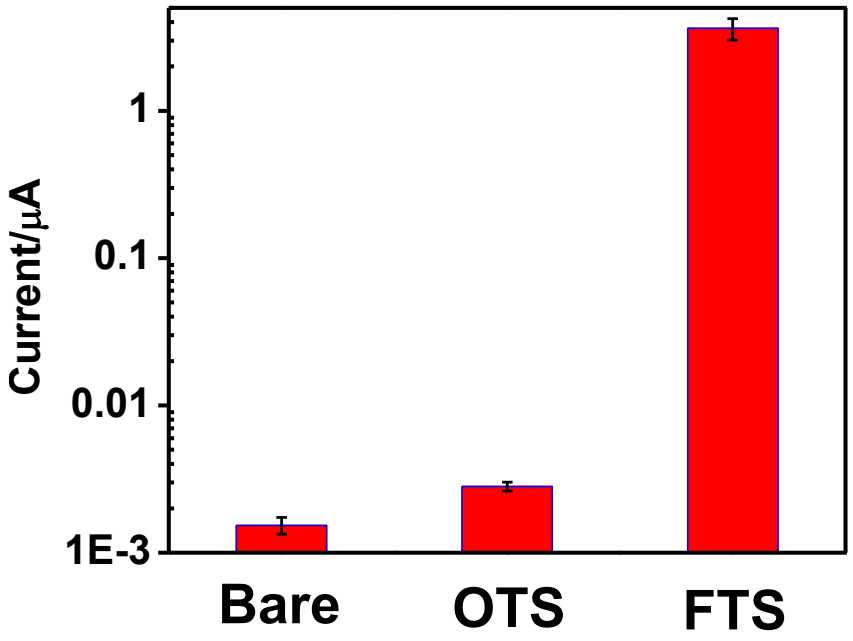

Figure 4.5 Comparison of the conductivity of bare, OTS, and FTS-coated DTC nanofibers. The nanofibers were deposited onto the same electrodes as in Figure 4.4 using the same drop-casting method as described in the Experimental Section. For each case the nanofibers were deposited onto 3–5 electrodes and measured for the I-V curve as shown in Figure 4.4; the electrical current value measured under a bias voltage of 30 V was used for the conductivity comparison shown in this plot, for which the small error bar reflects the slight variation between different devices thus fabricated.

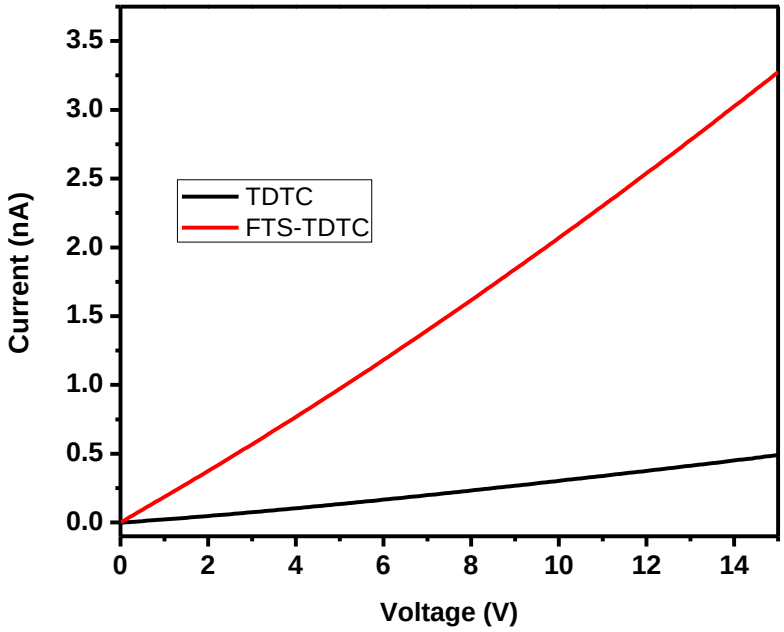

Figure 4.6 Current-Voltage curves for bare TDTC film and FTS-coated TDTC film. Thin films were deposited on a gold electrode pair with a gap of 5 μm and width of 10 μm. The conductivity of FTS-coated TDTC film showed only a few-fold increase compared with the pristine TDTC film.

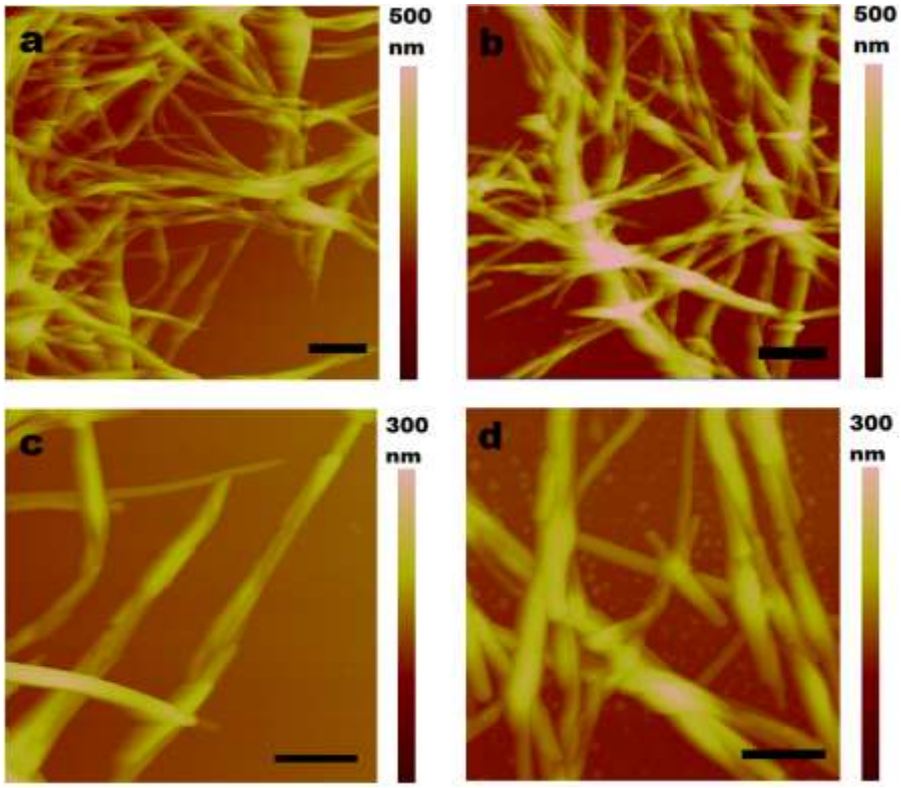

Figure 4.7 AFM images of DTC fibers before (a, c) and after (b, d) FTS coating. The scale bars are 500 nm (a, b) and 200 nm (c, d), respectively.

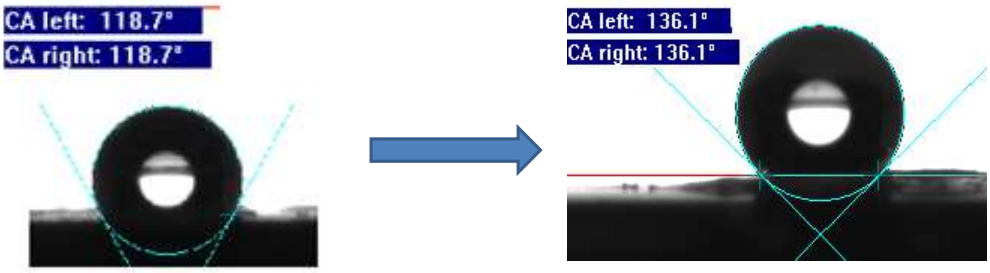

Original DTC fiber surface

FTS coated DTC fiber surface

Figure 4.8 Contact angle measurement of pristine and FTS-modified DTC nanofibers. FTS treatment increased the contact angle from 118° to 136°.

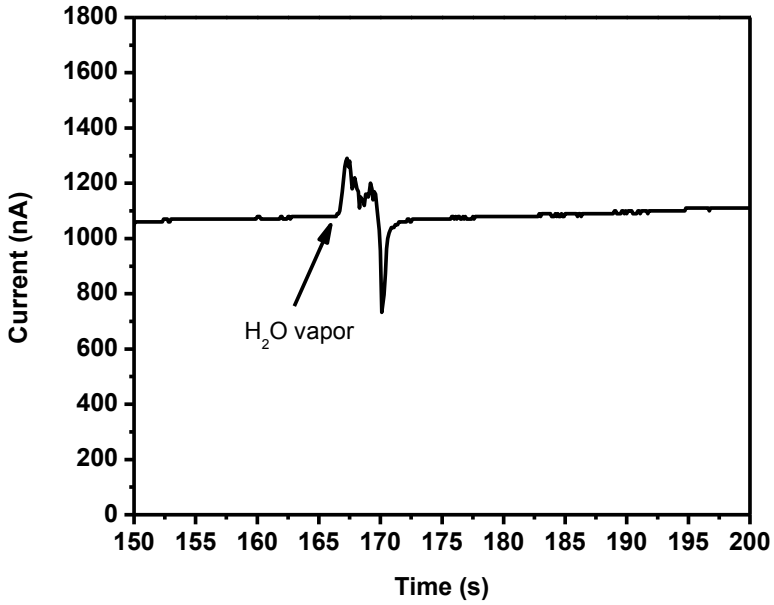

Figure 4.9 Electrical current measured over the FTS-modified DTC nanofibers upon exposure to saturated water vapour (23000 ppm). Nanofibers were deposited on the same electrodes with a gap of 5 μm and width of 10 μm and measured under 30 V bias. As observed for the organic solvent vapor, exposure to high concentration water vapor causes a spike-like fluctuation of electrical current due to some nonspecific interfacial interaction, though the signal fluctuation was very fast (only 5 seconds) and completely reversible, which can be easily distinct from the response to aniline and other amines vapor.

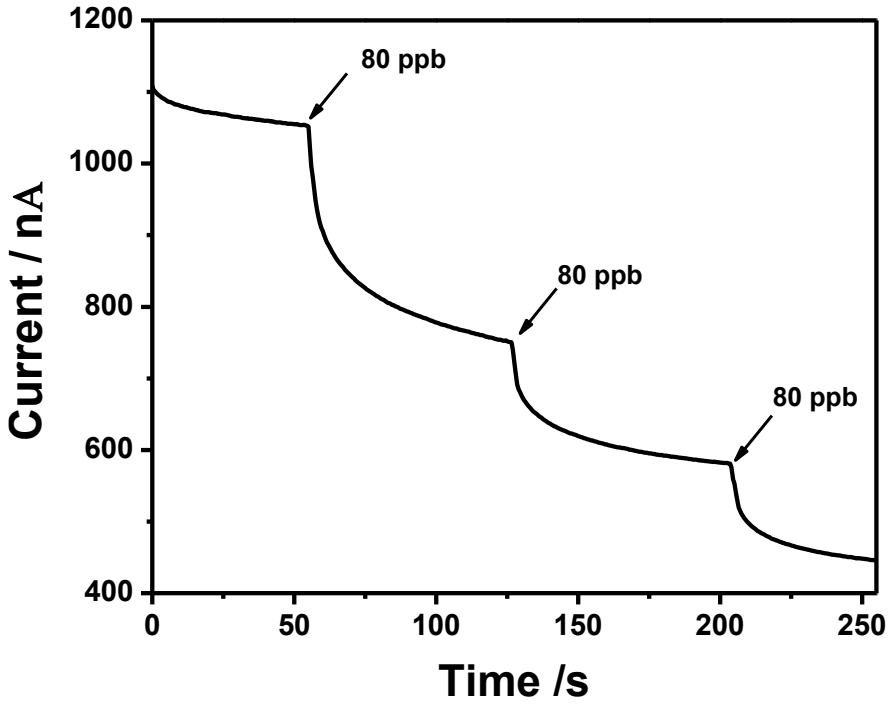

Figure 4.10 Electrical current measured over the FTS-modified DTC nanofibers upon successive exposure to 80 ppb aniline vapor. Nanofibers were deposited on the same electrodes as in Figure 4.4 and measured under 30 V bias.

Figure 4.11 Selectivity test of FTS-modified DTC nanofibers sensor. Electrical current measured over the FTS-modified DTC nanofibers upon successive exposure to aniline and common organic solvent vapors (a): (1) air flow, (2) 410 ppm acetone, (3) 350 ppm chloroform, (4) 75 ppm toluene, (5) 350 ppm THF, (6) 150 ppm ethanol, (7) 260 ppm hexane, (8) 140 ppm nitromethane, and (9) 8 ppm aniline. The spike signals caused by acetone, chloroform, and THF are likely due to the nonspecific solvent effect (e.g., surface desorption of oxygen, commonly observed for other nanomaterial sensors), though this quick, reversible response (in time range of only 0.6 sec (b)) can be easily distinguished from the response of amines. The rapid recovery of the spike signal caused by the solvent vapor is consistent with the weak, nonspecific physical adsorption of the solvent molecules on the nanofiber, which can be desorbed quickly upon reexposure to clean air. In comparison, the electrical current response to aniline vapor was almost irreversible in the time course of experiment, which is apparently due to the strong binding between amine and the nanofiber.

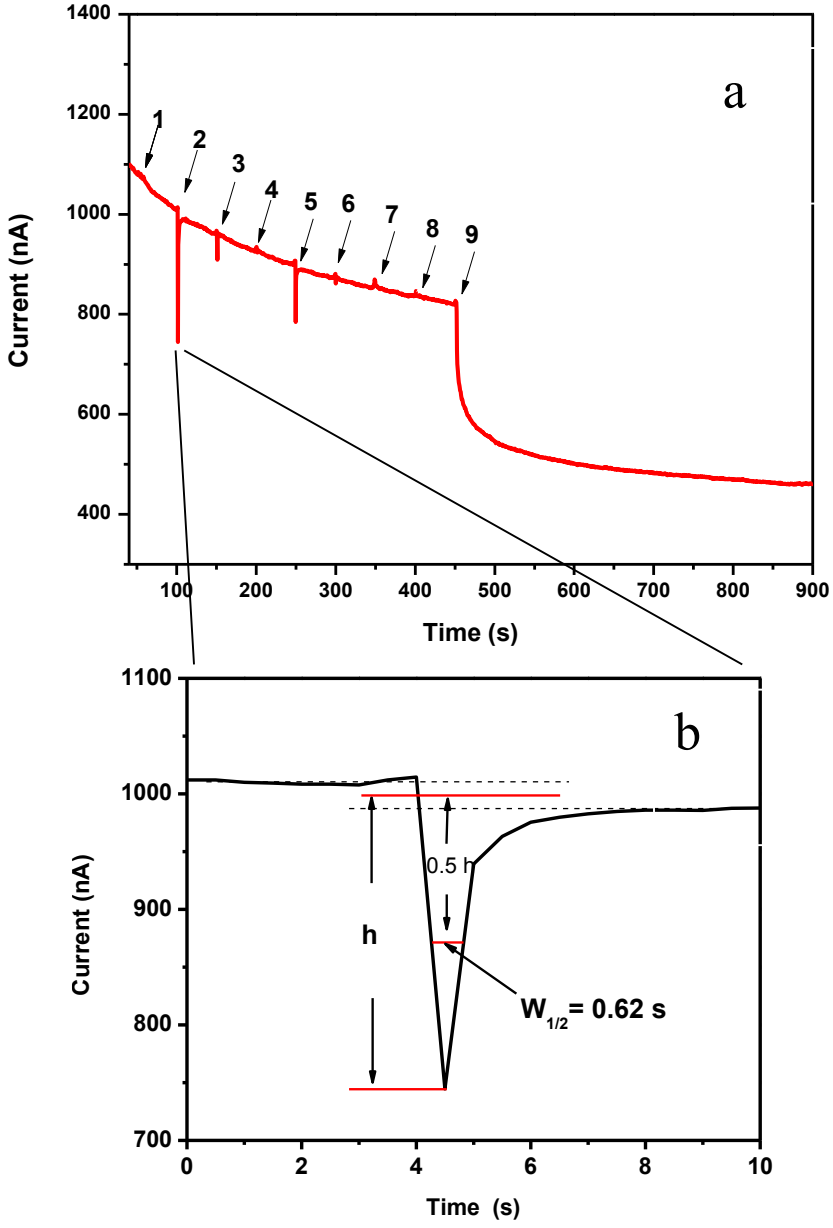
a
1
2
3
4
5
6
7
8
9
Current (nA)
Time (s)
b
0.5 h
h
W1/2= 0.62 s
Current (nA)
Time (s)

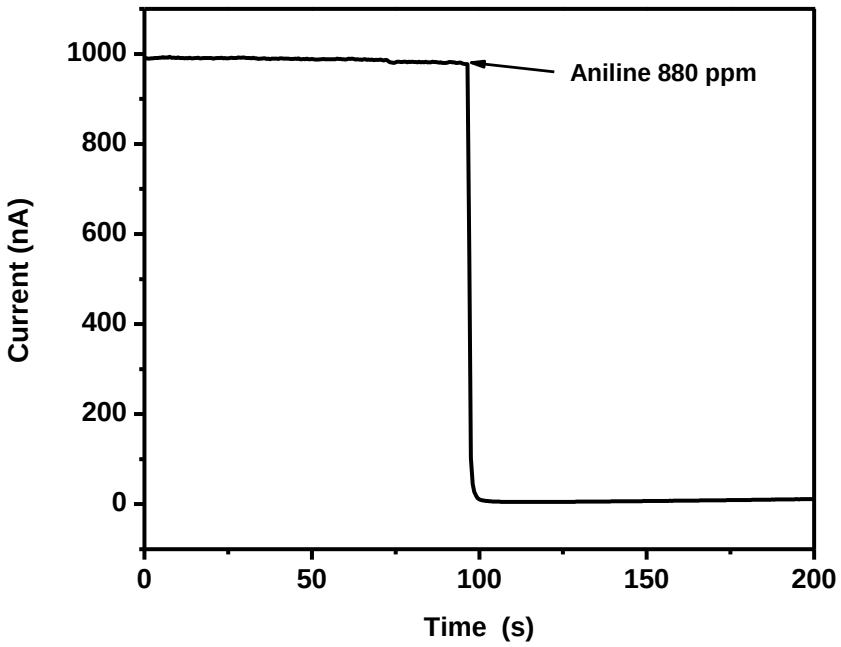

Figure 4.12 Electrical current measured over the FTS-modified DTC nanofibers upon exposure to the saturated vapor of aniline under ambient condition (880 ppm). Nanofibers were deposited on the electrodes with a gap of 5 μm and width of 10 μm and measured under 30 V bias. Under this high vapor pressure, the electrical current was apparently decreased to zero level, indicating that the sensor was saturated with the aniline vapor.

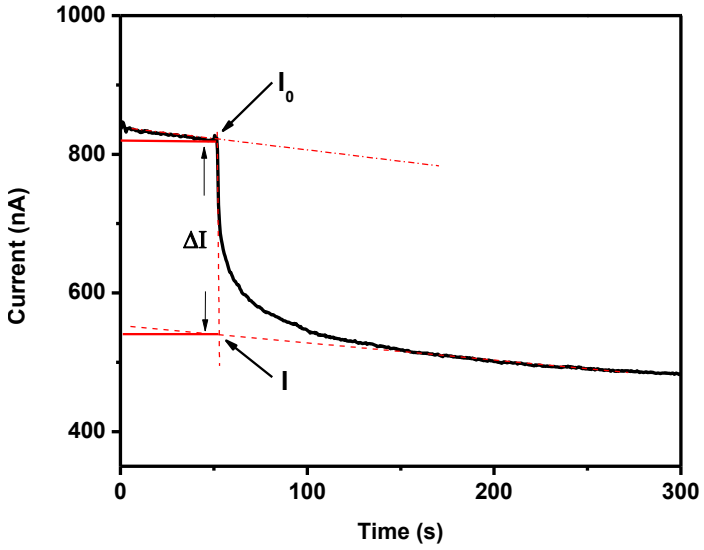

Figure 4.13 A plot showing how to get the current change ($\Delta I = I_0 - I$) from the current versus time curve.

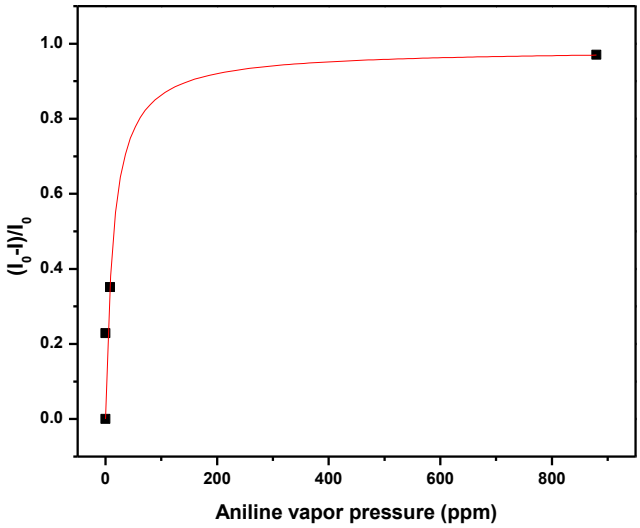

Figure 4.14 The Langmuir fitting between current change and analyst concentration.

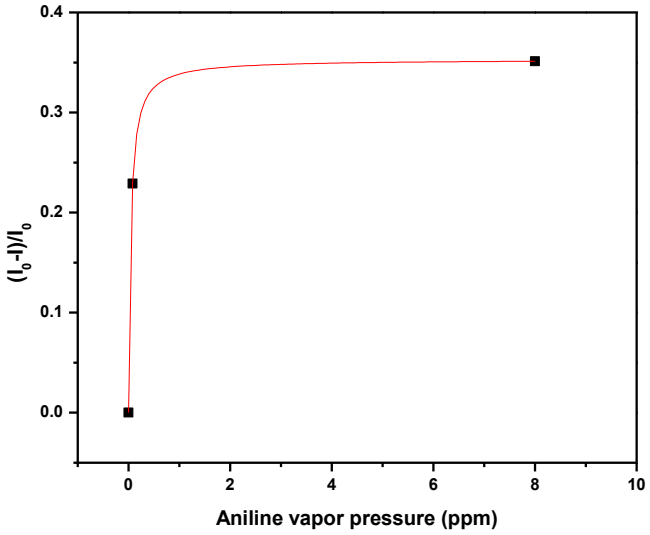

Figure 4.15 Modified Langmuir fitting between current change and analyst concentration.

Table 4.1 Comparative sensing tests against the vapor of varying organic amines.

Amine type	Names	Vapor pressure	Conductivity change
Aliphatic	Dodecylamine	18.4 ppm	-25%
	Trihexylamine	7.5 ppm	-10%
Aromatic	Triphenylamine	455 ppb	-60%
	2,4,6-Tri-tert-butylaniline	65 ppb	-30%
	4-Aminobiphenyl	1.1 ppm	-30%
	4-Dodecylaniline	200 ppb	-25%
	aniline	80 ppb	-25%

Each amine was tested on a freshly made new device. Similar to the response to aniline, the nanofibers demonstrate significant conductivity modulation upon one-time exposure to diluted vapor of both aliphatic and aromatic amines, indicating that the reported nanofiber composite functions as a general amine sensor, in the similar manner as n-type semiconductor chemiresistors.

Table 4.2 Current change vs. vapor concentration of aniline at different concentration.

vapor pressure of aniline	Relative current change observed $((I_0 - I) / I_0)$
0	0
0.08	0.23
8	0.35
880	0.97 (close to 100%, sensor likely saturated)

CHAPTER 5

DIRECT SYNTHESIS OF HIGHLY PURE PERYLENE TETRACARBOXYLIC MONOIMIDE

5.1 Abstract

A series of perylene tetracarboxylic monoimides substituted with cycloalkanes were synthesized through a one-step reaction between cycloalkyl amines and the parent perylene dianhydride. The reaction demonstrates high selectivity for the production of monoimides with no formation of diimides. The high reaction selectivity is primarily due to the insolubility of the monoimides in the reaction medium, which in turn causes rapid precipitation of the products, shifting the reaction equilibrium to the right.

5.2 Introduction

Perylene tetracarboxylic diimides (PTCDIs) represent a robust class of n-type organic semiconductor with high thermal- and photostability and have long been used in various optoelectronic materials and devices [1–4]. As evidenced in recent research, appropriate side-chain modification of PTCDIs facilitates one-dimensional (1D) cofacial stacking of the molecules, leading to formation of well-defined nanowires or nanobelts [4–7]. Compared to the traditional bulk-phase materials, these 1D nanostructures often demonstrate unique properties and unprecedented performance, such as 1D confined

Reprinted with permission from Tetrahedron Letters, 2010, 51, 6651–6653.

charge transport [8–10], linear emission polarization [11, 12], and 1D enhanced exciton migration and the resulted amplification of emission quenching [13, 14]. Combination of these optoelectronic properties enables applications in vapor sensing of gaseous reagents through modulation of the emission intensity or electrical conductivity of the nanofibers [4, 15].

The synthesis of PTCDIs takes advantages of the fact that the two nitrogen positions at the imides of PTCDI are nodes in the π-orbital wavefunction [16], providing enormous options for modifying the structures of the two side-chains (but without significant altering of the electronic property of the PTCDI skeleton). To construct supramolecular structures of PTCDI containing multifunctional moieties (e.g., electron donor for charge separation, hydrophilic side-chain for enhanced layer-by-layer stacking), it is often demanded to make the monoimide as a precursor so as to synthesize the asymmetric PTCDIs with two different side-chain substitutions (Figure 5.1). However, most of the monoimides have thus far been synthesized through partial hydrolysis of the symmetric PTCDI [17, 18], followed by extensive column purification (which could be extremely time-consuming and costly if the solubility of imides is limited). This prevents large scale production of the asymmetric PTCDIs for the necessary materials fabrication. To overcome this bottleneck, it is critical to develop a synthetic protocol that allows for direct preparation of monoimides from the parent dianhydride compound (Figure 5.1).

Herein we report on a one-step synthesis of highly pure cycloalkyl substituted monoimides without further purification (Figure 5.2). Cycloalkanes represent a special class of side-chains that possess a crossed orientation with the perylene plane at about 90˚, thus enforcing rotated stacking between the molecular planes so as to minimize the steric

hindrance caused by the cycloalkanes rings [12]. The rotated stacking enables strong fluorescence emission for the nanofibers thus fabricated from the molecules, though most of other PTCDIs demonstrate very weak emission due to the H-type interaction [3].

5.3 Results and discussions

Since the solubility of cycloalkyl monoimide in common organic solvents is very low, it is impossible to perform NMR characterization directly on the monoimide products obtained. To improve the solubility, the as-prepared monoimides were reacted with excessive dodecylamine to convert to the asymmetric disubstituted PTCDIs (Figure 5.3), which turned to be sufficiently soluble in chloroform, allowing for ^{1}H NMR characterization. As evidenced for all the three PTCDIs substituted with cyclopentyl, cyclohexyl, and cycloheptyl, the NMR spectra showed clean assignment to a single compound, which in turn indicated the high purity of the monoimide as prepared in Figure 5.2. The straight, highly selective production of monoimides thus observed is largely due to its insolubility in the mixed solvent of ethanol/water, which causes rapid precipitation of the product out of the reaction medium. Such precipitation-driven synthesis was previously employed in the preparation of macrocyclic conjugated molecules through cyclo-oligomerization [19, 20].

To further prove the concept of precipitation-driven synthesis, we changed the reaction medium from ethanol/water mixture to other alcohol based solvents, where the cycloalkyl PTCDIs remain insoluble [12]. These solvents include pure ethanol, methanol, and their mixtures with water containing varying levels of water up to 60%. As expected, the only product for the reaction following the same protocol described above (Figure 5.2) was the

corresponding monoimide. Increasing the water content above 60% makes it difficult to dissolve the alkyl amines, thus significantly slowing the reaction process.

The same reaction protocol was also tested for synthesizing other monoimides substituted with different side-chains such as dodecane (Figure 5.4). The reaction turned out not as selective as that performed with the cycloalkyl side-chains. In the best case (14:6 ethanol/water), the production yield of the dodecyl monoimide was only about 80%, with 20% parallel production of the diimide. This less selective reaction is likely due to the increased solubility of dodecyl monoimide in alcohols. Indeed, as previously observed in propanol/water mixture, the same reaction also produced diimide as impurity [21].

5.4 Conclusion

In summary, a series of perylene tetracarboxylic monoimides substituted with cycloalkyls were synthesized through a one-step reaction between cycloalkyl amines and the parent perylene dianhydride, which both are cheaply commercial available. The high selectivity thus obtained for the reaction is primarily due to the insolubility of the monoimides in the reaction medium, which in turn causes rapid precipitation of the products. This precipitation-driven synthesis may be extended to preparation of other perylene monoimides, for which selection of the appropriate reaction medium is the most critical for achieving the high purity of product. In general, an ideal reaction medium must possess minimal solubility (if not none) for the monoimides while still maintaining sufficient solubility for the reactant amines.

5.5 Experimental section

In one typical reaction, perylene-3,4,9,10-tetracarboxylic dianhydride (0.2 g, 0.51 mmol), cyclohexylamine (0.5 mL, 4 mmol), and ethanol/water (20 mL, volume ratio of 4:1) were mixed and heated at 70 ^{o}C for 6 h. The reaction mixture was cooled to room temperature and acidified by adding 30 mL concentrated HCl (12 M) and 20 mL water. After stirring overnight, the resulted solid was collected by vacuum filtration through a 0.45 μm membrane filter (Osmonics), followed by washing with methanol and water until the pH of washings turned to be neutral. The collected solid was dried in vacuum at 60 ^{o}C. The solid thus obtained was proven pure with no formation of the diimide, which has significant solubility in chloroform and can be spotted (if any) by alumina TLC (eluent:chloroform/methanol of 9:1).

The asymmetric PTCDIs substituted with dodecyl and three different cycloalkyl groups were synthesized following the standard condensation method previously developed (see [4] and [17]). In a typical reaction, 193 mg (0.41 mmol) of the cyclohexyl substituted monoimide, 113 mg (0.61 mmol) of dodecylamine and 2 g of imidazole were heated at 120 ^{o}C under argon for 4 h. The reaction mixture was cooled to room temperature and dispersed into 10 mL ethanol, followed by addition of 25 mL of 2 M HCl. After stirring overnight, the resulting solid was collected by vacuum filtration through a 0.45 μm membrane filter (Osmonics). The red solid was then washed thoroughly with methanol and water until the pH of washings turned to be neutral. The collected solid was dried in vacuum at 60 ^{o}C. TLC: R_f (silica gel/CH_3Cl:methanol 95:5) = 0.60. The purity and structure of the three asymmetric PTCDIs thus prepared (as shown in Figure 5.3) were confirmed by ^{1}H NMR as presented below:

***N*-cyclopentyl-N'-dodecyl-perylene-3,4,9,10-tetracarboxylic diimide.** ^{1}HNMR (500 MHz, $CDCl_3$): δ = 0.87 (t, 3 H, CH_3), 1.24–2.28 (m, 28 H, 14 CH_2), 4.11(t, 2 H, CH_2), 5.53 (t, 1 H, CH), 8.15 (m, 8 H, perylene).

***N*-cyclohexyl-N'-dodecyl-perylene-3,4,9,10-tetracarboxylic diimide.** ^{1}HNMR (500 MHz, $CDCl_3$): δ = 0.87 (t, 3 H, CH_3), 1.24–2.28 (m, 30 H, 15 CH_2), 4.16(t, 2 H, CH_2), 5.04 (t, 1 H, CH), 8.44 (m, 8 H, perylene).

***N*-cycloheptyl-N'-dodecyl-perylene-3,4,9,10-tetracarboxylic diimide.** ^{1}HNMR (500 MHz, $CDCl_3$): δ = 0.87 (t, 3 H, CH_3), 1.24–2.28 (m, 32 H, 16 CH_2), 4.17(t, 2 H, CH_2), 5.20 (t, 1 H, CH), 8.50 (m, 8 H, perylene).

5.6 References

[1] Hoeben, F. J. M.; Jonkheijm, P.; Meijer, E. W.; Schenning, A. P. H. J. *Chem. Rev.* **2005**, *105*, 1491–1546.

[2] Newman, C. R.; Frisbie, C. D.; da Silva Filho, D. A.; Bredas, J.-L.; Ewbank, P. C.; Mann, K. R. *Chem. Mater.* **2004**, *16*, 4436–4451.

[3] Wurthner, F. *Chem. Commun.* **2004**, 1564–1579.

[4] Zang, L.; Che, Y.; Moore, J. S. *Acc. Chem. Res.* **2008**, *41*, 1596–1608.

[5] Balakrishnan, K.; Datar, A.; Naddo, T.; Huang, J.; Oitker, R.; Yen, M.; Zhao, J.; Zang, L. *J. Am. Chem. Soc.* **2006**, *128*, 7390–7398.

[6] Balakrishnan, K.; Datar, A.; Oitker, R.; Chen, H.; Zuo, J.; Zang, L. *J. Am. Chem. Soc.* **2005**, *127*, 10496–10497.

[7] Che, Y.; Datar, A.; Balakrishnan, K.; Zang, L. *J. Am. Chem. Soc.* **2007**, *129*, 7234–7235.

[8] Che, Y.; Datar, A.; X., Y.; Naddo, T.; Zhao, J.; Zang, L. *J. Am. Chem. Soc.* **2007**, *129*, 6354–6355.

[9] Vura-Weis, J.; Ratner, M. A.; Wasielewski, M. R. *J. Am. Chem. Soc.* **2010**, *132*, 1738–1739.

[10] Carmen Ruiz Delgado, M.; Kim, E.-G.; da Silva Filho, D. A.; Bredas, J. L. *J. Am. Chem. Soc.* **2010**, *132*, 3375–3387.

[11] Datar, A.; Balakrishnan, K.; Yang, X. M.; Zuo, X.; Huang, J. L.; Yen, M.; Zhao, J.; Tiede, D. M.; Zang, L. *J. Phys. Chem.* **2006**, *110*, 12327–12332.

[12] Che, Y.; Yang, X.; Balakrishnan, K.; Zuo, J.; Zang, L. *Chem. Mater.* **2009**, *21*, 2930–2934.

[13] Che, Y.; Yang, X.; Loser, S.; Zang, L. *Nano Lett.* **2008**, 2219–2223.

[14] Che, Y.; Zang, L. *Chem. Commun.* **2009**, 5106–5108.

[15] Che, Y.; Yang, X.; Liu, G.; Yu, C.; Ji, H.; Zuo, J.; Zhao, J.; Zang, L. *J. Am. Chem. Soc.* **2010**, 5743–5750.

[16] Kazmaier, P. M.; Hoffmann, R. *J. Am. Chem. Soc.* **1994**, *116*, 9684–9691.

[17] Langhals, H. *Heterocycles* **1995**, *40*, 477–500.

[18] Zang, L.; Liu, R.; Holman, M. W.; Nguyen, K. T.; Adams, D. M. *J. Am. Chem. Soc.* **2002**, *124*, 10640–10641.

[19] Zhang, W.; Moore, J. S. *J .Am. Chem. Soc* **2004**, *126*, 12796.

[20] Zhang, W.; Brombosz, S. M.; Mendoza, J. L.; Moore, J. S. *J. Org. Chem.* **2005**, *70*, 10198–10201.

[21] Geerts, Y.; Quante, H.; Platz, H.; Mahrt, R.; Hopmeier, M.; Bohmc, A.; Mullen, K. *J. Mater. Chem.* **1998**, *8*, 2357–2369.

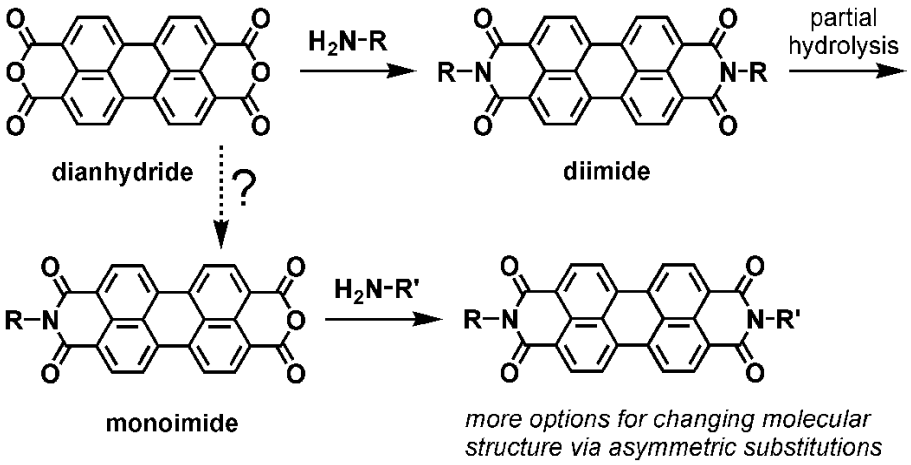

Figure 5.1 Synthetic pathways for PTCDIs.

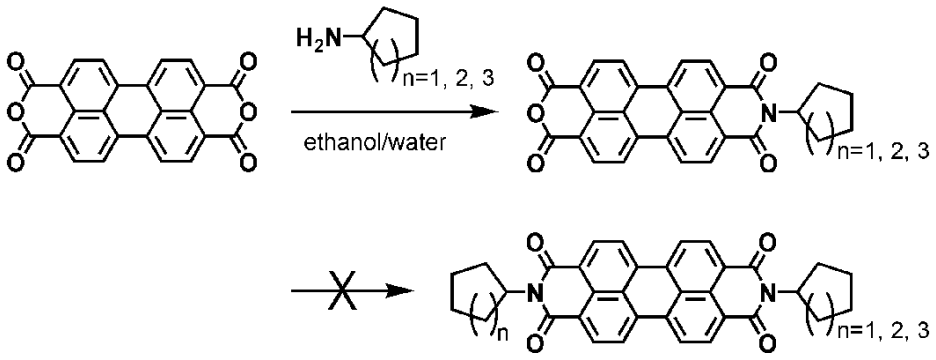

Figure 5.2 One-step condensation leading to selective production of monoimides.

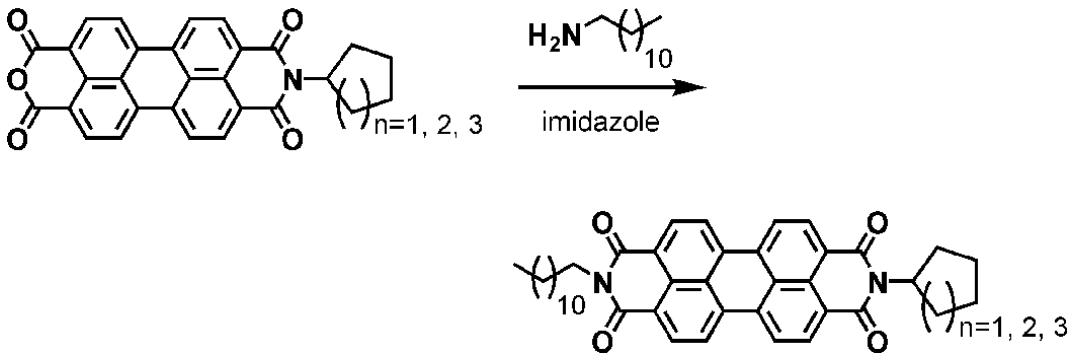

Figure 5.3 Substituting the monoimides with long alkyl side-chains to improve the solubility for NMR characterization.

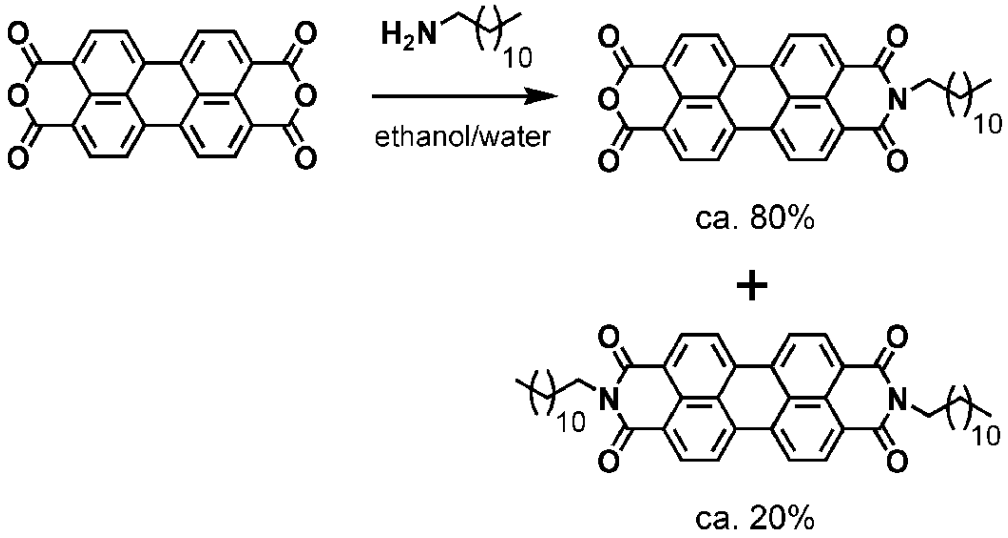

Figure 5.4 One-step condensation with linear alkyl amines shows decreased selectivity for the production of monoimides.

CHAPTER 6

CONCLUDING REMARKS

6.1 Conclusion

The primary goal of this thesis project was to investigate the structure-property relationship in organic nanofibril heterojunction materials through 1) designing and synthesizing functional building block molecules, 2) self-assembling the molecules into well-defined nanofibers and fabricating nanofibril heterojunction through interfacial engineering (e.g., solvent or vapor processing), and 3) constructing optical and electrical devices employing the nanofibril heterojunction materials and testing the photoconductivity and sensor properties.

In Chapter 1, a brief introduction of synthesis and application of one-dimensional heterojunction nanofibril materials are reviewed, especially on the relevant applications in photodetectors and vapor sensors. Also discussed in this chapter are the disadvantages of current nanofibril fabrication methods and the possible solutions for the fabrication problems.

In Chapter 2, highly photoconductive organic nanofibril heterojunctions have been fabricated through simple interfacial engineering of the hydrophobic interaction between alkyl side-chains of D and A parts. Such nanofibril heterojunctions possess two prominent features that are critical for efficient photocurrent generation: one is that the nanofibers

both create a wide D/A interface for increased charge separation and act as a long-range transport pathway for photogenerated charge carriers towards the electrodes; the other is that the alkyl groups modified at the A molecules not only enable effective surface adsorption of D molecules on the nanofibers for effective electron-transfer communication, but also spatially separate the photogenerated charge carriers to prevent their recombination. The reported approach represents a simple, adaptable method allowing for development and optimization of photoconductive organic nanomaterials.

In Chapter 3, we further synthesized a series of electron donor molecules (**D1**–**D4**) that share the same π-conjugation core, but that were modified with different side groups. PTCDI fibers coated with such donor molecules showed a dramatically different photocurrent response. It was found that the nanofibers coated with homogeneously and molecularly distributed donor molecules (such as **D4)** exhibit the highest photocurrent, whereas those coated with segregated donor aggregates (such as **D1**–**D3)** show much lower photocurrent under the same illumination conditions. The aggregation of donor molecules on the surface of the PTCDI fibers may lead to the buildup of a local electrical field, which hinders the charge separation of the photogenerated electron-hole pairs. The different morphologies of molecular aggregates were mostly the result of side group modification of the donor molecules. Such structural effect was more clearly manifested by investigating the structure and morphology change of the drop-casting films upon solvent vapor annealing. The findings presented provide new insight into the molecular structural effect on photoconductivity of organic semiconductor materials, particularly those based on donor-acceptor composites or interfaces, and open alternative ways to improve the photoconductivity by structural design and modification.

In Chapter 4, we developed an alternative nanofibril heterojunction structure through vapor deposition process. High dark electrical conductivity was obtained for a p-type organic nanofibril material simply through a one-step surface coating (doping) of electron withdrawing (accepting) molecules. The nanofibril composite thus fabricated has been proven robust under ambient conditions. The high conductivity, combined with the intrinsic large surface area of nanofibers, enables the development of chemiresistor sensors for trace vapor detection of amines, with detection limits down to sub-ppb range. The reported work represents a simple approach to the fabrication of highly conductive nanofibril materials, which may find broad application in sensors and other electronic systems.

In Chapter 5, a large-scale one-step synthetic method has been developed for perylene monoanhydride building block material. High yield reaction protocol laws were achieved. Traditional synthesis of these molecules requires two-step reactions, which are time consuming and with low yield. A series of perylene tetracarboxylic monoimides substituted with cycloalkyls were synthesized through a one-step reaction between cycloalkyl amines and the parent perylene dianhydride, which both are commercially available at low cost. The high selectivity thus obtained for the reaction is primarily due to the insolubility of the monoimides in the appropriately selected reaction medium, which in turn causes rapid precipitation of the products. This precipitation-driven synthesis may be extended to preparation of other perylene monoimides, for which selection of the appropriate reaction medium is the most critical for achieving the high purity of product. In general, an ideal reaction medium must possess minimal solubility (if not none) for the monoimides while still maintaining sufficient solubility for the reactant amines. This approach opens up a new

way for large scale production of the monoimides, which are the precursor for making a variety of perylene based building block molecules.

6.2 Suggestions for future plan

For future research, further exploration of the structure-property relationship will be performed by extending onto other surface-coating materials. For example, poly (3-hexylthiophene) (P3HT) is widely used as a p-type material in organic solar cells due to its broad absorption and efficient charge transport property. PTCDI molecules can act as the n-type material in the solar cell, which have strong electron affinity and extensive absorption in the visible light region. A solar cell device that combines P3HT and PTCDI as their building block materials is expected to have promising photovoltaic performance. Recently, we have fabricated the shish-kebab-like p-n junction nanostructures of P3HT and PTCDI by using interfacial engineering process. The P3HT nanofiber branches off the PTCDI trunk normal to its long axis. Remarkably, these shish-kebab-like structures demonstrated unprecedentedly high photovoltages. A record-breaking 2.3 V open circuit voltage was obtained, which is much larger than the theoretical threshold value (1.2 V). The exceptional high open circuit voltage may be attributed to the presence of large numbers of charge carriers accumulated across the interface between P3HT and PTCDI [1]. More work is underway to further explore the mechanism of high open circuit voltage and improve material structure and morphology to increase the photoconversion efficiency.

The vapor deposition method described in Chapter 4 can also be improved and adapted to fabricate n-type nanofibril heterojunctions. One proposal is to change the coating molecule from FTS to amine-terminated silane molecules, which have a strong tendency

to form a uniform monolayer on the surface of PTCDI nanofiber through lateral self-assembly. Such a monolayer-coated nanofibril heterojunction material has two possible advantages: 1) the amine part has a strong electron-donating capability, which can transfer electrons to the PTCDI part to increase the charge carrier density, 2) the terminal amine group can also form noncovalent bonds with analyte molecules, which have the potential to increase the sensor sensitivity and selectivity. Recently, it has been found that amine-functionalized nanowire has extraordinary sensitivity toward vapor analytes [2, 3]. For example, TNT molecules can strongly bind to the surface of the nanowires through an acid-base interaction with the amine group. Due to this enhanced interfacial binding, the sensor device can detect TNT with an unprecedented low concentration (subfemtomolar, $< 10^{-15}$ M). However, the matrix materials used in these studies are inorganic nanowire materials, for which the detection selectivity is limited due to the lack of specific interfacial interaction between analyte and sensor material. The amine-functionalized PTCDI nanofiber proposed herein will likely fill this technical gap by providing high selectivity while still maintaining the high sensitivity.

6.3 References

[1] Li, L.; Jacobs, D. L.; Bunes, B. R.; Huang, H.; Yang, X.; Zang, L. *Polym. Chem.* **2014**, *5*, 309–313.

[2] Engel, Y.; Elnathan, R.; Pevzner, A.; Davidi, G.; Flaxer, E.; Patolsky, F. *Angew. Chem. Int. Ed.* **2010**, *49*, 6830–6835.

[3] Hoffmann, M. W. G.; Prades, J. D.; Mayrhofer, L.; Hernandez-Ramirez, F.; Järvi, T. T.; Moseler, M.; Waag, A.; Shen, H. *Adv. Funct. Mater.* **2014**, *24*, 595–602.